HIGH FRAME RATE ULTRASOUND VELOCIMETRY

OF FAST BLOOD FLOW DYNAMICS

Jason VOORNEVELD

ISBN
978-94-632-3807-6

Lay-out
Jason Voorneveld

Cover
Keda Gomes, Jason Voorneveld

Print
Gildeprint, Enschede

© J.Voorneveld, 2019, excluding:
Chapter 2 © IEEE, 2016
Chapter 3 © IEEE, 2018
Chapter 4 © RSNA, 2018
Chapter 5 © IEEE, 2017
Chapter 6 © American Heart Association, Inc, 2019
Chapter 7 © SPIE, 2017
Chapter 8 © Elsevier Ltd, 2019

All rights are reserved. No part of this book may be reproduced, distributed, stored in a retrieval system, or transmitted in any form or by any means, without prior written permission of the author.

An electronic version of this dissertation is available at
`http://hdl.handle.net/1765/115832`.

HIGH FRAME RATE ULTRASOUND VELOCIMETRY

OF FAST BLOOD FLOW DYNAMICS

SUPERSNELLE ECHOGRAFIE
VOOR DYNAMISCHE BLOEDSTROMINGSPATRONEN

Thesis

to obtain the degree of Doctor from the
Erasmus University Rotterdam
by command of the
rector magnificus

Prof. dr. R. C. M. E. Engels

and in accordance with the decision of the Doctorate Board.

The public defence shall be held on
Tuesday the 17th of September 2019 at 11:30 hrs
by

Jason Dirk Voorneveld

born in Johannesburg, South Africa

Erasmus University Rotterdam

Doctoral Committee

Promotors:	Prof. dr. ir. N. de Jong Prof. dr. ir. A. F. W. van der Steen
Other members:	Prof. dr. L. Løvstakken Prof. dr. M-X. Tang Dr. A. E. van den Bosch
Co-promotor:	Dr. ir. J. G. Bosch

This work was supported by ZonMw within the Innovative Medical Devices Initiative Program under Project Heart Failure and 4-D Flow with number 104003001

The research described in this thesis has been carried out at the Department of Biomedical Engineering, Thorax Center, Erasmus MC Medical Center Rotterdam.

Financial support for the publication of this thesis was graciously provided by:
Erasmus Medical Center,
Bracco Imaging,
Oldelft Ultrasound.

Financial support by the Dutch Heart Foundation for the publication of this thesis is gratefully acknowledged.

CONTENTS

1

INTRODUCTION

1.1. CARDIOVASCULAR SYSTEM

The cardiovascular system is responsible for delivering oxygen, nutrients and hormones to the rest of the body and returning carbon dioxide and waste products for removal. Diseases of the cardiovascular system are the leading cause of death globally [1]. At the centre of the cardiovascular system is the heart, which pumps oxygenated blood out of the left ventricle into the aorta before breaking off into networks of gradually smaller vessels, eventually ending in capillary beds which allow for nutrient and oxygen exchange into tissues and organs. The capillaries then drain into the venous system for waste product removal, returning to the right side of the heart. The right heart pumps deoxygenated blood into the lungs, removing carbon dioxide and replenishing oxygen. Blood from the lungs then drains into the left atrium which, in turn, supplies the left ventricle, ready to start the cycle all over again.

1.1.1. BLOOD FLOW

Blood flow in the heart and greater vessels is time varying, three dimensional and complex. For instance, in the left ventricle's (LV) filling phase (diastole), the muscles of the LV wall relax, causing blood to come rushing into the LV cavity from the atrium. As the blood passes the mitral valve, flow interacts with the tips of the valves and collides with the slow moving blood in the LV chamber, forming a vortex ring [2]. This vortex ring is believed to help the jet penetrate deeper towards the apex of the ventricle, preventing blood from stagnating in the ventricle and forming thrombi [3]. Additionally, the vortex ring slowly expands outwards as it travels which forms swirling patterns that smoothly redirect blood towards the aortic outflow tract just in time for ejection during systole (See Figure 1.1) [4].

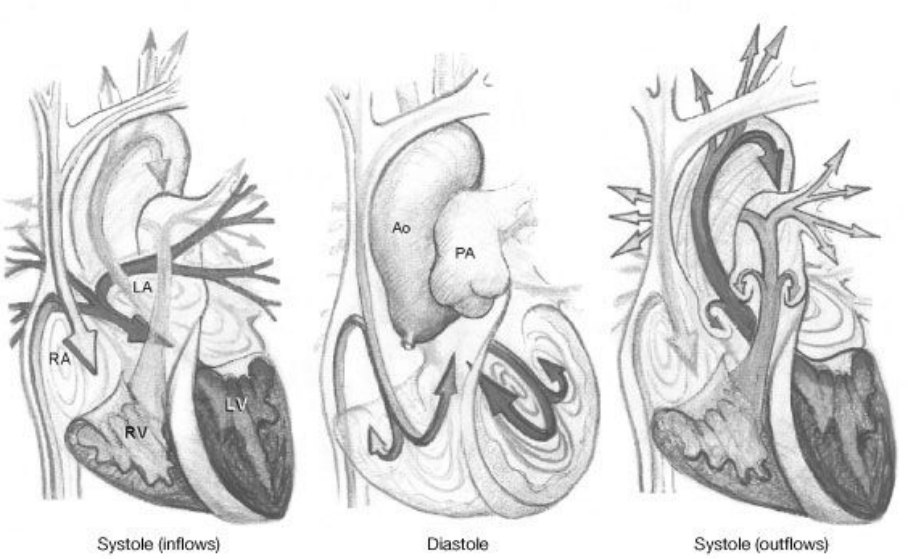

Figure 1.1: Flow patterns during the different cardiac phases. Blood initially drains into the atria (left), forming distinct vortical patterns. During diastole, blood flows from the atria into the ventricles, forming asymmetrical vortices (middle). During ejection, blood flow is already aligned for ejection, due to the swirling motion from previous phases. RA = right atrium, LA = left atrium, RV = Right Ventricle, LV = Left Ventricle, PA = Pulmonary Artery, Ao = Aorta. Image reprinted, with permission, from [4] © *2000, Springer Nature*

Blood flow dynamics in the LV are known to be influenced by LV loading conditions, such as LV relaxation (expanding of the LV to fill with blood) and left atrial pressure (pushing force from the atrium into the LV) [5]. Left ventricular blood flow dynamics are also believed to be involved in the development of LV dysfunction, by complex interactions with cells of the heart wall in a process known as mechanotransduction [6]–[8]. Changes in LV vortex formation, caused in early stages of LV dysfunction, are thought to result in local changes in wall shear stress which lead to unfavourable LV remodelling and further disease progression [9].

Similarly, in arterial flow, regions of bifurcation are known to have complex vortical flow patterns. E.g. the common carotids splitting into the internal and external carotids and the abdominal aorta splitting into the iliac arteries. Atherosclerotic lesions are known to preferentially form in these regions of complex flow patterns, where local wall shear stress is low and oscillatory [10]. Additionally, abdominal aortic aneurysms (where the vessel walls weaken, thin and balloon outwards) are also known sites of vortical flow patterns; where it is thought that wall shear stress influences arterial remodelling.

The study of blood flow dynamics and its association with cardiovascular disease *in vivo* requires methods to (preferably non-invasively) measure blood flow patterns. Note that velocity estimates are required over both space and time, where blood flow patterns

vary both spatially and temporally. The next section will discuss current methods for non-invasive blood flow measurement.

Heart Failure

Heart failure is when the heart cannot meet the rest of the body's demand for oxygenated blood. People with heart failure can find everyday activities such as walking or climbing stairs extremely difficult. Heart failure presents society with a significant health burden, affecting over 26 million people world-wide [11]. Additionally, it is associated with high rates of co-morbidities and mortality. Its prevalence is predicted to increase 46% from 2012 (~ 6 million) to 2030 [11], [12] (in the United States). Early diagnosis of heart failure may provide more opportunities for effective treatment and prevention of disease progression and co-morbidities.

1.2. CLINICAL BLOOD FLOW MEASUREMENT

1.2.1. DOPPLER ULTRASOUND

As the name implies, Doppler ultrasound is a method of quantifying flow based on the Doppler shift of the frequency spectrum: $f_d = f_0 \times (2|\vec{v}|\cos\theta/c)$, where f_d and f_0 are the Doppler frequency and transmit frequency, c is the speed of sound and $|\vec{v}|\cos\theta$ is the velocity component along the ultrasound beam [13]. Doppler forms the backbone of clinical blood flow imaging, with different forms of the Doppler technique being used for different applications.

Continuous wave (CW) Doppler can estimate the velocities along an axial line extending from the probe, but it is not possible to distinguish where the velocity signals originate along that line. Pulsed-wave (PW) Doppler uses focussed pulses to measure the velocities in a predefined region ('range-gate') of the image (Figure 1.2.a). However, due to the use of pulses over continuous waves, care must be taken to avoid aliasing of high velocities if the pulse-repetition-frequency (PRF) is not high enough. Note that PW Doppler uses a phase shift between pulses to approximate the Doppler frequency shift, due to the broad-band nature of pulsed ultrasound [14]. Colour Doppler can measure the mean velocities present over a large 2D region of interest (Figure 1.2.b) but at the cost of low frame rates (<20 fps), lower resolution/accuracy and it is also susceptible to aliasing (Figure 1.2.c). Note that even though 2D flow images can be obtained with colour Doppler, the velocities depicted in these images are only the velocity components aimed towards (typically encoded with a red colour) and away from the probe (blue colour). The velocity components transverse to the ultrasound beam cannot be measured using standard Doppler techniques.

1.2.2. MAGNETIC RESONANCE IMAGING

Before continuing with emerging echocardiographic blood flow analysis techniques, it is worth giving a brief review of blood flow quantification using phase-contrast MRI (PC-MRI). PC-MRI can measure the blood flow velocity in all directions, either in a 2D plane or a 3D volume (often called 4D-flow MRI – see Figure 1.3). PC-MRI requires several

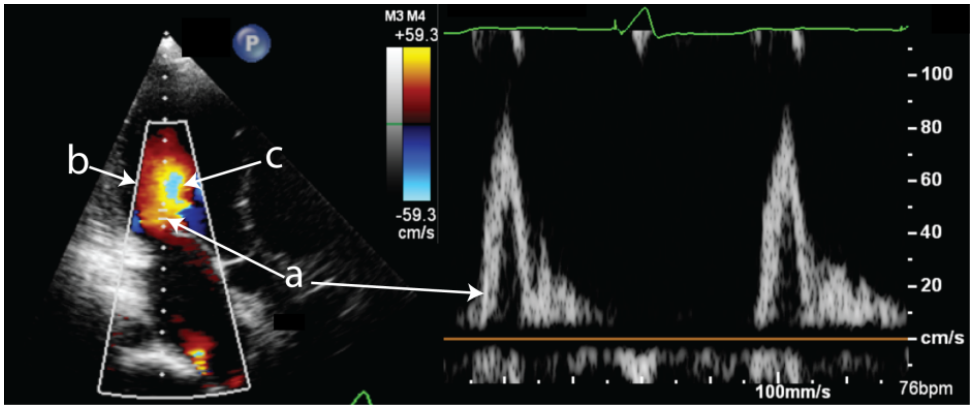

Figure 1.2: a) PW Doppler, showing range gate (left) and velocity spectrum over time (right). b) Colour Doppler sector, with flow towards and away from transducer color-coded in red and blue, respectively. c) High velocity aliasing, where the colormap quickly switches from yellow (fast flow towards the probe) to light-blue (fast flow away from the probe)

heartbeats to acquire accurate velocity information and uses electro-cardiogram (ECG) gating to achieve this. Typically, 20-30 phases are acquired per cardiac cycle. The ability to measure all three velocity components over the whole heart allows for quantification of interesting blood flow dynamics, such as vorticity, blood residence time, kinetic energy, energy dissipation and local pressure gradients. The key draw-back of PC-MRI is the long acquisition times, where hundreds of heart beats are required to generate the flow sequences. This causes some complications, such as the need for breath-holds to prevent motion related artefacts; and the fact that the flow sequences are not real time representations of the flow per cycle but the phase-averaged flow over the whole acquisition length. Additionally, MRI equipment is expensive, requiring specialized infrastructure and is not useable as a bed-side imaging technique. The ability to measure 3D blood flow using echocardiography, like that of PC-MRI would be beneficial.

1.3. ULTRASOUND VECTOR FLOW IMAGING

Many ultrasound techniques have been developed to address the need for measuring both the axial and lateral velocity components in cardiovascular imaging. A brief introduction of these techniques will be provided in this section, but a comprehensive review is available in [16], [17].

Vector Doppler (VD) uses two or more angled transmit beams to obtain independent 'views' of the velocity field, which can then be used to deduce the separate axial and lateral components [18]–[20]. The accuracy of VD is affected by the relative beam angle(s) between views, where larger angles provide better accuracy. Thus, VD is more often used in superficial vascular applications, where large aperture linear arrays are used to allow for larger angles. VD has been implemented commercially as V-Flow on Mindray's Resona7 ultrasound imaging system [21].

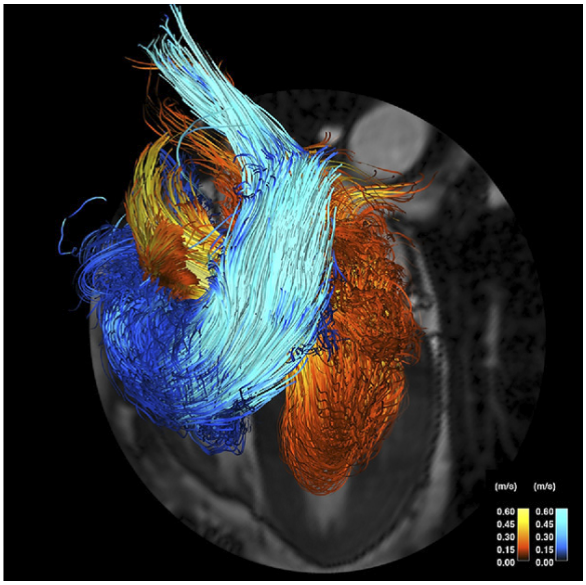

Figure 1.3: 4D-flow MRI based path-line visualization of blood flow throughout the whole heart, with oxygenated blood flow in a black-to-red colormap and deoxygenated blood in a black-to-blue colormap. Image reprinted, with permission, from [15] © *2012 American College of Cardiology Foundation. Published by Elsevier Inc. All rights reserved.*

A similar technique, called *Transverse Oscillations* (TO), generates a laterally modulating field by applying a two peak apodization function on the received signals. Thus phase shift can be deduced both axially (similar to standard colour Doppler) and laterally [22]. The wavelength of the lateral modulation can be calculated as: $\lambda_{lat} = 2\lambda_{ax} d/P_d$, where λ_{ax}, d and P_d are the axial wavelength, depth from the probe and distance between the peaks, respectively [18]. It can be seen from the lateral wavelength equation that the depth of interest (d) and the available aperture (maximum P_d possible) are directly related to the lateral wavelength, and in turn the accuracy of the lateral estimate. However, despite this limitation, work has been done on extending TO to greater depths using curvilinear arrays [23] and phased arrays [24]. TO has been demonstrated for LV flow analysis but suffered from low frame rates (11 fps) when imaging the whole LV and requires validation *in vivo* [25].TO has been implemented commercially as 'vector flow imaging' by BK Medical [26].

Vector Flow Mapping (VFM) uses standard colour Doppler and LV wall motion segmentations, in combination with a fluid dynamics model of blood flow to calculate the lateral velocity components in the LV [27]–[29]. VFM has the advantage that data can be acquired using standard clinical ultrasound scanners and post-processed using VFM offline. Careful attention must be paid when choosing wall filter and velocity cut-off settings of the colour Doppler data to prevent erroneous VFM results. Out-of-plane motion, frame rate (<15 Hz, due to the large sector size needed to include the whole LV) and ve-

locity aliasing are some of the key limitations of VFM. VFM has been implemented commercially in Hitachi ultrasound scanners [30]. Doppler Vortography is a similar method to VFM, in that it only requires colour Doppler data, but instead calculates an index of blood vorticity directly from the anti-symmetry of the Doppler data around vortices, bypassing the need for time-resolved vector fields [31], [32].

Blood Speckle Tracking (ST) estimates 2D or 3D blood velocities by tracking blood speckle patterns over time. Ultrasound speckle is an interference patterns caused by the summation of many sub-resolution scatterers, in this case red blood cells [33]. The displacement of the speckle pattern is assumed to reflect the underlying motion of the blood cells. ST works in three main steps: 1) sub-divide the image into smaller blocks (kernels); 2) calculate the similarity between each block (template) and the matching block in the next frame (target); 3) find the optimum in the similarity measure to estimate the displacement (usually a sub-pixel estimator is used to achieve sub-pixel precision) [16]. ST typically requires imaging at a high frame rate (HFR) in order to track high velocity flows, such as the diastolic inflow jet which can exceed 1 m/s in magnitude. ST has been used to image cardiac blood flow patterns in neonates [34], paediatric patients [35] and adults [36]. ST has been implemented commercially as 'blood speckle imaging' in GE's Vivid E95 system.

Due to the use of HFR imaging, ST suffers from poor signal-to-noise ratio (SNR) and increased sensitivity to clutter (high intensity signal from surrounding tissue overlaying moving blood signal). The low SNR is a result of the low echogenicity of blood cells, especially when compared to tissue signal. This can be alleviated by using ultrasound contrast agent (UCA) microbubbles, which greatly improve the back-scattered signal over blood cells. Additionally, the use of microbubbles allows control over scatterer concentration (sparsity). The tracking of microbubbles to measure blood flow is called Echo-Particle Image Velocimetry (echoPIV).

Ultrasound Contrast Agent (UCA)

Microbubbles are the most common form of UCA, consisting of a gas encapsulated in a lipid, albumin or polymeric shell, with a diameter of between 1 μm and 10 μm. Microbubbles are beneficial for ultrasound blood pool imaging due to the enormous increase in scattering strength compared with red blood cells, where a microbubble can have a scattering cross section of up to a billion times that of a similarly sized solid particle [37], [38]. The increased signal intensity is due to 1) the large acoustic impedance mismatch between the encapsulated gas core of the microbubble and the surrounding liquid; and 2) the compressibility of the gas, which causes highly non-linear radial oscillations. These non-linear oscillations can be exploited using specialized imaging sequences to distinguish bubble signal from tissue signal. Examples of such imaging sequences are power modulation [39] and pulse inversion [40], [41]. The use of UCA to improve ultrasound imaging is called contrast enhanced ultrasound (CEUS).

1.3.1. ECHO-PARTICLE IMAGE VELOCIMETRY (ECHOPIV)

EchoPIV (also known as ultrasound image velocimetry – UIV) tracks the displacement of microbubbles over time, similar to how ST tracks red-blood cells; where it is assumed that the microbubbles faithfully follow the blood flow. EchoPIV was derived from optical PIV, which is the industry gold standard for velocimetry in fluid dynamics research - where optical access is available. EchoPIV was first implemented using a clinical ultrasound scanner and UCA microbubbles by Kim et al. (2004) [42].

Since then a few studies have assessed the accuracy of echoPIV for studying LV flow patterns, using conventional line-scanning acquisitions from clinical ultrasound machines. It was found that while echoPIV could accurately measure the velocity and direction of relatively low velocity flows (< 0.4 m/s); large underestimations occurred for the high velocity flows, which are associated with ventricular filling and ejection [43]–[45]. The underestimation of high velocity flows was attributed to insufficient frame rate to accurately track the fast moving bubbles between frames. However, the same studies also found that while the magnitude of the high velocities were severely underestimated, the direction of the vectors was less affected by the insufficient frame rate, concluding that echoPIV was a promising approach for analysis of intra-ventricular flow patterns.

Conventional echoPIV has been used in a number of small human studies, exploring the relationship of various flow and vortex related metrics with clinical presentation and outcome. These studies include: characterizing the flow parameters of healthy LVs in volunteers [46]; assessing indicators of LV pump efficiency [47] and thrombus formation [48] in patients with myocardial infarction; comparison of LV flow properties between patients with heart failure and normal controls [49], [50]; relating LV flow properties in patients with heart failure undergoing cardiac resynchronization therapy to clinical outcome [6], [51], [52]; assessing the effect of various prosthetic mitral valves on LV flow properties [53]; studying the left and right ventricular flow properties in patients with repaired Tetralogy of Fallot [54]; and characterisation of left atrial vortex properties in patients with atrial fibrillation [55]. Multiple reviews of existing echoPIV studies have been published [9], [15], [56], [57].

The most commonly reported metrics from the previously mentioned studies are: vortex position (where the center of the main vortex sits inside the chamber); vortex morphology (width, height, sphericity); vortex strength; vortex direction (clockwise or anticlockwise in a particular view); kinetic energy (system energy stored in moving blood); kinetic energy dissipation (kinetic energy lost to heat); and local pressure gradients.

However, how the sensitivity of these flow parameters is affected by the velocity underestimation during filling and ejection has yet to be evaluated. Important information relating to clinical outcome may be lost by the underestimation. Additionally, these studies have all been performed in 2D, due to the even lower frame rates possible with 3D ultrasound imaging on current clinical scanners, potentially missing important out-of-plane flow information.

High Frame Rate (HFR) Ultrasound

Conventionally, ultrasound images are constructed by transmitting and scanning many focussed beams (line scanning) into the region-of-interest, waiting after each beam to record the returned signals. Due to the constant speed of sound (1540 m/s in human tissues), the frame rate achievable is severely limited, usually less than 100 frames per second (fps). Instead, by transmitting broad beams such as plane waves or diverging waves, the entire region-of-interest can be insonified all at once, where the receive signals are then stored in memory for software beamforming. This allows for frame rates of approximately 100 times those possible using conventional line scanning methods. The trade-off is image quality, with lower contrast and resolution than line scanning, due to lack of focussing in transmit. Contrast and resolution can be improved, at the cost of frame rate, by using angled transmissions, to synthetically focus in transmit (Figure 1.4). See [58], [59] for more information on HFR (ultrafast) ultrasound imaging.

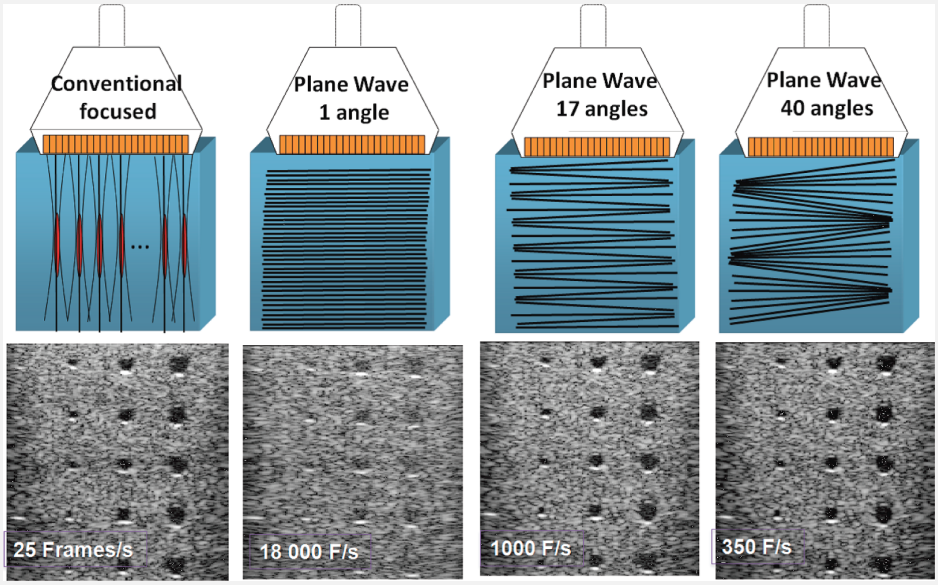

Figure 1.4: Conventional focussed (line scanning) ultrasound imaging (far left) and HFR ultrasound imaging with only plane waves (middle left). Image quality is reduced for HFR but can be recovered by using angled plane waves and coherent compounding (middle right). Using more angles further improves image quality, in some cases matching or even surpassing conventional imaging (far right). Image reprinted, with permission, from [58] © *2014, IEEE*

CHALLENGES

Two key limitations exist for current echoPIV research: 1) Early validation studies revealed that high velocity flows were severely underestimated [43]–[45]; and 2) flow data were acquired (and interpreted) in 2D, where LV flow is inherently complex, time-varying and 3D.

High velocity flows are underestimated due to the large bubble displacements between successive frames. It is believed that by using HFR ultrasound in conjunction with echoPIV, we will be able to track the full range of velocities expected in the LV. The issue of frame rate is even further exacerbated in 3D imaging, where focussed lines need to be formed along both azimuth and elevation. The use of HFR imaging in 3D is not as straightforward as in 2D, due to the complexities of electronically connecting the thousands of elements and large data-rates required for matrix transducers.

1.4. THIS THESIS

1.4.1. AIM

The aim of this thesis is to explore HFR ultrasound sequences for use with echoPIV in 2D and 3D, with the aim of measuring the high velocity blood flow patterns present in LV and greater vessels.

1.4.2. OUTLINE

This thesis gradually increases the complexity of the flow being studied and the ultrasound system being used. In **Chapter 2** we begin in 2D, with a simple laminar pipe-flow phantom to assess the accuracy of HFR echoPIV using angled plane-waves with a linear array. Here we assess whether UCA is really required, comparing ST with blood-mimicking fluid to echoPIV with UCA at different depths. We find that UCA is beneficial at greater depths.

In **Chapters 3 & 4** we investigate HFR echoPIV for tracking abdominal aortic blood flow in healthy volunteers. First, in **Chapter 3**, we perform an *in vivo* parametric study of critical echoPIV parameters; then in **Chapter 4**, we assess the accuracy of echoPIV (using the optimal parameters found previously) by comparing with PC-MRI.

In **Chapter 5**, we go back to the laboratory, developing and using a dynamic LV phantom as a test platform for assessing the accuracy of HFR echoPIV against optical PIV. After finding that HFR echoPIV can indeed measure the high velocity diastolic blood flow patterns we assess whether this is possible in a patient (**Chapter 6**).

Chapter 7 moves on to 3D ultrasound; where we assess the accuracy of 3D HFR echoPIV using a miniaturized paediatric transoesophageal (TEE) transducer in a simulated pipe-flow phantom with a Womersley flow profile. We find that lateral resolution using such a small aperture probe causes severe underestimation in the jet velocity magnitude. Wanting to experiment with a prototype adult matrix TEE transducer (with a larger aperture) capable of HFR imaging, we develop a new LV phantom; this time capable of time-resolved volumetric optical PIV imaging (tomographic PIV). **Chapter 8** describes the new LV phantom and the tomographic PIV setup and also compares the flow patterns observed when using different prosthetic valve types. **Chapter 9** demonstrates high volume rate echoPIV using the prototype matrix TEE transducer and assesses its accuracy against time-resolved tomographic PIV.

Finally, in **Chapter 10**, HFR echoPIV is discussed with future perspectives.

2

NATIVE BLOOD SPECKLE VS ULTRASOUND CONTRAST AGENT FOR PARTICLE IMAGE VELOCIMETRY WITH ULTRAFAST ULTRASOUND – IN VITRO EXPERIMENTS

Based on:
Voorneveld J, Kruizinga P, Vos HJ, Gijsen FJH, Jebbink EG, van der Steen AFW, de Jong N, Bosch JG. Native blood speckle vs ultrasound contrast agent for particle image velocimetry with ultrafast ultrasound - *in vitro* experiments, *Proc. IEEE International Ultrasonics Symposium (IUS)*, Sep. 2016. [60].

ABSTRACT

Ultrafast contrast enhanced ultrasound, combined with echo particle image velocimetry (echoPIV), can provide accurate, multidimensional hemodynamic flow field measurement. However, the use of ultrasound contrast agent (UCA) still prevents this method from becoming a truly versatile and non-invasive diagnostic tool. In this study, we investigate the use of native blood instead of UCA backscatter for echoPIV measurements and compare their accuracy in vitro. Additionally, the effect of measurement depth is experimentally assessed.

Blood mimicking fluid (BMF) was pumped through a 10 mm diameter tube producing parabolic flow profiles, adding UCA in the case of contrast imaging. Plane wave imaging at 5000 frames- per-second was performed with a Verasonics Vantage system and a linear array. The tube was imaged at three different depths: 25, 50 and 100 mm. Singular value decomposition (SVD) was assessed for clutter suppression against mean background subtraction. PIVlab was used as a PIV implementation.

With SVD, BMF provided almost equal echoPIV accuracy as UCA, except at 100 mm depth where UCA provided better accuracy. Use of clutter suppression greatly improved echoPIV results, but minimal differences in echoPIV accuracy were noted between mean and SVD filtered groups (BMF or UCA). Accuracy decreased with increasing depth, likely due to reduced elevation resolution, resulting in out-of-plane smoothing of velocity gradients.

2.1. INTRODUCTION

Visualization and quantification of blood velocity perpendicular to the ultrasound (US) beam direction remains a challenge in clinical imaging. This is especially true when imaging deep structures such as in the heart or abdominal aorta. In this case, vector imaging techniques such as *Vector Doppler* imaging suffer reduced accuracy due to limited probe aperture. A different approach for estimating velocity is by echo-particle imaging velocimetry (echoPIV), which instead operates on successive, beamformed frames, in a patch-by-patch basis, to determine velocity fields. While echoPIV was first demonstrated by Kim et al. (2004) [42], its success has been limited due to the relatively low frame-rates attainable in conventional ultrasound scanners (<100 fps). Low frame rate results in decorrelation of high velocity flows due to the relatively large particle displacement between frames. The recent advances in ultrafast ultrasound imaging offer a solution to this limitation of echoPIV [61]. However, the use of ultrasound contrast agent (UCA) still prevents echoPIV from becoming a truly versatile and non-invasive diagnostic tool. In this study, we compare the use of UCA and speckle from blood mimicking fluid (BMF, as a proxy for native blood speckle) as signal sources for echoPIV, after using singular value decomposition (SVD, [62]) as a clutter filter. Additionally, we perform the comparison at different depths, in an effort to investigate the relationship between echoPIV accuracy and depth.

2.2. METHODS

2.2.1. *In Vitro* PHANTOM

A custom designed *in vitro* flow phantom was used to pump blood mimicking fluid (BMF) through a 10mm diameter tube. The tube was immersed in water to allow for ultrasonic imaging at 3 different depths from the transducer lens (25, 50 and 10 mm). Calibrated flow rates, corresponding to parabolic velocity profiles, were measured with an inline ultrasonic flow meter (UF Ultrasonics Flow Meter, Cynergy3 Components, UK, 3% accuracy). Three physiologically relevant peak velocities (0.25, 0.5 and 0.75 m/s) were studied.

BMF was prepared according the recipe of Ramnarine et al. with 5 μm Orgasol particles, providing equivalent backscatter to human blood [63]. A diluted, commercial UCA (SonoVue, 50μl/l concentration) was added to the BMF in the case of contrast imaging.

2.2.2. ULTRAFAST ULTRASOUND ACQUISITION AND BEAMFORMING

Raw channel data were acquired with a Verasonics Vantage 256 system (Verasonics Inc., USA) using an ATL L7-4 transducer (5MHz, 25mm elevation focus, 298μm pitch, 128 elements). A plane wave acquisition protocol captured 300 frames at the pulse repetition frequency (PRF) of 5000 Hz. Three different clutter suppression techniques were compared by applying each filter on the pre-beamformed channel data: a) no filtering, b) mean subtraction (along slow time) and c) hard threshold SVD rank reduction (keeping ranks 5 to 270).

Beamforming was performed offline, using a Fast Fourier Transform (FFT) method [64]. Beamformed RF data was sinc-interpolated in the axial direction to obtain equal pixel spacing in axial and lateral direction. Finally, the envelope was detected and log compressed forming B-mode image sets.

2.2.3. ECHOPIV

PIVlab (V1.41,[65]) was used as a Particle Imaging Velocimetry implementation in Matlab (R2015a, The MathWorks Inc., Natick, MA). PIVlab utilizes an iterative approach to echoPIV, deforming the target kernel after each iteration according to the previous iteration's displacement estimates, theoretically converging towards true autocorrelation. In this study three iterations, with square kernel sizes of 2.3^2 mm^2, 2.3^2 mm^2 and 1.15^2 mm^2 for each successive iteration, were used, using bicubic interpolation for image deformation of the target image after each iteration. Post processing was limited to discarding the velocity estimates on the borders of the region of interest, no outlier elimination or smoothing was applied. echoPIV was performed on every 5th frame (effective frame rate of 1000).

2.2.4. ANALYSIS & STATISTICS

A ground truth velocity profile was calculated using the Hagen-Poiseuille equation for pipes of circular cross section:

$$v_r = \frac{2Q}{\pi R^2}\left[1 - \frac{r^2}{R^2}\right] \tag{2.1}$$

where v_r is the velocity at radius r within the total pipe radius $R(r \leq R)$ and Q is the flow rate measured by the flow meter. This study compared the signal obtained from UCA and BMF with 3 different filters (none, mean subtraction and SVD rank reduction) at 3 depths (25, 50 and 100 mm) with 3 repeated experiments per group.

Bias error was defined as the Mean of the Absolute Difference (MAD) between the echoPIV derived profile and the ground truth profile. The MAD was normalized to the peak ground truth velocity allowing for comparison over different flow rates:

$$\epsilon = \frac{\sum_{i=1}^{N} |v_{PIV(i)} - v_{GT(i)}|}{(N \times \max(v_{GT}))} \tag{2.2}$$

where ϵ, v_i and N are the error, velocity (echoPIV or ground truth) at point i, and N is the total number of echoPIV sampled points (along the radius of the tube), respectively. Vectors were averaged over ten consecutive frames before calculating the MAD.

Comparison between groups were performed by means of 2-way ANOVA followed by multiple comparisons using an uncorrected Fisher's LSD in GraphPad Prism (v7.01, GraphPad Software, USA).

2.3. RESULTS

SVD filtering suppressed the tube wall and its reverberation artefacts better than mean amplitude subtraction, as depicted in Figure 2.1, where mean subtraction was not able

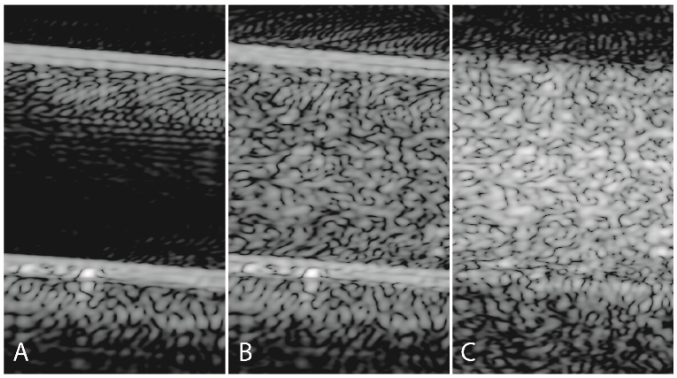

Figure 2.1: Effects of different clutter filters on BMF: A) no filter, B) mean subtraction and C) SVD. Mean amplitude subtraction fails to suppress the tiny vibrations in the tube wall (likely caused by the pumps). SVD successfully suppresses clutter. Dynamic range of 40dB.

to completely suppress the tube wall. After SVD clutter suppression, cineloops of BMF and UCA were visually similar (40dB dynamic range, Figure 2.2).

The profile estimated by echoPIV was similar to the theoretical profile calculated from the measured flow rate. This is depicted in Figure 2.3. with echoPIV vectors and theoretical ground truth overlaid on a single B-mode frame.

The effect of clutter filtration (mean over the depths and velocities sampled in this study) is summarized in Figure 2.4 Without clutter filtration UCA performed far better than BMF (27±16 % vs 67±5 % bias error, respectively). Utilizing SVD however, there was minimal difference in result, only at 100 mm depth did UCA provide improved echoPIV accuracy over BMF (13±6% vs 19±6%, p=0.005). No significant differences were observed between mean amplitude subtraction and SVD filtered echoPIV results (BMF and UCA).

With respect to Figure 2.5, depth was a significant factor in echoPIV accuracy ($p<0.0001$), with mean bias increasing with depth, even after clutter suppression using SVD filtering. Error values (using SVD) at 25, 50 and 100 mm were 4%, 12% and 19% for BMF and 5%, 9% and 13% for UCA, respectively (Figure 2.5).

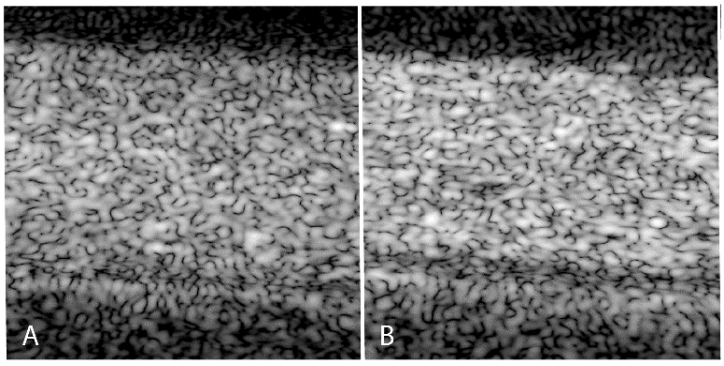

Figure 2.2: B-mode image sections of tube after SVD filtering for A) BMF and B) UCA at a dynamic range of 40 dB.

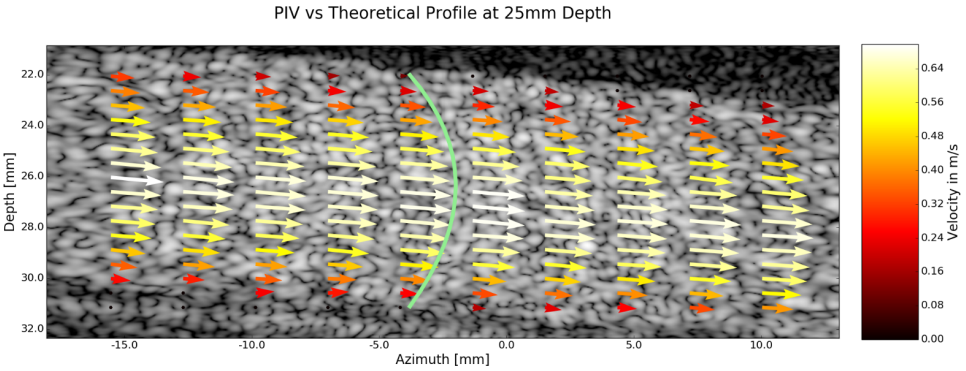

Figure 2.3: Example of echoPIV result (arrows) at 25mm depth. Green curve depicts theoretical velocity profile calculated from the measured flow meter data

2.4. DISCUSSION

2.4.1. FINDINGS

With clutter suppression, BMF provided almost equal echoPIV accuracy as UCA, except at 100 mm depth, where BMF's signal-to-noise ratio (SNR) was lower. SVD rank reduction was more effective at clutter filtering than mean subtraction, which was not able to completely suppress the signal from the tube wall due to sub-wavelength motion in the wall, induced by pump vibrations. However, the superiority of SVD in clutter suppression did not transfer to improved echoPIV results over the mean method. This was most likely due to the region of interest that was used for calculating the echoPIV, which was limited to the lumen of the tube.

With the aid of clutter suppression, echoPIV accurately estimated the velocity profile within the tube. Similar accuracy to Leow et al. (2015) was obtained when imaging at 25 mm depth [61]. However, it should be noted that in the current study no contrast specific acquisition scheme was used. Contrast specific acquisition schemes such as pulse inversion or amplitude modulation would isolate blood signal and suppress tissue signal, at the cost of reduction of the frame rates by a factor 2-3. Yet, SVD filtering already isolates blood signal, thus negating the need of a contrast mode. Alternatively, compounding techniques [58] have a similar cost of frame rate reduction, but may improve image resolution and SNR, which would likely further improve echoPIV performance.

The persistent underestimation of velocity with increasing depth was suspected to be due to the increased beam-width in the elevational direction as depth increases. In this case, with the circular cross section of the tube, causing velocity averaging of the parabolic profile over the beam width. This can readily be verified by repeating the experiments with a transducer with a deeper elevation focus.

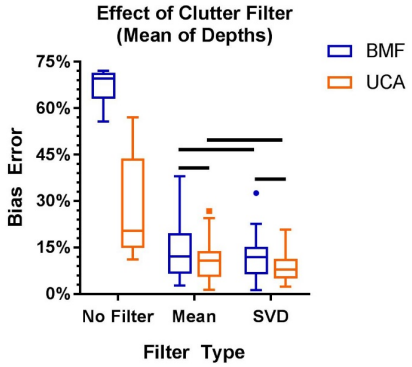

Figure 2.4: Effect of clutter filter on the resultant echoPIV bias. Using a clutter filter significantly improves accuracy for both BMF and UCA. n=9. *solid lines denote p>0.05 (no significance)

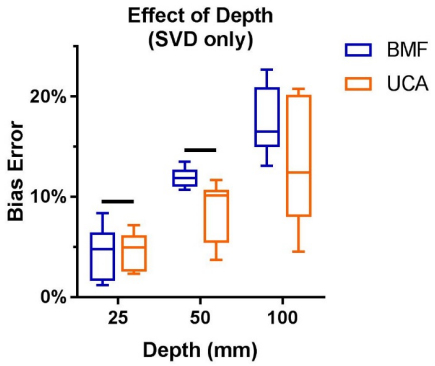

Figure 2.5: Effect of increasing depth on echoPIV bias error. For both BMF and UCA increasing depth results in increased bias error. The effect is stronger for BMF resulting in poorer performance than UCA at 100mm depth. n=9. *solid lines denote p>0.05 (no significance)

2.4.2. LIMITATIONS

The use of water as a propagation medium for ultrasound resulted in minimal attenuation and phase aberration in the ultrasound signal. It is possible that the attenuation *in vivo* will result in too low SNR from the native blood speckle for even the SVD algorithm to enhance, especially at great depth. Also, there is far more considerable tissue motion *in vivo* than the sub-wavelength vibrations experienced in the current study. It remains to be seen how well SVD separates clutter, blood and noise signal in large vessels *in vivo*. Also, the current implementation of SVD utilized a manual selection of the eigenvalues threshold, by which tissue clutter, flow signal and noise are separated. An automatically calculated threshold would be an improvement and will be explored further. Finally, the current study did not report velocities greater than 0.75 m/s, this was a limitation of the flow phantom when used with BMF and not echoPIV. When exceeding 0.75 m/s the system sucked air-bubbles into the flow medium which made comparison between UCA and BMF impossible.

2.5. CONCLUSION

The use of ultrafast ultrasound imaging in conjunction with echoPIV allowed for accurate flow velocity estimation *in vitro*. Significant improvements in echoPIV accuracy, through the addition of UCA, only occurred at 100 mm depth.

ACKNOWLEDGMENT

We acknowledge G. Springeling and A. Brouwer for their assistance in constructing the phantom.

3

HIGH FRAME RATE CONTRAST-ENHANCED ULTRASOUND FOR VELOCIMETRY IN THE HUMAN ABDOMINAL AORTA

Based on:
Voorneveld J, Engelhard S, Vos HJ, Reijnen MMPJ, Gijsen F, Versluis M, Jebbink EG, de Jong N, Bosch JG. High Frame Rate Contrast-Enhanced Ultrasound for Velocimetry in the Human Abdominal Aorta, *IEEE Transactions on Ultrasonics, Ferroelectrics, and Frequency Control* 2018;65:2245–2254. [66].

ABSTRACT

Treatment of abdominal aortic aneurysms and stenotic lesions may be improved by analyzing their associated blood flow patterns. Angle-independent blood flow patterns in the AA can be obtained by combining echo-particle image velocimetry (echoPIV) with high frame rate contrast-enhanced ultrasonography. However, echoPIV performance is affected by ultrasound contrast agent (UCA) concentration, microbubble stability and tissue clutter. In this study we assessed the influence of acoustic pressure and UCA concentration on image quality for echoPIV analysis. We also compared amplitude modulation (AM) and singular value decomposition (SVD) as tissue suppression strategies for echoPIV.

Fourteen healthy volunteers were imaged in the region of the distal abdominal aorta. We tested four different UCA bolus volumes (0.25, 0.5, 0.75 and 1.5 ml) and four different acoustic output pressures (mechanical indices: 0.01, 0.03, 0.06 and 0.09). As image quality metrics, we measured contrast-to-background ratio, bubble disruption ratio and maximum normalized cross-correlation value during echoPIV.

At mechanical indices ≥ 0.06, we detected severe bubble destruction, suggesting that very low acoustic pressures should be used for echoPIV. SVD was able to suppress tissue clutter better than AM. The maximum tracking correlation was affected by both UCA concentration and flow rate, where at high flow rates, lower UCA concentrations resulted in slightly higher correlation values but more signal drop-outs during late diastole. High frame rate echoPIV was successfully performed in the abdominal aorta of healthy volunteers and shows promise for future studies in patients.

3.1. INTRODUCTION

Study of abdominal aortic (AA) flow patterns may assist the disease-progression prediction process in patients with AA stenotic lesions and aneurysms. Several studies on stenotic lesions suggest that local flow patterns and their associated flow parameters, such as wall shear stress, have an influence on lesion development and progression [67]–[69]. In AA aneurysms, changes in flow patterns modulate inflammatory mechanisms in the vascular endothelium, causing aneurysm growth [70]. For AA aneurysms and stenotic lesions around the aortic bifurcation, *in vitro* data have shown that different treatment options generate different flow perturbations [71], [72], which can partly explain the different outcomes of these treatments. Post-treatment analysis of AA blood-flow patterns may make the follow-up schemes after endovascular treatment more patient-specific by predicting potential failure.

Investigation of blood flow patterns *in vivo* requires full field, angle independent velocity measurements. Currently, the most widely used method of assessing AA blood flow is Doppler ultrasound. However, conventional Doppler is angle dependent, which complicates imaging blood flow in regions of bifurcation, where blood flows in different directions, and where it can also flow approximately perpendicular to the ultrasound beam (70° to 110°) [13], [73].

Several ultrasonic techniques have been developed to overcome the angle dependency limitations of standard Doppler. *Vector Doppler Imaging* (VDI) splits the transmit aperture, obtaining multiple Doppler measurements at known angles to each other, from which both velocity magnitude and direction can be deduced [19], [74].

However, for imaging of deep structures, the angles between beams, and hence velocity estimates, can become unreliable due to the limited aperture [14]. *Transverse Oscillation* is a technique that also utilizes a split aperture, although usually only synthetically in receive [22]. Although originally limited to linear arrays, this method has recently been expanded to work with curved arrays, being demonstrated in the portal vein of a healthy volunteer [23]. However, the velocities expected in the AA are much higher than those in the portal vein. *Blood Speckle Tracking* can obtain angle-independent velocity measurements by tracking the speckle motion of moving red blood cells between frames [75]. It, however, requires sufficient temporal resolution for tracking the range of flows expected in the AA. High frame rate (HFR) imaging, using unfocussed transmissions, allows for the temporal resolution required for tracking high blood flow velocities, but is complicated by strong clutter in the blood-pool from surrounding tissue and reduced penetration depth compared to focused transmissions [35].

Echo-particle imaging velocimetry (echoPIV) using ultrasound contrast agent (UCA) microbubbles can be beneficial for the penetration depths required in AA flow imaging in patients (6-10 cm), since backscattered signal is greatly improved over native blood cells. We have shown previously that HFR echoPIV can accurately measure the high velocity flows which are expected in the AA, *in vitro* (**Chapter 2**). Translation to *in vivo*, however, requires further optimization of critical UCA related parameters, such as mechanical index (MI), UCA concentration and the applied tissue suppression strategy.

UCA specific acquisition sequences suppress tissue signal by exploiting the non-

linear behavior of UCA, e.g. *amplitude modulation* (AM) or *pulse inversion*. However, these sequences incur a cost in frame rate, as multiple transmissions are required to reconstruct a single image. Alternatively, singular value decomposition (SVD) based tissue suppression has been shown to perform equivalently or better than UCA specific acquisition sequences, although only for microvascular flow environments [76]. It is not yet known whether SVD also performs well in large vessels like the abdominal aorta.

The use of UCA also mandates careful tuning of the acoustic pressures used for imaging. Too-low pressures may generate insufficient signal from the bubbles; while overly-high pressures can result in bubble destruction. In both cases, velocity estimation will be compromised. The relationship between acoustic pressure and bubble destruction during HFR imaging has been reported only for *in vitro* studies [77]–[79]. It is well known that bubble stability is affected by physiological conditions. In this study we assess bubble destruction *in vivo*.

Another variable requiring optimization is UCA concentration. Higher concentrations are associated with higher signal power, but may reduce echoPIV accuracy if too high [42], [80]. Conversely, low concentrations may leave void regions, occupied only by noise. The effect of UCA concentration has not yet been studied for HFR echoPIV. In this study, we investigate the effect that tissue suppression strategy (AM versus SVD), acoustic pressure and UCA concentration have on image quality metrics for echoPIV, in healthy human volunteers.

3.2. METHODS

3.2.1. STUDY DESIGN

After approval as a pilot study, by the medical ethic committee of the Erasmus Medical Center (NL58025.078.16), 15 healthy volunteers (age 18-35 years, BMI < 25) were imaged in the region of the distal aorta with the aortic bifurcation and proximal iliac vessels in a coronal view. Four bolus injections of UCA (0.25, 0.5, 0.75 and 1.5 ml, SonoVue, Bracco S.p.A., Milano, Italy) were administered before acquiring 2.5 s of HFR ultrasound data with a research ultrasound system (Vantage 256, Verasonics Inc., Kirkland WA, USA). An additional clinical ultrasound system (Epiq 7, Philips Healthcare, Andover, MA, USA) was used to simultaneously record contrast mode image sequences in the left superficial femoral artery (downstream of the AA). HFR recordings in the AA were initiated on the research ultrasound system once the bolus was detected in the femoral artery.

After imaging the first volunteer, some minor adjustments/improvements were made to the acquisition scheme, making the data of this volunteer incomparable with the others. Measurements were performed on the remaining 14 volunteers during four measurement sessions (afternoons) in groups of 3-4.

The first three volunteers were imaged at a transmit voltage of 30V. Due to clearly visible bubble destruction on the clinical system, the transmit voltage on the Verasonics ultrasound system was decreased for subsequent volunteers, after each measurement session. Thus, three volunteers were imaged using a transmit voltage of 30V, three at 20V, four at 10V and four at 5V. The transmit voltages of 30V, 20V, 10V and 5V correspond

to MIs of 0.09, 0.06, 0.03 and 0.013, respectively (at a depth of 30-50 mm taking into account a tissue attenuation of -0.3 dB per cm).

Additionally, the volunteers underwent MRI phase contrast imaging and the detected flow was compared to the echoPIV results. This part of the study is further described in **Chapter 4**.

3.2.2. ULTRASOUND ACQUISITION & IMAGE RECONSTRUCTION

RF data were acquired with a curvilinear probe (3 MHz, C5-2, ATL, Bothell WA, USA) connected to the research ultrasound system. The AM sequence consisted of diverging waves (transmit delays all zero, single cycle pulse) transmitted with different apodization schemes (even, full, and odd elements active [39], [81]) at a pulse repetition frequency (PRF) of 3000 Hz. The sum of odd and even apodization transmissions was coherently subtracted from the full transmit to produce AM images at 1000 fps. From the full transmit acquisitions a standard B-mode sequence of 1000 fps was also generated, producing synchronized datasets for comparison. Images were beamformed into the polar domain where further analysis was performed.

3.2.3. SINGULAR VALUE DECOMPOSITION (SVD)

SVD based clutter suppression assumes that the tissue, blood and noise components of an image sequence can be separated based on their respective spatiotemporal coherence energy [62]. Tissue signal is typically higher intensity and more spatiotemporally coherent than flowing blood (and bubble) signal. Thus, when an image sequence containing blood flow and surrounding tissue is decomposed using SVD, the tissue signal accumulates more coherence energy than the flowing blood. This causes tissue to collect in the low-rank modes of the system while blood and bubbles are distributed more centrally (Figure 3.1). Noise, being relatively incoherent and low intensity, typically resides in the high-order modes. Truncating low and/or high order modes allows for selective removal of tissue and/or noise from the image sequence.

In this study, a low-rank threshold selection algorithm was used to automatically detect the transition between tissue and flowing UCA. Low-rank selection was based on the ratio of successive singular values: $\sigma_n/\sigma_{n-1} > 0.99$ (see Figure 3.1). This criterion selects the first mode n which decreases less than 1% in energy from its predecessor [82]. A high-rank cutoff was not used in this study. The number of frames used when performing SVD (ensemble length) is known to affect the separability of slow moving bubbles and tissue [76]. Thus, to assess the effect of SVD ensemble length on contrast-to-background ratio (CBR) four different SVD ensemble lengths were tested: 32, 64, 128 and 1250 frames (all frames). CBR was assessed during periods of slow flow (velocity magnitude < 0.1 m/s) and fast flow (velocity magnitude > 0.4 m/s) separately. Comparison was performed on data with MI = 0.01 only to reduce the influence of bubble disruption on the comparison.

SVD was performed on beamformed IQ data. For ensemble lengths of 32, 64 and 128, individual SVD outputs needed to be combined into a continuous set of frames. Thus, ensembles were overlapped by 87.5%, where overlapping frames from different

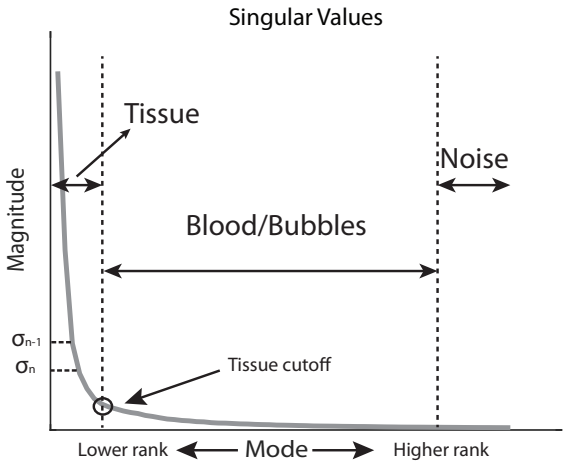

Figure 3.1: Illustration of the low-rank threshold selection algorithm used in this study. Tissue cutoff is found by searching for the point in the curve where the slope begins 'flattening out'.

SVD ensembles were averaged to create the final SVD outputs. This was not required with the 1250 ensemble as only one SVD output was created.

3.2.4. TISSUE SUPPRESSION STRATEGIES

AM was compared to SVD (ensemble length = 1250 frames) as a method for suppressing tissue signal without deteriorating the UCA signal. SVD images were computed from the B-mode sequences. Additionally, a 2nd order Chebyshev high-pass filter with a -6dB cut-off at 15 Hz was applied to the AM data, acting as a low-cutoff frequency Doppler wall-filter (AM+Cheby). SVD was also applied to the AM processed data (ensemble length = 1250 frames) as an additional group for comparison (AM+SVD), to investigate the usefulness of a combination of the two techniques.

3.2.5. CONTRAST AGENT PERFORMANCE METRICS

CONTRAST-TO-BACKGROUND RATIO (CBR)

Tissue suppression efficacy was assessed using contrast-to-background ratio (CBR) [83], defined as:

$$CBR = 20\log_{10}\left(\frac{\overline{RMS}_{B_{1-10}}}{\overline{RMS}_A}\right) \tag{3.1}$$

where $\overline{RMS}$ is the time-averaged root-mean-square signal strength in UCA (Figure 3.2: B_{1-10}) and tissue regions (Figure 3.2: A). Comparison between AM and SVD was performed during periods of slow flow (mean velocity < 0.1 m/s), which is the worst-case scenario for SVD, where bubble coherence between frames is similar to that of slowly moving tissue, increasing the likelihood that bubble signal will be removed along with the tissue signal

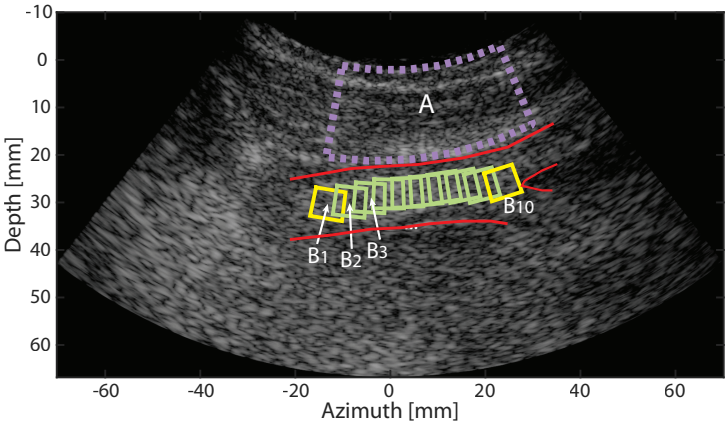

Figure 3.2: Regions used for calculating DR and CBR. Red lines indicate outlines of AA and bifurcation to iliac arteries. Purple dotted region A was used for tissue signal strength. Regions B_1 to B_{10} were used for UCA signal strength. B_1 and B_{10} were used for DR. Images displayed at 50dB dynamic range.

DISRUPTION RATIO

UCA disruption ratio (DR), a measure of acoustically driven bubble destruction, was calculated as:

$$DR = 1 - \frac{\overline{RMS}_{B_{10}}}{\overline{RMS}_{B_1}} \tag{3.2}$$

where $\overline{RMS}$ is the time-averaged RMS signal in the proximal (Figure 3.2:B_1) and distal (Figure 3.2:B_{10}) regions inside the AA. DR values range from 0 to 1, implying not any and full bubble destruction, respectively [79]. DR was calculated on the SVD processed datasets during systole only (mean velocity > 0.4 m/s) to ensure that fresh bubbles were being supplied to the region of interest.

3.2.6. BUBBLE CONCENTRATION / VELOCITY TRACKING

This section describes how the velocity and correlation values were calculated for comparison between different bolus concentrations. Velocity in the center of the vessel was estimated using normalized cross-correlation (along slow-time, frequency domain implementation) in ten regions (Figure 3.2: B_{1-10}) running along the length of the vessel. Each region was 4.7° by 6 mm in size, resulting in regions sized approximately 6 mm by 6mm, once scan converted. This size was chosen to meet the widely accepted 1/4 interrogation window rule for PIV [84]. Normalized cross-correlation was performed on the polar beamformed data after envelope detection. The maximum correlation value was used as a measure of tracking performance for different UCA concentrations. Velocity vectors were determined by finding the location of maximum cross-correlation per region (Figure 3.2. B_{1-10}). Subpixel displacement was estimated using the centroid approach [84]. Velocity vectors were scan-converted and then smoothed using a temporal moving median filter (15 ensemble length). Bubble concentrations during diastolic

(mean velocity < 0.1 m/s) and systolic (mean velocity > 0.4 m/s) phases were assessed separately, where maximum normalized cross-correlation and CBR were used for comparison.

3.2.7. ECHOPIV MEASUREMENT

A full echoPIV measurement is demonstrated on a volunteer imaged at 0.01 MI with a bolus volume of 1.5 ml, after applying a 1250 ensemble SVD filter. Four cross-correlation iterations were performed with window deformation, using interrogation areas of 9.5° x 6.1 mm and an overlap of 75% [84]. Correlation compounding was performed on three subsequent frame pairs before subpixel displacement estimation using a centroid approximation [84]. Vector fields were processed for display - at peak systole, backflow and diastole - using the dynamic visualization procedure described in [85]. Vessel boundaries were manually segmented.

STATISTICS & REPORTING

Significance of differences was statistically tested using a two-tailed Student's t-test, where a p-value < 0.05 implied significance. Results are reported as mean ± standard deviation.

For box plots: circles denote individual data points; whiskers extend to max and min values of non-outliers; boxes start and stop at first and third quartiles; solid lines denote median; and dashed lines denote mean (if present).

3.3. RESULTS

Ultrasound contrast agent (UCA) was detected in all volunteers using HFR ultrasonography with no adverse events. UCA signal could be detected using all of the tissue suppression strategies tested.

SVD ENSEMBLE LENGTH

Increasing SVD ensemble lengths resulted in increasing CBR during periods of slow flow (Figure 3.3). However, during periods of fast flow shorter ensembles resulted in higher CBR.

MECHANICAL INDEX (MI)

For AM processed data, increasing MI resulted in reduced CBR (Figure 3.4.a). Larger bolus volumes resulted in higher CBR but only for the lower MIs (0.01 and 0.02 - Figure 3.4.a). The tissue signal after AM processing increased quadratically with increasing MI (Figure 3.4.b). Higher MIs (0.06 and 0.09) caused considerably more microbubble destruction than lower MIs (Figure 3.4.c). Contrast-ultrasound recordings in the femoral artery, downstream from the HFR imaged AA, showed dips in intensity during HFR insonification for the higher MIs but not for the lower MIs (Figure 3.5).

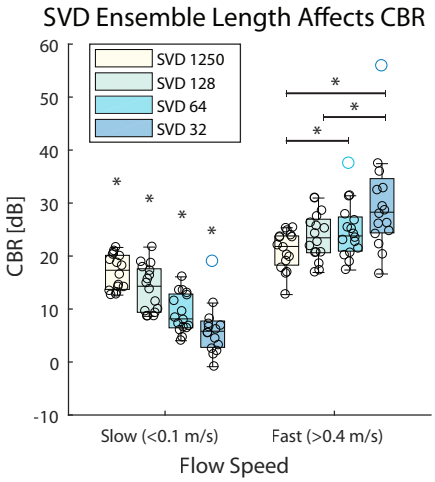

Figure 3.3: CBR values obtained with different SVD ensemble lengths during periods of slow and fast flow. Longer ensembles achieve higher CBR during slow flow. During fast flow, the opposite is true. Only 0.01 MI data was used for this comparison. n = 16 (volunteers x bolus volumes). * $p < 0.05$.

TISSUE SUPPRESSION

SVD consistently provided superior CBR values to AM and filtered derivatives of it, for all the MIs tested (Figure 3.6). No significant differences were noted between AM+Cheby or AM+SVD, although both resulted in higher CBR than AM alone, even at 0.01 MI, where AM performed at its best. Frames of each filter group at different MIs are shown during slow flow only ($|v| < 0.1$ m/s) in Figure 3.7. The average depth to the centerline of the aorta observed in these volunteers was 32±5 mm.

BUBBLE CONCENTRATION

Correlation between frames during fast flow (0.3 ±0.05) was weaker than during slow flow, independent of UCA concentration (0.7 ± 0.1, Figure 3.8.a). The 0.25 ml bolus had a lower correlation during slow flow than the 1.5 ml bolus (0.65 ± 0.14 vs. 0.79 ± 0.05, p=0.03) but a higher correlation during fast flow (0.35 ± 0.04 vs. 0.30 ± 0.02, p=0.007). Larger bolus volumes increased CBR for both diastolic and systolic flow rates (Figure 3.8.b), where systolic CBR was higher than diastolic on average (23±5 dB vs 18 ± 5 dB, respectively, $p < 0.001$). For the 0.25 ml bolus volumes, signal 'drop-outs' were observed towards the end of diastole, where bubble signal was lost in small regions. This was less prominent in higher concentrations.

ECHOPIV MEASUREMENT

Taking into account the optimization described in previous sections, echoPIV vector-fields were derived from a volunteer with an MI of 0.01 and a UCA bolus of 1.5ml. The results are shown in Figure 3.9.

3.4. DISCUSSION

High frame rate contrast enhanced ultrasonography was successfully performed in the abdominal aorta of healthy volunteers. Velocity field information could be determined

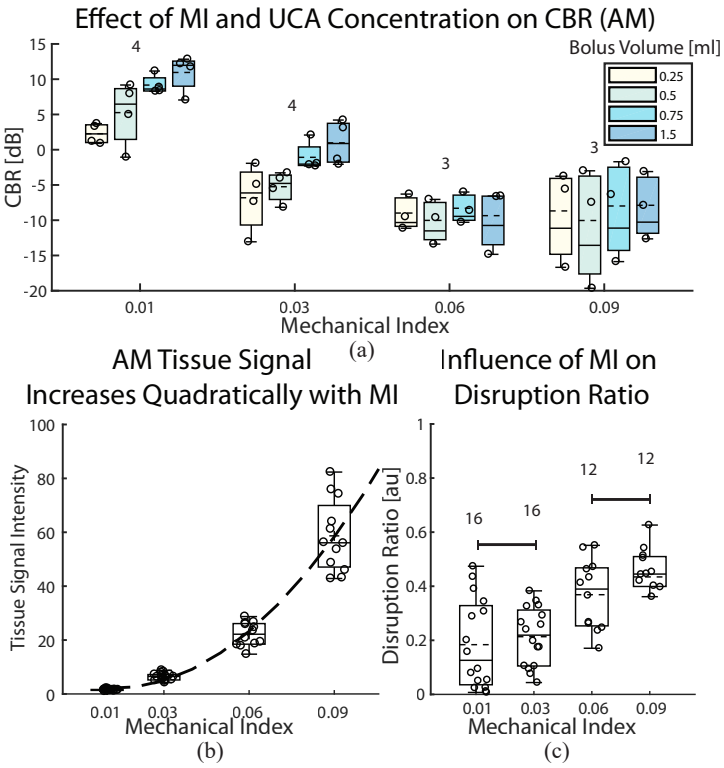

Figure 3.4: Effects of MI on CBR of AM images and DR. a) Increasing MI results in lower CBR for AM processing. At MI ≤ 0.03 larger bolus volumes result in more CBR. b) Tissue-signal intensity after AM processing increases quadratically with MI (dashed line indicates quadratic fit). c) Increasing MI results in more bubble destruction, where horizontal bars denote non-significant differences between groups. Numbers represent sample size (volunteers x bolus volumes).

using echoPIV (with the optimization described in this study) which was very similar to 4D phase-contrast magnetic resonance imaging (see **Chapter 4**).

3.4.1. SVD ENSEMBLE LENGTH

Longer ensemble lengths resulted in increased sensitivity to slow moving bubbles. This was expected as using more frames allows for more time for slow-moving bubbles to develop differences in spatial-temporal coherence from the slow-moving tissue. We also observed that shorter ensemble lengths resulted in higher CBR values for fast flow; this may be due to shorter ensembles being able to remove the pulsatile motion of the vessel wall better than long ensembles.

However, for AA applications longer ensemble lengths are preferable as their CBR is best during slow flow and sufficient during fast flow.

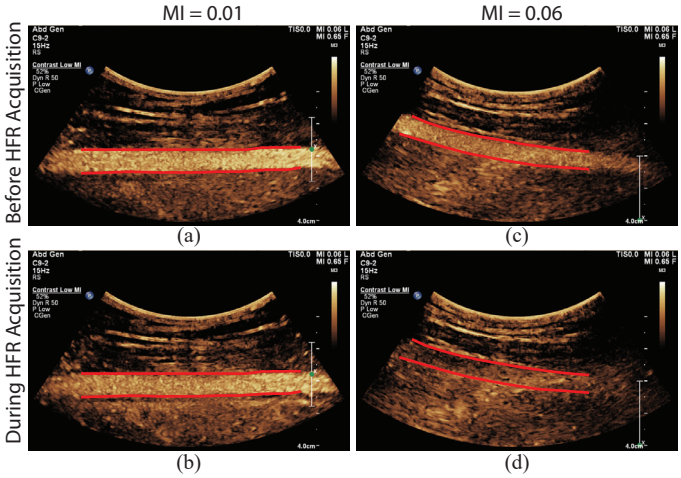

Figure 3.5: Contrast mode images recorded downstream from the abdominal aorta, in the left superficial femoral artery with a clinical ultrasound system. Images are recorded a few seconds before (a, c) and during (b, d) the high frame rate (HFR) acquisitions in the abdominal aorta, for MIs of 0.01 (a, b) and 0.06 (c, d). For 0.06 MI, note the dramatic reduction in contrast intensity before (c) and during (d) the HFR acquisition. This is not the case of 0.01 MI, where contrast intensities before (a) and during (b) HFR acquisition are very similar.

3.4.2. EFFECT OF MECHANICAL INDEX (MI)

CONTRAST-TO-BACKGROUND RATIO (CBR)

Lower MIs resulted in higher CBR values for AM processing (Figure 3.4.a). The reason is two-fold: 1) higher MI results in more bubble destruction (Figure 3.4.b); and 2) higher MI accompanied higher tissue signal (Figure 3.4.c), even after removal of the linear signal component. The reason for the increased tissue intensity is likely non-linear propagation of the pressure wave through tissue, which increases quadratically with the ultrasonic pressure applied [86]. We also observed apparent bubble signal below the AA (Figure 3.7), possibly caused by non-linear propagation through the UCA filled AA, as described in [87], [88].

DISRUPTION RATIO (DR)

We observed some differences in bubble destruction to those reported by *in vitro* studies. Couture et al. [77] reported more than 75% DR at peak-negative pressures of 0.2 MPa (~MI of 0.01 at 7.5 MHz), whereas we observed ~ 20% DR at a MI of 0.01. However, exposure time to ultrasound (~80 ms here versus 25 s used in their study) and acoustic frequencies used (3 MHz versus 7.5 MHz) were drastically different between our two studies. To the contrary, Toulemonde et al. [79] observed negligible bubble destruction at a MI of 0.1. However, their MI values were measured close to the probe, whereas here (and in [77]) MI was measured at the depth of interest (30 mm here and 20mm in [77]). Finally, *in vitro* studies do not typically account for physiological temperatures [89]–[91] and pressures [92], gas exchange between blood and UCA [93], [94] or filtration by the lungs. We found that a maximum MI of 0.03 could be used without severe bubble destruction. However, it is important to note that DR was established during periods of fast flow; during slow flow, the contrast bubbles will be exposed several times longer to ultrasound resulting in more severe bubble destruction in a given region. Therefore, the lowest MI is preferred. In further research, even lower MI values could be tested

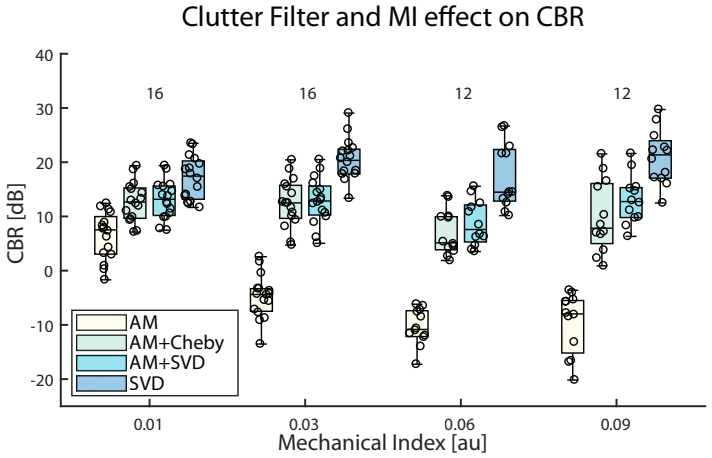

Figure 3.6: CBR values for increasing MI and different contrast enhancement schemes (clutter filters). SVD is consistently superior to AM, AM+Cheby and AM+SVD. Note that while AM CBR reduces with increasing MI, AM+Cheby and AM+SVD do not. CBR calculated during periods of slow flow only (velocity < 0.1 m/s). Numbers represent sample sizes (volunteers x bolus volumes).

3.4.3. AMPLITUDE MODULATION VS. SINGULAR VALUE DECOMPOSITION

SVD achieved higher CBR values than AM (Figure 3.6 and Figure 3.7). Even when combined with a very 'mild' wall filter (AM+Cheby), AM performed worse than SVD. We also tested how applying SVD to AM processed images would compare to SVD on a B-mode image. From Figure 3.7.c, it appears that AM+SVD provides higher signal intensities. However, Figure 3.6 shows that SVD alone provides higher CBR values than AM+SVD. AM processing reduces the signal level and introduces additional noise during the coherent subtraction process of the AM sequence, which both deteriorate CBR.

Although SVD performed well on this data, with small amounts of non-rigid tissue motion, it may not perform so well where tissue motion is relatively large, e.g. the motion of the heart valves and wall in echocardiography.

CBR is not the only factor worth considering in the comparison between AM and SVD. AM needs at least two transmissions to produce an image; we implemented a commonly used three-transmission sequence which overcomes a limitation in the research ultrasound system to quickly switch between different transmit voltages. SVD can be applied to single transmission sequences, as performed in this study. Thus higher frame rates can be achieved when using SVD alone, or angular compounding can be used to reduce side-lobe levels, increasing both resolution and contrast [95]. However, it should be noted that coherent compounding of angular transmissions in the presence of fast moving scatterers is not straightforward, as decorrelation of the scatterers between different angles causes strong imaging artefacts [96]. Alternatively, for echoPIV applications, the compounding of individual angles can be performed in the correlation domain [97] (Described in **Chapter 5**).

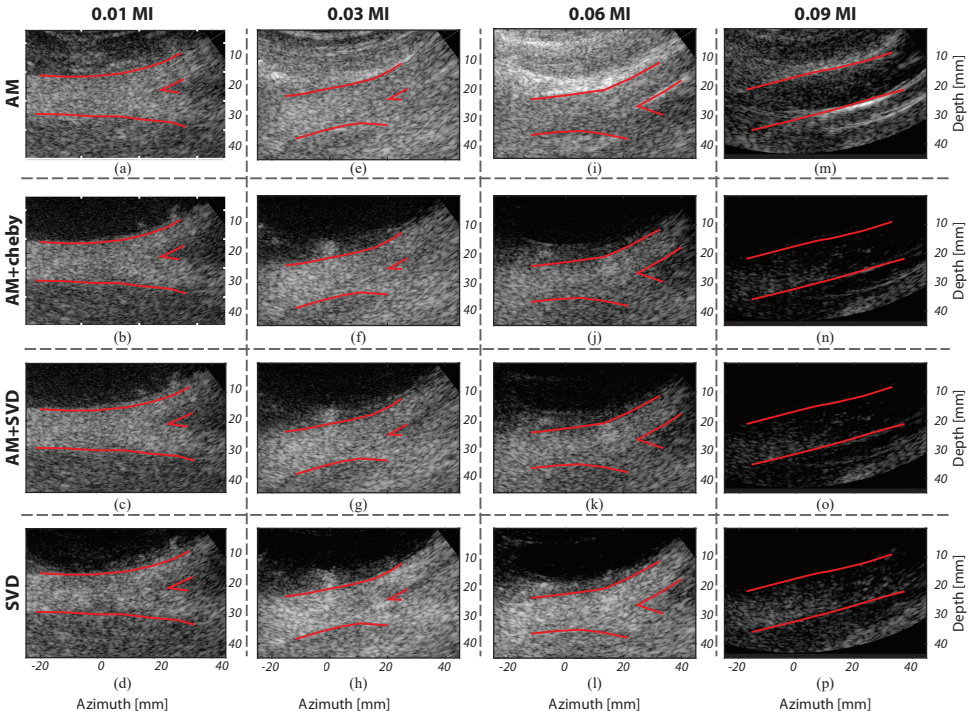

Figure 3.7: AM, AM+Cheby, AM+SVD and SVD processed frames during slow diastolic flow (<10 cm/s) for the MIs studied (different volunteers). Bolus volume was 1.5 ml. Red lines indicate vessel boundaries. Higher MI results in higher AM tissue signal power and increased bubble destruction (left column to right column). SVD processing produces higher CBR than AM and its filtered derivatives. Images displayed at 50dB dynamic range and normalized individually.

3.4.4. UCA CONCENTRATION

The mean correlation values obtained during fast flow were much lower than during periods of slow flow, independent of UCA concentration. This was expected as more bubbles will exit (and enter) the interrogation region as the flow rate increases. Additional factors linked to flow speed, such as large flow gradients or out-of-plane flow can also reduce the correlation value obtained. There are methods to account for these effects: including the use of different size interrogation windows between frames; or the use of iterative block-matching schemes with window offset and/or deformation [84] (as was used to obtain the results in Figure 3.9).

We found that high UCA concentrations facilitated higher correlation during low flow rates and vice versa. The reason for poor performance of low bubble concentrations during slow flow was likely the lower CBR during slow flow (Figure 3.8.b). The CBR decrease during slow flow was likely due to more bubble destruction, caused by the increased ultrasound exposure time. Indeed, we observed distinct regions with signal loss, particularly during late diastole, which were more prominent in the 0.25 ml bolus data than in the 1.5 ml bolus data. Thus, for low concentrations, these signal drop-outs during slow

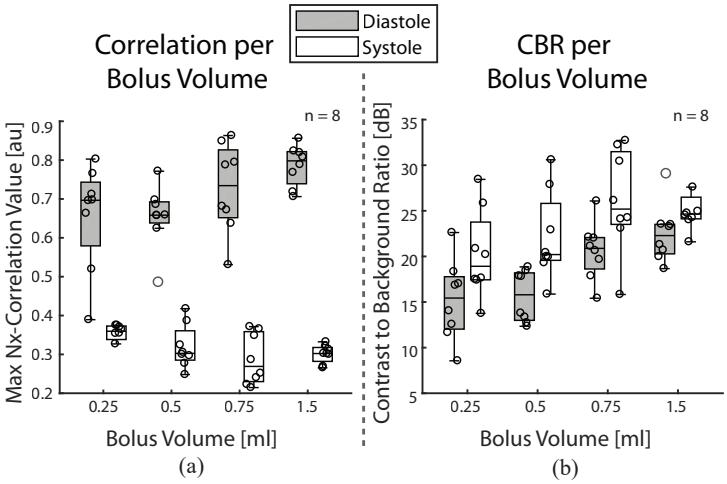

Figure 3.8: Effect of increasing UCA concentration (bolus volume) on a) maximum normalized cross-correlation values and b) CBR. During fast flow, low concentrations result in slightly stronger correlation between frames than high concentrations. However, during periods of slow flow the opposite was true. Numbers represent sample sizes (number of volunteers).

flow may outweigh the small correlation improvements during fast flow, as the drop-outs result in significant tracking error.

The small correlation improvement gained by low UCA concentrations during fast flow is in agreement with *in vitro* studies using conventional line-scanning ultrasound for echoPIV [42], [80]. Likely caused by less 'particle-pairs' being present in an interrogation window which reduces correlation uncertainty in the presence of strong flow gradients.

3.4.5. LIMITATIONS

This study did not test other non-linear contrast specific tissue suppression strategies, such as pulse inversion or power modulated pulse inversion (PMPI), which may have performed better with a different transducer. However, Desailly et al. (2017) reported similar results to this study when comparing SVD with PMPI in a microvasculature environment [76].

The volunteers in this study had lower BMI than anticipated in the patients of interest, with relatively superficial aortas (32±5 mm) compared with the depths that can be expected in patients (up to 100 mm, sometimes deeper). However, this preliminary study aimed to prove that HFR echoPIV was possible in the region of the AA bifurcation, and to gain insight into optimal UCA parameters for future patient studies. The acoustic pressures required to obtain sufficient signal were also very low, thus the transmit power can be increased to obtain similar MIs in deeper regions. How echoPIV is affected by the increased attenuation and reduced image quality in patients will be assessed in future studies.

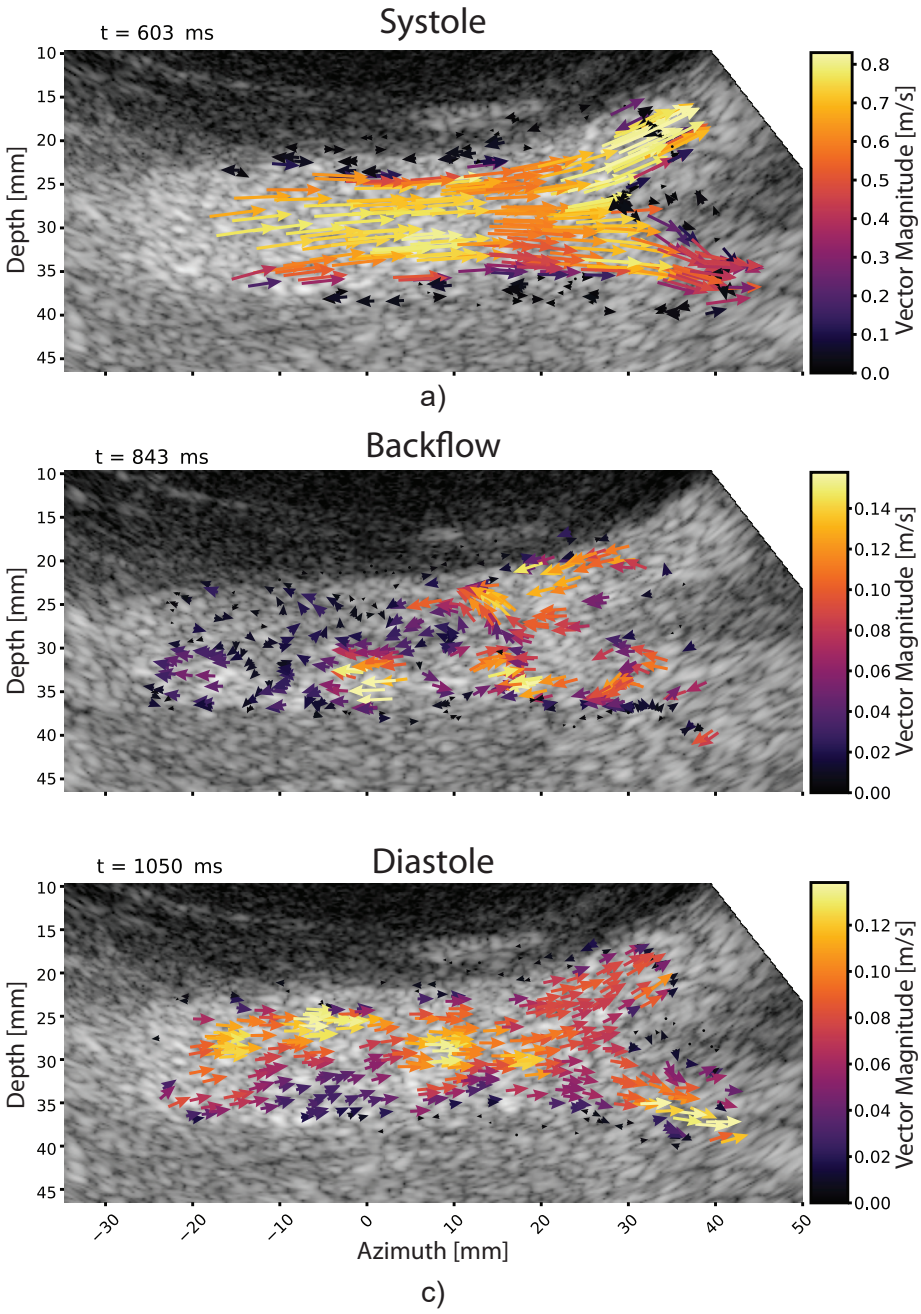

Figure 3.9: EchoPIV derived velocity fields during three phases of the cardiac cycle: a) peak systole, b) backflow, and c) diastole. Results obtained with 0.01 MI, 1250 SVD ensembles and 1.5 ml UCA bolus.

We tested lower MIs only after discovering that the planned MI of 0.09 (derived from previous in-vitro studies) was causing severe bubble destruction *in vitro*. This forced a parameter adjustment for the following batches of volunteers, but allowed us to assess the influence of MI, which was beneficial for the final outcome. For future HFR CEUS studies, *in vitro*, one should be prepared to use very low MI, maybe even lower than the values used here.

The use of the normalized cross-correlation value as a surrogate for tracking performance is also a limitation of this study, although this is not uncommon [80]. This was required as reliable ground truth measurements were not feasible *in vitro*.

Finally, the PRF used in this study was not as high as physically possible, but was limited to keep spatial-peak temporal-average intensity (ISPTA) under the recommended value for abdominal imaging [98]. We performed our ISPTA safety measurements to allow for the maximum MI value tested, resulting in an ISPTA value close to the 94 mW/cm^2 recommended for abdominal imaging. The use of the lower output pressures (MI $\leq$ 0.01) in this study would allow for a higher PRF in future, possibly up to the physical maximum of ~8000 Hz at a depth of ~10 cm.

3.5. CONCLUSION

We have shown that SVD can provide higher CBR than AM in the abdominal aorta, without requiring multiple transmissions per image. We found that lower MIs should be used *in vitro* to prevent bubble destruction, as compared to *in vitro* studies. Finally, we observed that higher UCA concentrations were associated with higher correlation during slow flow conditions and less signal drop-outs, but lower concentrations were associated with slightly higher correlation under fast flow conditions.

ACKNOWLEDGMENT

We thank Bastiaan Bongers (Rijnstate Hospital, Arnhem, the Netherlands) and Pavel Taimr MD (Erasmus MC, Rotterdam, the Netherlands) for their contribution to the high frame rate contrast enhanced ultrasound scans.

4

High-frame-rate echo-Particle Image Velocimetry in the abdominal aorta: first human results

Based on:
Engelhard S, **Voorneveld J**, Vos HJ, Westenberg JJM, Gijsen FJH, Taimr P, Versluis M, de Jong N, Bosch JG, Reijnen MMPJ, Groot Jebbink E. High-Frame-Rate Contrast-enhanced US Particle Image Velocimetry in the Abdominal Aorta: First Human Results. Radiology 2018;289:119–125.[99].
Author Contribution: Data acquisition and analysis; Involved in writing of manuscript.

ABSTRACT

Purpose: *To study the feasibility of high-frame-rate (HFR) echo-particle image velocimetry (echoPIV), in the abdominal aorta.*

Materials and Methods: *Fifteen healthy participants (six men; median age, 23 years [age range, 18–34 years]; median body mass index, 20.3 kg/m^2 [range, 17.3–24.9 kg/m^2]) underwent HFR contrast-enhanced ultrasound (CEUS). Ultrasound contrast agent microbubbles were injected at incremental doses (0.25, 0.5, 0.75, and 1.5 mL), with each dose followed by ultrasound measurement to determine the optimal dosage.*

Different ultrasound mechanical index values were evaluated (0.09, 0.06, 0.03, and 0.01) in a diverging wave acquisition scheme. EchoPIV analysis was performed via pairwise cross-correlation of all captured images. Participants also underwent phase-contrast MRI. The echoPIV and phase-contrast MRI velocity profiles were compared via calculation of similarity index and relative difference in peak velocity.

Results: *Visualization of the aortic bifurcation with HFR CEUS was successful in all participants. Optimal echoPIV results were achieved with the lowest contrast agent dose of 0.25 mL in combination with the lowest mechanical indexes (0.01 or 0.03). Substantial bubble destruction occurred at higher mechanical indexes ($\geq$0.06). Flow patterns were qualitatively similar in the echoPIV and MR images. The echoPIV and MRI velocity profiles showed good agreement (similarity index, 0.98 and 0.99; difference in peak velocity, 8.5% and 17.0% in temporal and spatial profiles, respectively).*

Conclusion: *Quantification of blood flow in the human abdominal aorta with echoPIV is feasible. Use of echoPIV has potential in the clinical evaluation of aortic disease.*

4.1. INTRODUCTION

Imaging of endovascular flow patterns in the abdominal aorta is challenging but clinically relevant because of the relationship between local hemodynamics and the development of vascular diseases [100]–[102]. Conventional Doppler ultrasound enables a one-dimensional blood flow velocity estimate in the axial direction. However, because the aortoiliac bifurcation is perpendicular to the transducer, it is difficult to obtain reliable flow quantification with Doppler imaging.

In the carotid artery and the heart, echo-particle image velocimetry (echoPIV) has been used to obtain two-dimensional velocity vector fields of blood flow in the axial and lateral directions [50], [103]. With this technique, ultrasound images are acquired and used for PIV analysis. Recent developments in the use of high-frame-rate (HFR) contrast enhanced ultrasound (CEUS) have improved the possibilities of quantifying blood flow with echoPIV. However, flow velocities of approximately 1 m/s, which can be found in the human abdominal aorta, have not been successfully quantified until recently [61].

In the abdominal aorta, ultrasound imaging is complicated by loss of signal due to bowel gas or imaging depth, which could be compensated by using ultrasound contrast agents. However, little is known about the amount of contrast agent required for optimal PIV analysis. *In vitro* models at an imaging depth of 10 cm suggested the feasibility of abdominal echoPIV with HFR CEUS (**Chapter 2**). The objective of this study was to investigate the feasibility of echoPIV to visualize blood flow in the human abdominal aorta by using phase-contrast MRI as a reference.

4.2. METHODS

This prospective within-subject exploratory study evaluated 15 healthy participants. ultrasound and MR imaging were performed in all participants in February and March 2017, with participants at rest in the supine position. Inclusion criteria were as follows: age of 18–35 years and body mass index of 25 kg/m^{2}or less. Exclusion criteria were as follows: hypersensitivity to the excipients in the ultrasound contrast agent (SonoVue; Bracco, Milan, Italy), known history of cardiorespiratory diseases, uncontrolled systemic hypertension, pregnancy, and standard MRI exclusion criteria.

Volunteers who met the entry criteria were included in the study after they provided written informed consent. This study was conducted in accordance with Good Clinical Practice guidelines and was approved by an authorized institutional review board in the Netherlands (NL58025.078.16).

4.2.1. HFR ECHOPIV

EchoPIV was performed with a fully programmable Vantage 256 ultrasound machine (Verasonics, Kirkland, Wash) with a curvilinear array abdominal probe (C5–2; ATL, Bothell, Wash). Before ultrasound imaging, physical examination was performed and blood flow velocity in the distal abdominal aorta was measured with pulsed wave Doppler imaging by using an Epiq 7 ultrasound machine (Philips Healthcare, Best, the Netherlands).

A four-member research team performed the echoPIV measurements. The aortic bifurcation was visualized in a coronal oblique view by an experienced vascular technologist. The Vantage 256 ultrasound machine was controlled by a researcher (J.V.). Contrast agent was injected by a physician with experience in CEUS examinations (P.T.). The Epiq 7 ultrasound machine was also used by a researcher (S.E.) for visual contrast monitoring in the left superficial femoral artery. A stable concentration of contrast agent was used for starting the HFR CEUS measurements, and subsequent injections were given only after substantial washout of the agent.

For each measurement, images were captured for 2.5 seconds at 1000 frames per second using a three-angled diverging wave acquisition scheme (PRF = 3000 Hz). First, HFR measurement without contrast agent administration was performed. After this measurement, four incremental contrast agent doses were administered to each participant (0.25, 0.5, 0.75, and 1.5 mL) to investigate the optimal dose for echoPIV analysis. An overview of the measurement scheme is given in Table 4.1.

Table 4.1: Overview of Activities for Each Study Participant

Duration	**Action**
Examination 1: high-frame-rate CEUS (echoPIV)	
5 minutes	Physical examination and blood pressure
5 minutes	Instructions and visualization of distal aorta
	HFR control measurement (Vantage 256 machine)
5 minutes	Pulsed wave Doppler measurement (Epiq 7 machine)
5 minutes	Insertion of venous cannula
4 × 2–3 minutes	ultrasound contrast agent injections (0.25, 0.5, 0.75, and 1.5 mL)
	HFR CEUS measurements (Vantage 256 machine)
Examination 2: phase-contrast MRI	
10 minutes	Instructions and imaging preparations
1 hour	Phase-contrast MRI

4.2.2. MECHANICAL INDEX

Before the study, hydrophone pressure measurements were performed to guarantee that pressures in the ultrasound beam field were within safety limits [98] with the transducer at maximum transmitter voltage. Thereafter, transmitting voltage was set to 60% during the first participant measurements. Four measurement sessions were planned, with three or four participants per session. In each subsequent measurement session, the transmitter voltage was further reduced to investigate image contrast and microbubble behavior. The average mechanical index at a depth of 3–5 cm (depth of abdominal aorta) was calculated for each transmitter voltage used. By following this regimen, measurements were performed at mechanical indexes of 0.09, 0.06, 0.03, and 0.01 (Table 4.2).

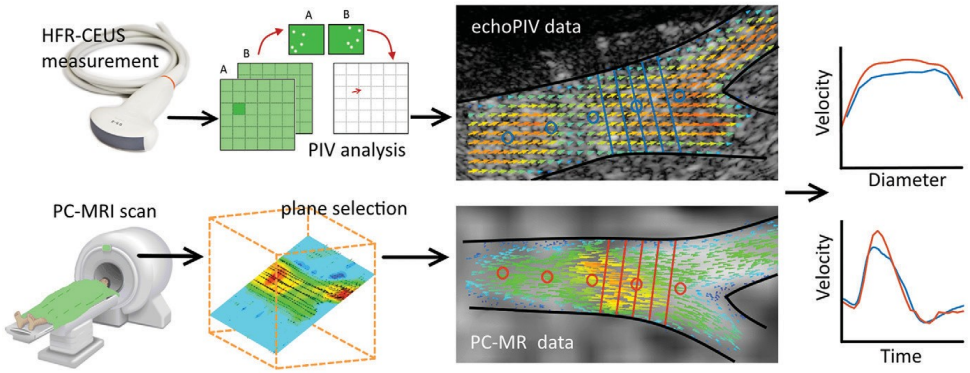

Figure 4.1: Overview of the measurement and registration method for the echo-particle image velocimetry (echoPIV) and phase-contrast MRI (PC-MRI) data. Probe locations of temporal velocity profiles (∘) and spatial velocity profiles (lines) are shown in red for PC-MRI data and in blue for echoPIV data. HFR-CEUS = high-frame-rate contrast-enhanced ultrasound.

4.2.3. DATA ANALYSIS

EchoPIV data were processed offline. Singular value decomposition–based clutter suppression was applied to each of the three transmit angles individually [62]. PIV analysis was performed by means of block-wise cross-correlation between like-angled transmissions in each image pair by using a modified version of the open-source software PIVlab (V1.41; W. Thielicke) [65]. The mean of the three resulting correlation maps was used for displacement estimation. A four-iteration cross-correlation approach was used, with a final block size of 7 × 6 mm and 75% overlap.

A 15-frame temporal moving average filter and 5 × 3 Gaussian spatial filter were applied for smoothing of the obtained velocity data. An extensive comparison of contrast agent doses, mechanical indexes, ultrasound acquisition schemes, and post-processing methods that were used in this study is reported in **Chapter 3**.

4.2.4. PHASE-CONTRAST MRI

All participants underwent phase-contrast 3.0-T MRI (Ingenia; Philips Healthcare) by using a phased-array torso coil within 1 month before or after echoPIV measurements. Multisection two-dimensional survey acquisitions were obtained to localize the distal aorta and iliac arteries. Subsequently, a three-dimensional acquisition was performed with free-breathing retrospective vectorcardiography-gated gradient-echo and echo planar imaging readout (repetition time / echo time = 8.9 ms/4.6 ms; echo planar imaging factor = 5; flip angle = 10°).

Standard four-point three-directional velocity encoding was used with Venc (maximum velocity encoding) of 150 cm/s [104]. The acquisition volume captured the aortoiliac bifurcation, including renal and external iliac arteries, with 29 reconstructed 2-mm-thick sections, resulting in a voxel size of 1.8 × 1.8 × 2.0 mm. The cardiac cycle was

reconstructed into 30 phases. True temporal resolution was 35.6 ms (ie, 4 × the repetition time).

4.2.5. COMPARISON OF ECHOPIV AND PHASE-CONTRAST MRI

Quantitative comparisons of echoPIV and phase-contrast MRI velocity data were performed. For image registration, an in-house software package (MASS) was used to visualize the three-dimensional phase-contrast MRI velocity data in manually selected planes that showed anatomic dimensions similar to the echoPIV images. Qualitative comparison of the velocity images was performed.

To extract velocity profiles, the phase-contrast MRI data were imported into Tecplot 360 EX (2016 R1; Tecplot, Bellevue, Wash), and a plane was selected by using the previously mentioned method. Further processing and comparison of the data were performed by using Matlab (R2016a; MathWorks, Natick, Mass).

Temporal velocity profiles were extracted from both data sets in five locations on the centerline of the aorta at 1 cm intervals proximal to the bifurcation apex (Figure 4.1). The time axis of the phase-contrast MRI data was matched to the echoPIV time axis. Spatial velocity profiles were extracted perpendicular to the centerline of the aorta in five locations 1–3 cm proximal to the bifurcation apex.

Cosine similarity between the shape of the temporal and spatial velocity profiles of both data sets was used as a similarity index and was calculated as follows:

$$SI = \frac{\left(V_{echoPIV}, V_{MRI}\right)}{\left|V_{echoPIV}\right|\left|V_{MRI}\right|}, \tag{4.1}$$

where $(V_{echoPIV}, V_{MRI})$ denotes the inner vector product and $|V_{echoPIV}||V_{MRI}|$ are the L_2 norms of the two vectors. Similarity index can range from −1 to 1, where a value of 1 means that the two curves are exactly the same shape (but not necessarily the same magnitude). Difference in peak velocity was calculated relative to the phase-contrast MRI data. Bland-Altman analysis was performed for the temporal peak velocities.

4.3. RESULTS

Fifteen participants (six men) were included; their median age was 23 years (range, 18–34 years), and their median body mass index was 20.3 kg/m^2 (range, 17.3–24.9 kg/m^2). Contrast agent injections and HFR CEUS measurements were successful in all participants. Adequate echoPIV results (in terms of cross correlation) were achieved in all participants for all contrast agent doses (Movie 1 [Online]). Without the ultrasound contrast agent, insufficient signal for echoPIV analysis remained after clutter suppression.

MECHANICAL INDEX

Mechanical indexes of 0.09 and 0.06 showed substantial destruction of contrast agent microbubbles in the abdominal aorta during echoPIV (Table 4.2). This resulted in contrast agent signals that were inadequate for echoPIV analysis during diastole. Bubble concentration was replenished during systole by new microbubbles entering the field of

view. Contrast agent signal also decreased in the superficial femoral artery at the exact time of the HFR CEUS measurements (Movie 2 [Online]). With a mechanical index of 0.03, some bubble destruction was visible in the HFR CEUS recordings, with no substantial signal decrease in the superficial femoral artery. Contrast agent signal during diastole was adequate for echoPIV analysis in these measurements. At a mechanical index of 0.01, no bubble destruction was observed.

As a result of contrast agent destruction, only the measurements with mechanical indexes of 0.03 and 0.01, which were performed in eight study participants, were used for comparison of echoPIV and phase-contrast MRI (with 0.25 mL of contrast agent).

Table 4.2: Mechanical Index and Bubble Destruction

		Bubble Destruction		
MI	No.	HFR CEUS Images (Abdominal Aorta)	Conventional ultrasound Images (Superficial Femoral Artery)	Adequate Contrast Signal for PIV Analysis
0.09	4	Substantial destruction	Substantial destruction	No
0.06	3	Substantial destruction	Substantial destruction	No
0.03	4	Some loss of signal	No visible destruction	Yes
0.01	4	No visible destruction	No visible destruction	Yes

Note: MI = Mechanical Index; No. = Number of participants

FLOW ASSESSMENT

Undisturbed forward blood flow was observed in all eight participants during systole for both modalities. During diastole, retrograde flow was observed with both modalities in all participants except participants 2, 7, and 8. In participants 2 and 8, only the echoPIV data showed backflow during diastole, while phase-contrast MRI data did not. The pulsed wave Doppler measurements agreed with the echoPIV measurements, showing a triphasic flow profile with a clear retrograde flow component. No significant retrograde flow was observed in participant 7 with either modality. In this participant, a period of relative blood stasis occurred during diastole. Flow patterns were similar in both the phase-contrast MRI and echoPIV data, including a recirculation zone near the origin of the left common iliac artery during diastole (Figure 4.2).

VELOCITY PROFILES

Temporal velocity profiles corresponded well between the echoPIV and phase-contrast MRI data sets (Figure 4.3). Mean similarity index was 0.98 (range, 0.96–0.99), and the mean difference in peak velocity was 8.5% (range, 0.09%–29%). Bland–Altman analysis is shown in Figure 4.4. Similar spatial velocity profiles were also found with both modalities (Figure 4.5). Mean similarity index was 0.99 (range, 0.93–1), and the mean difference in peak velocity was 17.0% (range, 4.6%–32.0%).

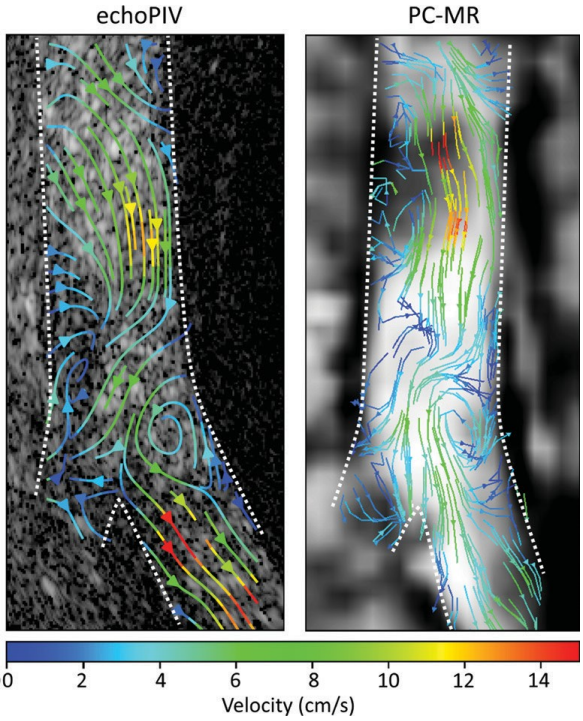

Figure 4.2: Streamline representation of blood flow velocities during early diastole in participant 7. Similar flow patterns can be observed in both data sets, including a slow (counterclockwise) recirculation zone near the origin of the left common iliac artery. This recirculation zone occurred during a longer time period in the phase-contrast MRI (PC-MR) data (five of 30 phases) than in the echoPIV data (10–15 ms). Dashed lines show estimated delineation of the vessel wall.

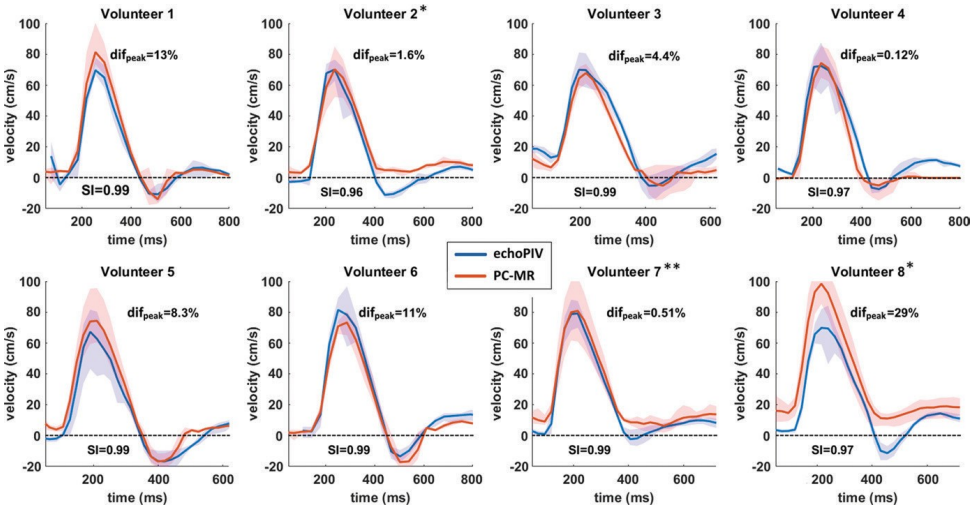

Figure 4.3: Temporal velocity profiles in eight participants. Shaded areas represent the range of measured velocities in the five probed locations. Dif_{peak} = difference in peak velocity relative to phase-contrast MRI data, SI = similarity index. ⋆ Participants in whom substantial backflow was found in the echoPIV data but not in the phase-contrast MRI data. ⋆⋆ Participant in whom no substantial backflow was found with either modality.

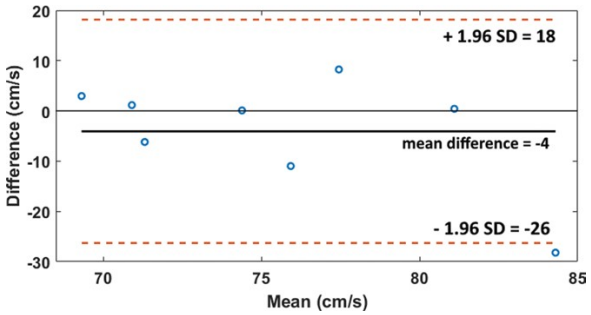

Figure 4.4: Bland–Altman plot of peak velocities in eight participants. Mean absolute difference between echoPIV and phase-contrast MRI peak velocities is 24 cm/s (echoPIV is 4 cm/s lower). The 95% confidence interval ranges from 226 to 18 cm/s. The negative mean difference is mainly caused by one outlier in the data (volunteer 8). SD = standard deviation.

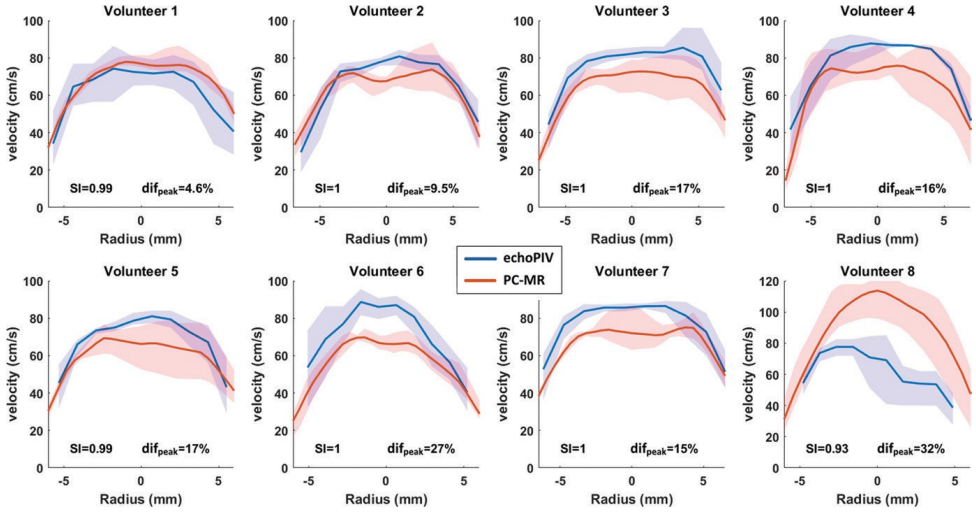

Figure 4.5: Spatial velocity profiles in eight participants. Shaded areas represent the range of measured velocities in the five probe locations. Dif_{peak} = difference in peak velocity relative to phase-contrast MRI data, SI = similarity index.

4.4. DISCUSSION

This study shows that quantification of blood flow in the human abdominal aorta is possible with echoPIV, and velocity profiles and data correspond well with those seen with phase-contrast MRI. This first-in-human study has demonstrated that assessment of flow patterns in the abdominal aorta is feasible, which can have major implications for the assessment of prognostic factors of vascular disease, indications for treatment, and clinical follow-up.

A large range of blood flow velocities, including velocities greater than 1 m/sec during systole, and very slow flow rates or blood stasis can be registered. In addition, two-dimensional vector fields of blood flow velocity can be used to evaluate flow disturbances, which is not possible with conventional Doppler imaging.

Analysis of the velocity profiles showed good overall agreement between the echoPIV and phase-contrast MRI data. Both techniques have similar spatial resolution (1.75 × 1.5 mm vector resolution and 2.6 mm ultrasound section thickness in echoPIV data versus 1.8 × 1.8 × 2.0 mm voxel size in phase-contrast MRI data), whereas the temporal resolution was 30 times higher for echoPIV (1000 frames per second in a single heart beat vs 30 phases per cardiac cycle with interleaved sampling in phase-contrast MRI data). Similar retrograde flow patterns were observed in six of eight participants studied. In participants 2 and 8, retrograde flow was observed in the echoPIV data and pulsed-wave Doppler measurements but not in the phase-contrast MRI data. This could indicate that flow quantification with echoPIV was more accurate in these participants because of a higher temporal resolution and no averaging of multiple heart cycles. However, the difference in flow patterns could also be explained by differences in body position or physiologic status of the participants during imaging.

Substantial bubble destruction occurred in the HFR CEUS measurements with a mechanical index greater than or equal to 0.06. This caused a decrease in contrast agent signal that rendered echoPIV results unreliable during diastole. These results were unexpected because no bubble destruction was observed during in vitro testing with use of similar acquisition settings and maximum transmitter voltage (mechanical index ~ 0.15) (**Chapter 2**). The reduced bubble stability in vivo could be attributed to several physiologic conditions (temperature, gas exchange, pressure) that were not accounted for in vitro [90], [92], [105].

Image registration was performed by manual extraction of a two-dimensional plane from the phase-contrast MRI data to match the echoPIV data. The ultrasound insonification plane was not recorded and could therefore not be recreated in the volumetric phase-contrast MRI data. Neighboring phase-contrast MRI planes were evaluated, showing clear differences in anatomic dimensions, whereas peak velocities showed differences of less than 10%. Thus, it is reasonable to assume that manual spatial matching of phase-contrast MRI and echoPIV data did not cause large differences in flow velocity.

In the echoPIV data, out-of-plane motion of ultrasound contrast agent and local imaging artifacts caused local decreases in correlation values and subsequent errors in the velocity vector fields. These errors were reduced by spatial smoothing, but this also removed details in the vector fields.

For echoPIV to become a clinically viable technique, further development is required in terms of ease of use, real-time data visualization, and calculation of derived flow parameters. Furthermore, prospective patient studies with echoPIV, in combination with long-term follow-up, are indicated to investigate the predictive value of these flow parameters.

In conclusion, quantification of blood flow in the abdominal aorta with echoPIV was performed in humans for the first time, demonstrating the feasibility of the technique. An optimal balance between image contrast and bubble concentration was found in a small cohort of healthy participants. The echoPIV velocity data showed good overall agreement with corresponding phase-contrast MRI data sets. Although it requires further development and validation, the echoPIV technique has great potential to enable quantitative diagnosis of vascular diseases and follow-up after treatment.

ACKNOWLEDGMENT

We thank Bastiaan Bongers for his contribution to the HFR CEUS measurements and Pieter van den Boogaard for his contribution to phase-contrast MRI.

5

HIGH FRAME RATE ULTRASOUND PARTICLE IMAGE VELOCIMETRY FOR ESTIMATING HIGH VELOCITY FLOW PATTERNS IN THE LEFT VENTRICLE

Based on:
Voorneveld J, Muralidharan A, Hope T, et al. High Frame Rate Ultrasound Particle Image Velocimetry for Estimating High Velocity Flow Patterns in the Left Ventricle. IEEE Transactions on Ultrasonics, Ferroelectrics, and Frequency Control, 2017;65(12):2222-2232. [106].

Note: In this Chapter echoPIV is referred to as ePIV to compliment the usage of oPIV for optical PIV.

ABSTRACT

Purpose: *Echocardiographic determination of multi-component blood flow dynamics in the left ventricle remains a challenge. In this study we compare contrast enhanced, high frame rate (1000 fps) echo particle image velocimetry (ePIV) against optical particle image velocimetry (oPIV, gold standard), in a realistic left ventricular phantom.*

We find that ePIV compares well to oPIV, even for the high velocity inflow jet (normalized RMSE = 9 ±1%). Additionally, we perform the method of Proper Orthogonal Decomposition, to better qualify and quantify the flow-pattern differences between the two modalities. We show that ePIV and oPIV resolve very similar flow structures, especially for the lowest order mode with a cosine similarity index of 86%.

The coarser resolution of ePIV does result in increased variance and blurring of smaller flow structures when compared to oPIV. However, both modalities are in good agreement with each other for the modes that constitute the bulk of the kinetic energy.

We conclude that high frame rate ePIV can accurately estimate the high velocity diastolic inflow jet and the high energy flow structures in a left ventricular setting.

5.1. INTRODUCTION

The left ventricular (LV) diastolic filling vortex has been suggested as a potential early-stage biomarker for cardiac dysfunction [7], [8], [107]–[111]. At present Doppler echocardiography and phase-contrast magnetic resonance (PC-MRI) are the primary techniques used for clinical assessment of LV filling dynamics. However, Doppler echocardiography is limited to assessing a single velocity component along the beam-axis; and whereas PC-MRI can resolve velocity components in 3D, its temporal resolution is limited, and acquisition is phase averaged over hundreds of cardiac cycles, resulting in the blurring of cycle-to-cycle variation, which may contain information of clinical importance [112].

Several ultrasonic techniques have emerged to measure blood flow in 2D or 3D rather than along the beam direction. *Vector Doppler Imaging* (VDI, also known as multi-angle Doppler) is one such technique developed to measure both the axial and cross-beam flow component; this is achieved by retrieving at least two Doppler measurements at a known angle to each other, which can then be used to deduce the separate flow components [74]. However, VDI requires a large aperture for imaging deep structures, which is impractical in transthoracic echocardiography due to the small intercostal windows.

Transverse Oscillation (TO) is a similar technique to VDI, in that it splits the transducer aperture, but in this case it does so synthetically by applying an apodization function in receive. TO has been used to measure LV blood flow but is limited to open-chest scanning only due to depth limitations [113], [114]. A recent variation of TO, named *Directional Transverse Oscillation* (DTO), is a method to automatically calibrate the TO technique with depth. DTO has shown reasonable accuracy at depths of up to 160 mm in pipe flow experiments, although its use in complex flow environments has yet to be demonstrated [115].

Alternatively, in a more numerical approach, *Vector Flow Mapping* (VFM) combines conventional 2D color-Doppler with tracking of the LV wall motion, and applies a mass-conservation constraint (under the assumption of planar flow) to numerically estimate the cross-beam velocity component at each point in the velocity field [29]. This technique can also be performed without LV wall motion, by splitting the flow field (assumed to be laminar) into a non-vortical and several vortical flow components; of which the axial and cross-beam velocity components can be derived [28].

Along an image-processing based paradigm, *Blood Speckle Tracking* estimates the displacement of local distributions of red blood cells (RBC) [116]. This technique has been used for flow estimation in neonates [34] and pediatric patients [35]. However, for adult cardiac applications, this technique requires a high signal-to-noise ratio (SNR) to retrieve sufficient signal from the blood, after clutter filtration. Here ultrasound contrast agent (UCA) can be beneficial, providing a large SNR improvement over the scattered signals from RBC. UCA has been widely used in a similar technique to Blood Speckle Tracking named *echo-Particle Image Velocimetry* (ePIV, also known as Ultrasound Imaging Velocimetry or UIV).

ePIV estimates the local displacement of a sparse distribution of microbubbles. However, when using focused transmission schemes, ePIV accuracy diminishes in the presence of fast flow. This is due to the relatively large scatterer displacement, and the as-

sociated speckle decorrelation, between frames [44]. The inability to resolve fast flows is especially detrimental for investigating the effect of the diastolic filling vortex, where the velocities inside the jet can exceed 1m/s. Indeed, previous left-ventricular (LV) flow phantom studies utilizing ePIV have both mentioned the limitations of the method with regard to tracking the high velocity trans-mitral jet [43], [117]. However, the recent feasibility of high frame rate (HFR) ultrasound acquisitions, using unfocussed transmit protocols, has offered a possible solution to the dynamic range limitations of ePIV.

Indeed, both our previous work (**Chapter 2**) and a study by Leow et al. (2015) [61] verified that ultrafast ePIV could accurately estimate high velocity flows in a blood vessel setting. However, these experiments do not cover the transient and multi-dimensional nature of intra-ventricular flow. Expanding on our previous work, we have developed an acoustically and optically transparent LV flow phantom to be used for optical-PIV and ultrasound (US).

In this study, we investigate whether HFR ePIV can accurately measure high velocity intraventricular flows. To do so we simultaneously acquire HFR US and time resolved digital PIV (herein referred to as optical PIV, i.e. oPIV) acquisitions at equivalent frame rates, allowing for frame-to-frame comparison between the two modalities.

5.2. METHODS

5.2.1. LEFT VENTRICULAR PHANTOM

A compliant, optically and acoustically transparent silicone LV chamber (Figure 5.1.b) was manufactured by painting four layers of silicone (HT 33 Transparente LT, Zhermack SpA, Rome, Italy) onto a 3D-printed mold of a LV. The 3D-printed mold was modelled from the statistical mean (end systolic phase) of a dataset of segmented 4D computed tomography images of 150 patients [118], [119]. The silicone LV was then fitted with mitral (Figure 5.1.b – MV) and aortic (Figure 5.1.b – AoV) Björk-Shiley valves.

The LV was encased in a transparent acrylic box and fitted with mitral and aortic valve ports, which were connected to an atrial chamber and an aortic compliance chamber, respectively (Figure 5.1). The acrylic box had one open port, which was connected to a programmable piston pump, which reciprocated in a sinusoidal pattern at a frequency of 1.0 Hz with an 80-ml stroke volume. The pump control system additionally provided a trigger pulse for synchronized acquisition between the oPIV and ePIV systems. The LV phantom design was inspired by [117], however this phantom is also designed to be MRI compatible for future research.

The LV housing had three flat and transparent surfaces for laser/camera view access, as well as an US port on the underside of the box, sealed with a thin film. The orientation of the US and laser/camera ports allow for simultaneous acquisition of oPIV and ePIV recordings.

The system works with two incompressible fluid systems: 1) the hydraulic fluid system, which is contained in the LV enclosure and transfers energy from the pump to the LV and 2) the “blood” fluid system, which flows from the atrium through the LV to the compliance chamber, slowly refilling through the return lines. The two fluid systems do

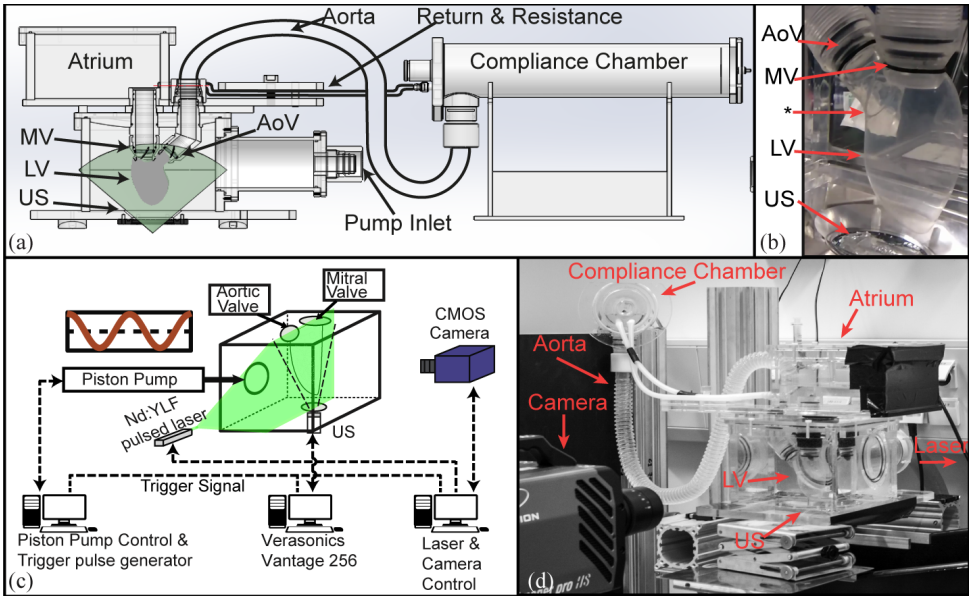

Figure 5.1: Left ventricular phantom and experimental setup. a) Diagrammatic representation of LV phantom. b) Close-up photograph of the compliant LV with aortic (AoV) and mitral (MV) valves and the US transducer through its view port. ⋆ note the opaque joint region at the start of the aortic outflow tract. c) Diagram of experiment: control of laser, ultrasound and pump are all performed with different computers and synchronization is achieved by a trigger pulse provided by the pump control system. d) Photograph of ePIV vs oPIV experimental setup.

not mix and the 'blood' fluid system dynamically pumps in response to the compression and expansion of the silicone LV wall, which follows the volume change in the hydraulic fluid system induced by the piston pump.

Both fluids were 66% glycerol in water solutions (density = 1160 kg/m^3, viscosity = 0.0177 Pa.s) to allow for correct optical index matching between the silicone of the LV and the fluid. The mismatch in density and viscosity to normal left ventricular blood values means that the Reynolds number is not matched to *in vivo* values. However, in this study we are primarily interested in capturing the diastolic, trans-mitral jet at similar velocities to those observed *in vivo* (~1 m/s).

The pump control system was not optimal, in that the pump stroke between acquisitions was not consistent. However, as oPIV and ePIV were acquired simultaneously this did not adversely affect the comparison.

5.2.2. ECHO-PARTICLE IMAGE VELOCIMETRY

ULTRASOUND SETTINGS:

Ultrasound RF data were acquired with a Verasonics Vantage 256 system (Verasonics Inc., USA) using a curvilinear (3 MHz, C5-2, ATL) probe. A single pulse-length diverging wave, 3-angled acquisition protocol was used at a pulse repetition frequency of 3 kHz;

resulting in imaging at 1 kHz after correlation compounding (see Section B.2). Datasets were acquired for 2 seconds, starting when the trigger pulse from the pump controller was received, allowing for 2 full heart cycles to be captured. Before beamforming, a 70 Hz, 8th order, high-pass Butterworth filter was applied to the channel data in the slow-time dimension to remove static clutter. The Verasonics Vantage software (V.3.0.7, all post-processing turned off) was used for IQ reconstruction, and the envelope data was used as an input for the ePIV algorithm.

An ultrasound contrast agent (UCA, SonoVue®, Bracco S.p.A) was used as a tracer particle for ePIV tracking. The UCA was injected in a 0.25 ml bolus injection, resulting in a concentration of approximately 90 μL/L.

EPIV SETTINGS:

We used a modified version of PIVlab ([65]) as an ePIV implementation in Matlab (R2017a, The MathWorks Inc., USA). This modified implementation performed block-wise cross correlation for each corresponding angle (in this case 3 angles), averaging their correlation maps before peak-finding (Figure 5.2). This was performed to reduce the decorrelation effects of bubble motion between angles.

An iterative scheme is employed where the interrogation window is resized and deformed using the displacement estimates from the previous iteration before performing the next iteration of displacement estimation. Deformation was performed using linear interpolation. Four iterations were performed in total with the first two having a kernel size of 64×64 pixels (~ 18×18 mm) and the last two refined to 32x32 pixels (~ 9×9 mm), all with an overlap of 75%. Pixel resolution was 280 μm (λ / 2) and the final grid spacing was 2.3 mm × 2.3 mm. Cross-correlation was performed in the Fourier domain and to reduce the implicit bias towards zero-displacement (caused by loss of particle pairs) the correlation maps were corrected by an appropriate window function [120].

For post processing, both local median test [121] (ϵ = 0.05, threshold = 3, b = 1) and global standard deviation (σ = 3) outlier tests were performed, replacing removed vectors with interpolated values from surrounding data. Finally, a moving average filter (5 ensembles) was applied along the time dimension of the data and a Gaussian convolu-

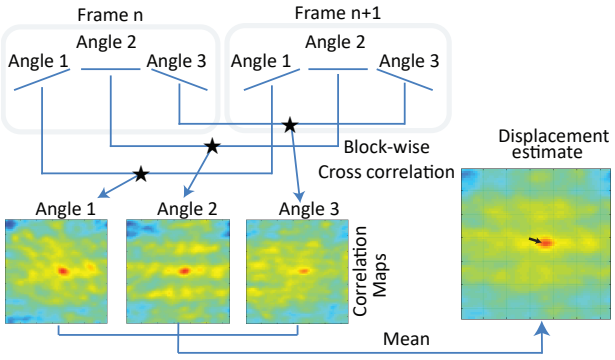

Figure 5.2: Illustration of the angle-wise cross-correlation averaging technique used for ePIV estimation. Corresponding angles between successive image frames are used for cross-correlation comparison and the mean correlation map of all angles is used for peak-finding. This process is repeated multiple times per frame-pair after interrogation window refinement and deformation.

tion filter ($\sigma = 0.5 \times 0.5$, span = 3×3) was used spatially. Table 1 provides a summary of the implementation details and parameters used for ePIV.

5.2.3. OPTICAL PARTICLE IMAGE VELOCIMETRY

oPIV was used to measure the instantaneous two-dimensional velocity field in sync with ePIV, which was performed at the same frame rate. The oPIV measurement plane was aligned to the US plane and was positioned such that both the AoV and MV would be visible in the plane, allowing for both filling and ejection dynamics to be captured. The oPIV setup is photographed in Figure 5.1.d and summarized in Figure 5.1.c and Table 1. Briefly, the oPIV setup consisted of a high-speed CMOS camera (Imager Pro HS 4M, LaVision Inc., England) equipped with a 100 mm focal length lens arranged perpendicular to the measurement plane. Image calibration was performed using a two level calibration plate (106-10, LaVision Inc.) placed in the desired measurement plane.

The camera's field of view (FOV) was adjusted to narrowly include the entire ventricle in an area of approximately 95×95 mm^2 at a focal aperture of 5.6. The measurement plane was illuminated by a high-speed dual cavity pulsed Nd:YLF laser (526 nm, LDY304, Litron Lasers, England). The laser sheet thickness was approximately 1 mm and the camera depth of field was approximately 1.8 mm. 2000 frames were acquired over a 2 second interval following the trigger signal received from the pump control system, thus synchronizing the ePIV and oPIV acquisitions.

The hollow glass spheres used as oPIV tracers were not visible in the US images, and the microbubbles used for ePIV were not visible in the oPIV images.

Vector calculation was performed using the TRDPIV package in the Davis 8.4 (LaVision Inc, England) software package. This implementation used an iterative FFT cross-correlation scheme with interrogation window refinement, ranging from 64x64 pixels down to 16×16 pixels with 50% overlap throughout. Pixel resolution was 47 μm and final grid spacing was 375 μm $\times$ 375 μm.

5.2.4. COMPARISON OF OPIV AND EPIV

The velocity profile of the primary inflow jet was used to compare the two modalities. Additionally, a technique widely used for flow feature studies in oPIV and numerical analysis called *Proper Orthogonal Decomposition* (POD), was used for comparison of the dominant flow features observed through oPIV and ePIV [122]–[124]. Using a conventional vector-to-vector analysis would require precise alignment between the ultrasound and laser scanning planes which is impractical. Using POD the dominant flow structures observed in the two datasets could be more reliably compared.

Before comparison, the oPIV dataset was spatially down-sampled (using a local mean) to match the grid spacing of the ePIV data. This made for a more meaningful comparison to the ePIV data which is an order of magnitude lower in resolution than oPIV. It was also required for POD analysis, in order to match the energy density between the two datasets.

Table 5.1: PIV Parameters

oPIV		**ePIV**	
Transmit			
Laser:	150W, 527-nm pulsed Nd:YLF	Transducer:	C5-2 (ATL)
		Center Freq.:	3.1 MHz
Pulse interval:	1 ms	Pulse Interval:	0.33 ms
Pulse Duration:	150 ns	Pulse Duration:	1 cycle
		Tx. Angles:	(-10.5°, 0°, 10.5°)
		Apodization:	Rectangular
Receive			
Camera:	2016×2016 px 12bit CMOS	US Scanner:	Verasonics Vantage 256
Sensor Size:	11 μm	No. Elements:	128
Acquisition Rate:	1 kHz	Acquisition Rate:	3 kHz
Viewing Angle:	90°	Opening Angle:	75°
Lens Focal Length:	100 mm	Elevation Focal Depth:	60 mm
FOV:	~95×95 mm^2	FOV:	110 mm × 75°
		Apodization:	Tukey (α = 0.2)
Particles			
8-12 μm hollow glass spheres		1-10 μm microbubbles (SonoVue®) 0.25 mL bolus	
Vector Analysis			
Multi-pass, normalized FFT cross correlation with window refinement		Multi-angle, Multi-pass, normalized FFT cross correlation with window refinement	
Kernel Size (px):	64×64 (2 pass) to 16×16 (5 pass)	Kernel Size (px)	64×64 (2 pass) to 32×32 (2 pass)
Overlap:	50%	Overlap:	75%
Final Grid:	375 μm × 375 μm	Final Grid:	2.3 mm × 2.3 mm
Validation and Smoothing			
Universal outlier detection		Universal outlier detection	
3×3 single pass denoising		Global standard deviation filter	
		3×3 Gaussian smoothing	
3 frame ensemble temporal moving average		5 frame ensemble temporal moving average	

5.2.5. PROPER ORTHOGONAL DECOMPOSITION (POD)

The POD technique (described in detail in [123], [125]) has been extensively used and developed in the fluid dynamics community but a brief description will be provided here.

POD analysis decomposes a time-sampled vector field into a set of orthogonal basis vectors (modes), and a set of scalar weighting coefficients (Equation 5.2). The utility of the method lies in that the modes and their corresponding coefficients are ordered in a descending manner by their energy contribution to the observed dataset. Thus, large (spatially and in magnitude) and coherent flow structures are described in the low-order modes; whereas small and incoherent flow structures are shifted towards the high-order modes. A typical POD results in the majority of energy being contained in a minority of the low-order modes. Hence, a comparison of the first few modes between decomposed datasets can reveal similarity or differences between the two datasets, largely reducing the dimensionality of the comparison problem [122], [126].

In this study the method of snapshots was used [127] which provides a discrete approximation of the POD method in the temporal domain. First the velocity grids are reorganized into a concatenated Casorati matrix $\mathbf{U}$:

$$\mathbf{U} = [\mathbf{u}^1 \mathbf{u}^2 \dots \mathbf{u}^N] = \begin{bmatrix} \mathbf{u}^1_{x_1} & \mathbf{u}^2_{x_1} & \cdots & \mathbf{u}^N_{x_1} \\ \vdots & \vdots & \ddots & \vdots \\ \mathbf{u}^1_{x_M} & \mathbf{u}^2_{x_M} & \cdots & \mathbf{u}^N_{x_M} \\ \mathbf{u}^1_{y_1} & \mathbf{u}^2_{y_1} & \cdots & \mathbf{u}^N_{y_1} \\ \vdots & \vdots & \ddots & \vdots \\ \mathbf{u}^1_{y_M} & \mathbf{u}^2_{y_M} & \cdots & \mathbf{u}^N_{y_M} \end{bmatrix} \tag{5.1}$$

where $\mathbf{u}_x$ and $\mathbf{u}_y$ are the velocity components in the axial and azimuth directions, respectively; N is the number of frames in the sequence and M is the number of vectors in the field per frame.

POD decomposes $\mathbf{U}$ into a set of orthogonal spatial modes $\mathbf{\Phi}$ and a set of temporal weighting coefficients $\mathbf{A}$:

$$\mathbf{U} = \mathbf{\Phi}\,\mathbf{A} \tag{5.2}$$

To calculate $\mathbf{\Phi}$ and $\mathbf{A}$, the covariance matrix $\mathbf{C}$ is computed:

$$\mathbf{C} = \mathbf{U}^T\mathbf{U} \tag{5.3}$$

from which the eigenvalue equation can be solved:

$$\mathbf{C}\boldsymbol{\beta} = \boldsymbol{\lambda}\boldsymbol{\beta} \tag{5.4}$$

where the eigenvalues, $\boldsymbol{\lambda}$, are ordered in decreasing amplitude. The eigenvectors $\boldsymbol{\beta}$ are used to construct the POD modes $\boldsymbol{\phi}^i$:

$$\boldsymbol{\phi}^i = \frac{\sum_{n=1}^{N} \beta_n^i u^n}{\lambda^i}, \qquad i = 1, \dots, N \tag{5.5}$$

The POD coefficients are calculated by projecting the velocity components onto the POD modes:

$$\mathbf{a}^n = \boldsymbol{\phi}^T \mathbf{u}^n \tag{5.6}$$

where $\boldsymbol{\Phi} = [\boldsymbol{\phi}^1\ \boldsymbol{\phi}^2\ \ldots \boldsymbol{\phi}^n]$ and $\mathbf{A} = [\mathbf{a}^1 \mathbf{a}^2 \ldots \mathbf{a}^n]^T$

To ensure that modes between the two datasets were comparable (i.e. shared), a combined decomposition was performed. That is, the vectors of each dataset were concatenated before POD and then reconstituted afterwards for comparison.

Similarity (**Rp**) between the POD modes of oPIV and ePIV was quantitatively assessed using the Cosine of the angle between their vectors:

$$\mathbf{Rp}^i = \frac{\left(\boldsymbol{\phi}^i_{oPIV}\ ,\ \boldsymbol{\phi}^i_{ePIV}\right)}{\left\|\boldsymbol{\phi}^i_{oPIV}\right\| \cdot \left\|\boldsymbol{\phi}^i_{ePIV}\right\|} \tag{5.7}$$

Where $(,)$ denotes the dot product of the two sets of basis functions and $\|\cdot\|$ denotes the L_2 Norm.

5.3. RESULTS

Three frames during filling and a frame during ejection are shown in Figure 5.3; where the first two columns (a-h) depict the velocity vector fields and the last two columns (i-p) depicting the calculated vorticity fields with overlaid streamlines. In Figure 5.3 (a, e, i and m) the LV is imaged shortly after MV opening. Due to the geometry of the Björk-Shiley MV two jets develop on the lateral (right) and septal (left) sides of the MV (Figure 5.3 - b and f). The primary (lateral) jet has a higher velocity than the secondary (septal) jet, and accompanying contra-rotating vortices, visible in both the oPIV and ePIV measurements. This jet develops further with the lateral (right) vortex moving slightly apically but mostly remaining in the basal region (Figure 5.3 - second and third rows). Concurrently, the septal (left) vortex migrates apically before dissipating and splitting into smaller vortices. The primary jet develops into a continuous stream over time while simultaneously reducing in velocity magnitude. The secondary jet only forms a clockwise vortex (Figure 5.3 - k and o) on the septal (left) side of the ventricle and dissipates much faster than the primary jet. During ejection (Figure 5.3 - last row), fluid is pushed towards the aortic outflow tract and fluid near the septal wall is observed to move with a higher velocity than in the center of the LV.

5.3.1. QUALITATIVE COMPARISON

The similarity between ePIV and oPIV is visible in all phases of Figure 5.3, with the exception of the ejection period where oPIV was not able to detect the velocities in the outflow tract due to the opaque joint in the silicone (Figure 5.3.d – $\star$, caused by the manufacturing procedure of the LV phantom, see Figure 5.1.b - $\star$). However, the velocities in the aortic outflow tract region were resolvable by ePIV (Figure 5.3.h).

Two tracking errors of ePIV are observed in Figure 5.3.f and Figure 5.3.g – X. Transient clutter caused by strong side-lobes of stationary air bubbles (on the LV wall) obscure the marked regions during the instances shown. The ePIV derived velocity vectors showed more frame-to-frame fluctuation than those derived from oPIV, especially in the basal region, which was in the elevational far field of the US image (>80 mm depth).

5.3.2. QUANTITATIVE COMPARISON

The ability of ePIV to capture the full range of velocities present in the field is demonstrated in Figure 5.4, where time profiles (from three separate acquisitions) through the jet cross-section are plotted for both ePIV and oPIV. Note the high level of agreement between the two temporal profiles regardless of the variation in pump-induced flow profile. Indeed, the RMSE for the three repeated profiles in Figure 5.4 was 5.5 ± 0.1 cm/s (9±1%). However, ePIV still slightly underestimates the flow when compared to the oPIV, which is reflected in a RMSE of 10±1 cm/s (16±2%), when only the high velocity ($|\bar{v}_{mean}| > 30$ cm/s) portions of the cycle are taken into account.

5.3.3. POD QUALITATIVE COMPARISON

To assess the similarity of the flow features observed by both modalities, a POD analysis was performed. The results of this analysis are shown in Figure 5.5 to Figure 5.7. Vector plots of the 5 lowest order modes for ePIV and oPIV are shown in Figure 5.5 (one row per mode).

The POD coefficient profiles, in the azimuthal and axial directions, of the 5 lowest order modes are shown in Figure 5.6. The minor underestimation of ePIV is apparent in the POD analysis, which can be seen in the axial coefficients of mode 1 (Figure 5.6 - region A), which for the most part, describes the primary jet stream (Figure 5.5 – a and f). Note that the secondary jet stream is not as prominent for ePIV as it is for oPIV in mode 1 (Figure 5.5.a and f). During ejection, oPIV is not able to resolve flow through the opaque joint region (see Figure 5.1.b - ⋆) whereas ePIV can; which is reflected in both their POD modes (Figure 5.5 - c and h) and their coefficients (Figure 5.6 - ⋆).

It should be noted that the flow profiles generated by the different modes are not necessarily real flow patterns that can be observed in the original datasets, they are instead the principal components of variation throughout the dataset, where the low order modes are of interest due to their inherent high kinetic energy. In the combined POD analysis, the first 53 modes (2.65% of the total number of modes) comprised 95% of the total energy in the decomposition.

5.3.4. POD QUANTITATIVE COMPARISON

Quantitative comparison of the two modalities can be seen in Figure 5.7.a, where the similarity index is plotted per mode along with the cumulative energy fraction (CEF). The similarity is highest for the first few modes of variation but drops off for higher order modes. The first five modes have a similarity index (**Rp**) of above 0.5. These first five modes comprise already 72% of the energy within the dataset and have an average

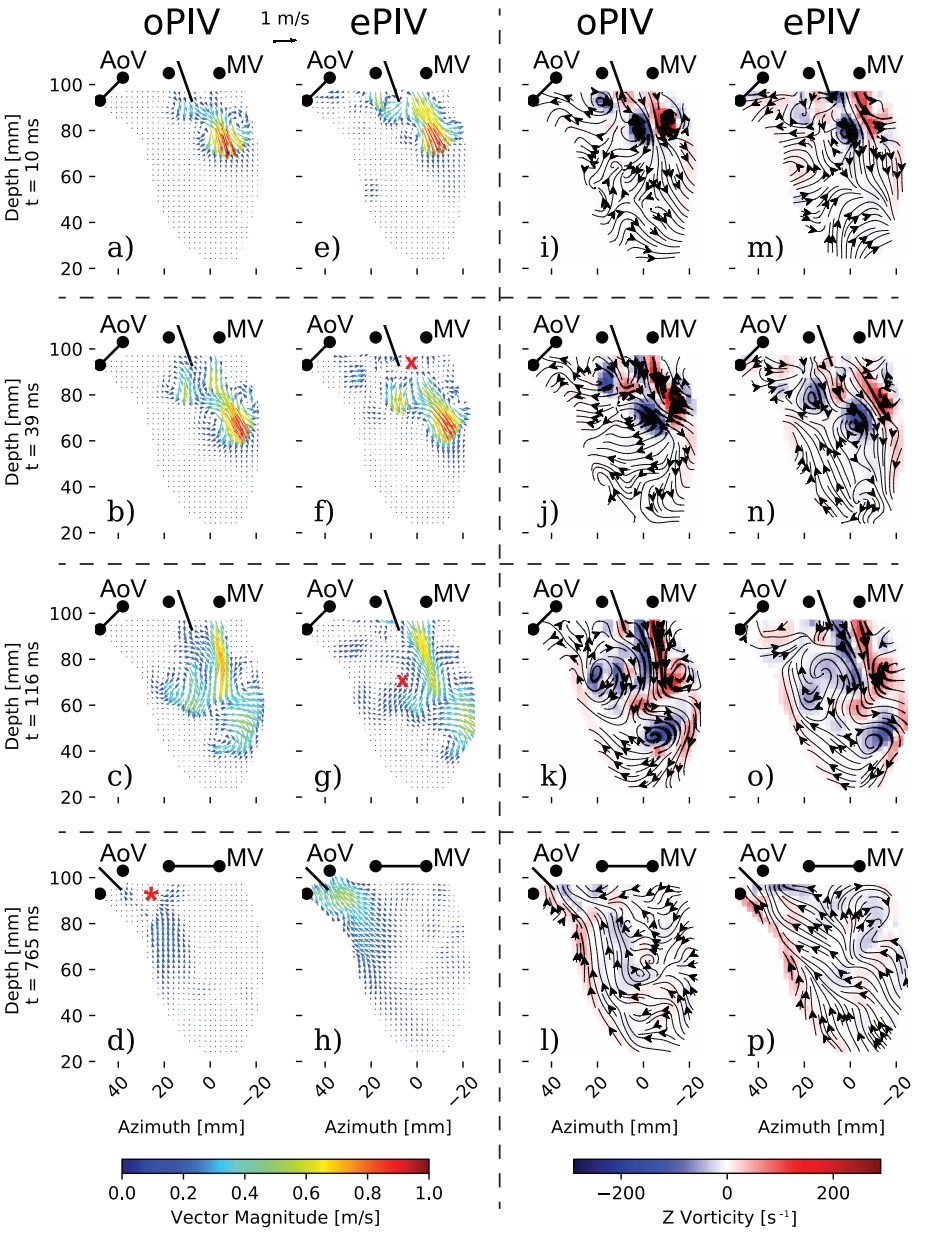

Figure 5.3: Vector field comparison between oPIV (a-d) and ePIV (e-h) during filling (a-c, e-g) and ejection (d, h).Vorticity and streamline comparison between oPIV (i-l) and ePIV (m-p). ePIV is able to capture the high velocity inflow jet, and similar flow patterns are observed. d) ⋆: Note that oPIV cannot resolve vectors in the vicinity of the opaque connection to the outflow tract (see Figure 5.1.d-⋆). g) X: ePIV tracking errors due to transient clutter artifact (see text). Black lines and dots represent the valve disks and seats, respectively (indicating a closed position when they overlap). A video showing one full cycle is available **Online**. AoV = Aortic Valve; MV = Mitral Valve

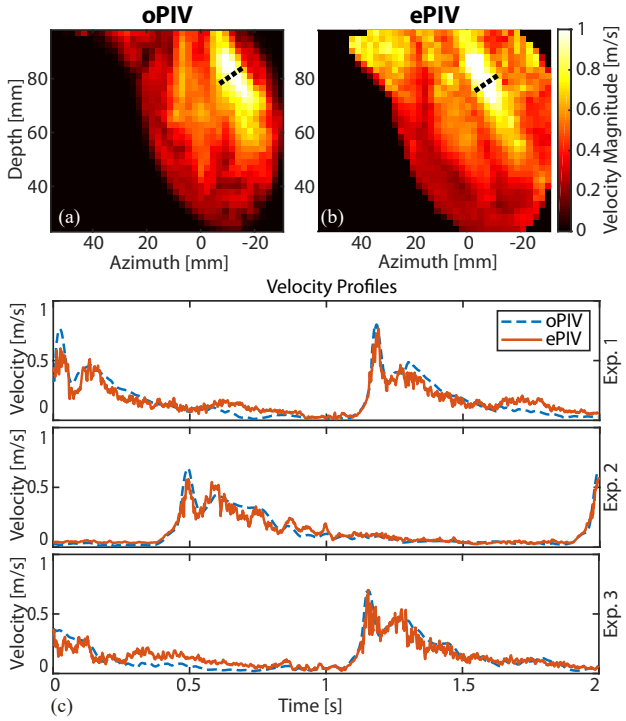

Figure 5.4: Maximum intensity projections (MIP) of the oPIV (a) and ePIV (b) time-series. c) Mean temporal velocity profiles in the jet region (of three repeated experiments), denoted by the dotted lines in a) and b), for oPIV (blue-dashed) and ePIV (orange-solid). Note the good agreement between oPIV and ePIV even though the pump-induced flow profile was inconsistent between repetitions.

similarity index of 73%. The first mode's similarity index is 86%. A sharp dip in the similarity index is seen for mode 3, which corresponds to a mode primarily associated with ejection (Figure 5.5 - c and h). Figure 5.7.b shows a similar comparison to Figure 5.7.a, except the POD decomposition was performed during frames 1-500 (filling) and 501-1000 (ejection) separately. Note the stronger similarity in filling than ejection, where there is disagreement about the ejection dynamics.

5.4. DISCUSSION

5.4.1. TRANS-MITRAL JET

Complex flow patterns, similar to those observed in LVs *in vivo*, have been measured in an *in vitro* experimental setup and a high degree of similarity was demonstrated between ePIV and the industry gold standard oPIV. Most notably, the use of high frame rate US imaging has enabled ePIV to resolve high velocity flows of approximately 1m/s; which was previously not possible with conventional scanning ultrasound acquisitions. Figure 5.3 and Figure 5.4 demonstrate that ePIV is able to resolve the high velocity trans-mitral jet. In similar LV phantom studies, where conventional scanning US based ePIV was used, the maximum detectable velocities were no higher than 0.45 m/s [44], [117].

Although the flow profiles obtained by oPIV and ePIV were similar, ePIV still slightly underestimated the trans-mitral jet velocity when compared to oPIV. The underestimation of ePIV is likely due to the order of magnitude reduction in spatial resolution be-

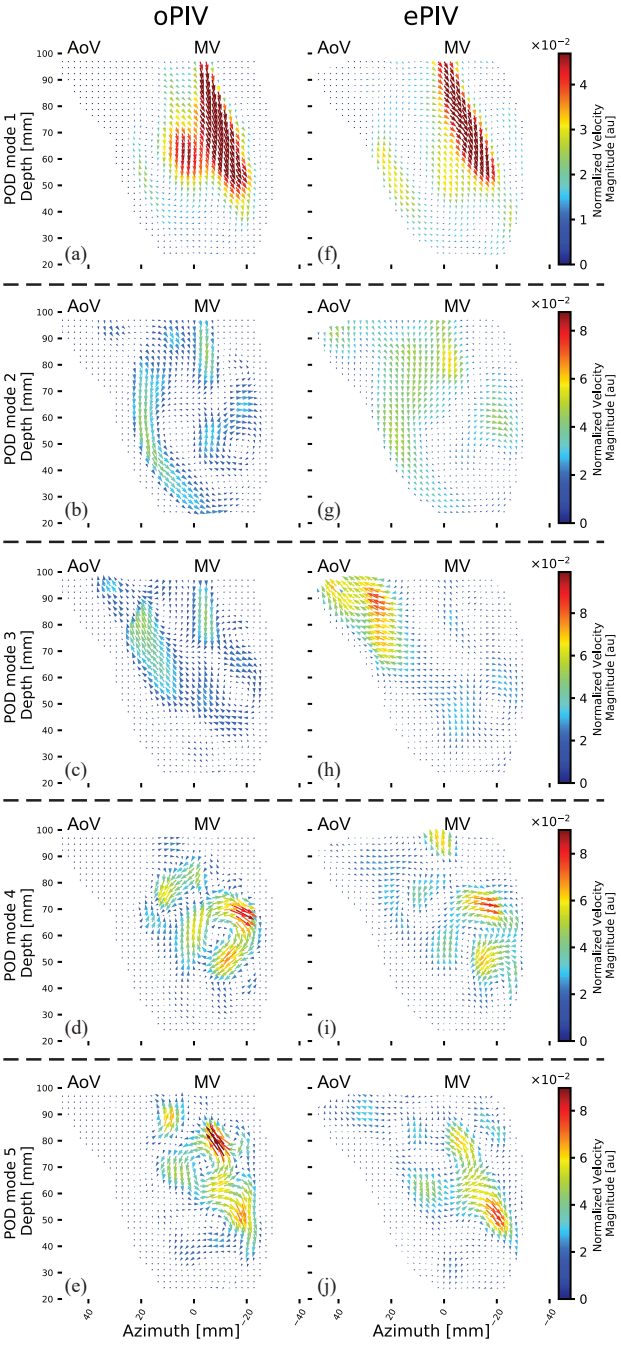

Figure 5.5: Vector map plots of the first five POD modes for oPIV and ePIV. Good agreement is noted for all modes. Mode 1: the primary jet is very similar but the secondary jet is weaker in ePIV. Mode 2: vector magnitude is more disperse for ePIV than oPIV. Mode 3: ejection dynamics captured by ePIV but not oPIV, similar to that observed in Figure 5.3.d&h. Mode 4 and 5: POD starting to describe high energy vortical structures, similarly captured for both modalities. AoV = Aortic Valve; MV = Mitral Valve

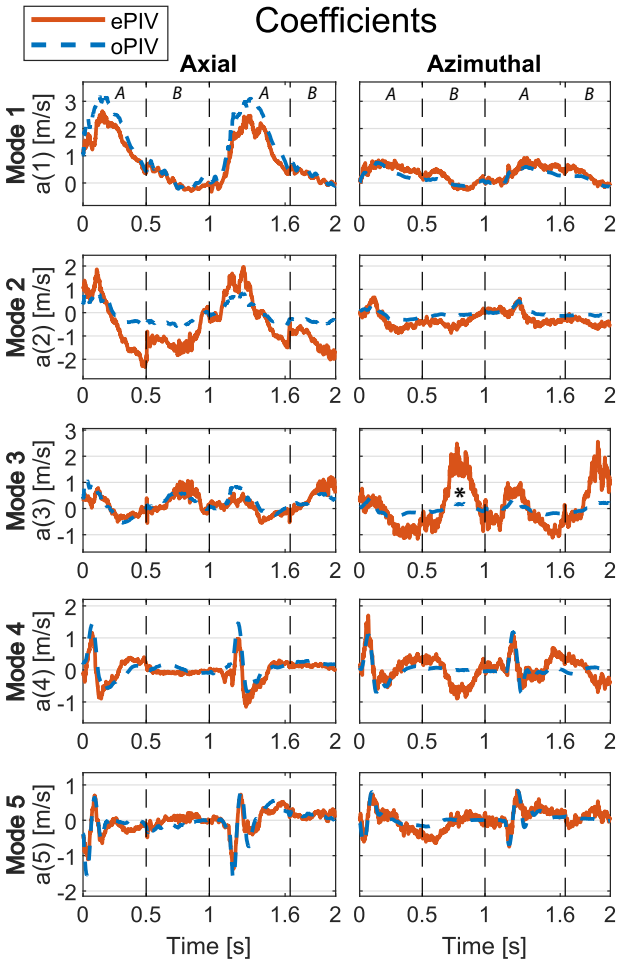

Figure 5.6: The first five POD coefficients for oPIV and ePIV in the azimuthal and axial directions. Regions demarcated between vertical dotted lines refer to periods associated with filling (A) and ejection (B). ⋆ Large difference corresponds to peak ejection period where oPIV estimate is obscured by joint region (see Figure 5.5.c and Figure 5.1.b-⋆).

tween oPIV and ePIV. The trans-mitral jet is narrow relative to the lateral resolution of the US image and the ePIV interrogation kernels, causing an averaging effect of flow in the region. Thus the flows in the high velocity, narrow jet region are averaged with the adjacent low velocity flow regions. The ePIV results were also noisier than the oPIV results. The lower SNR of the US images is likely the cause with a SNR of 18±2 dB versus 30±1 dB for the oPIV images (signal measured inside and noise measured outside the LV).

The two tracking errors (Figure 5.3.f and Figure 5.3.g - X) are caused by strong sidelobes of air bubbles on the LV wall. These air bubbles were static but moved in and out of the imaging plane with the motion of the LV wall resulting in slow-moving but transient clutter which obscured the underlying flow.

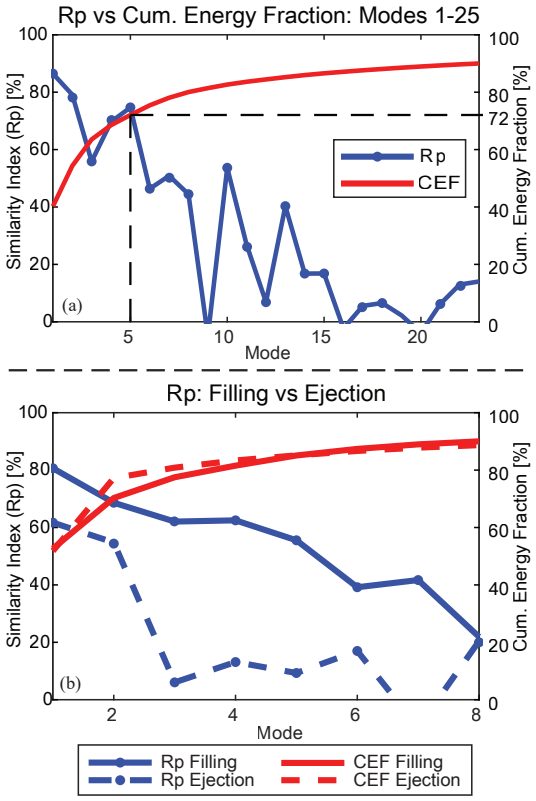

Figure 5.7: Rp similarity index versus Cumulative Energy Fraction (CEF) per mode. 90% of the energy is contained in the first 25 modes from a dataset of 2000 snapshots. Rp is strong for the first 5 modes, making up 72% of the combined energy, but drops thereafter. b) POD decompositions of filling (solid) and ejection (dashed) phases separately. Note the better similarity in filling versus ejection. This is attributed to the unresolved velocity in the outflow track for the oPIV measurements.

5.4.2. POD

POD analysis was able to show a fair agreement between oPIV and ePIV, as can be seen by their similar coefficient vectors for low order modes (Figure 5.6). The slight underestimation of ePIV is also highlighted in the axial coefficients of the first POD mode (Figure 5.6 – mode 1, A regions), which constitutes the majority of the trans-mitral jet energy. However, it can be seen that both ePIV and oPIV follow very similar flow patterns as is attested by the strong similarity indices of their low order modes.

For mode 2, the flow patterns do show some disparity, where the observed flow moving up the septal (left) wall is wider in structure for ePIV than for oPIV. Also, more flow is present near the outflow tract in the ePIV analysis, which is not present in the oPIV analysis. It may be that, for ePIV, out-of-plane flow is being registered as in-plane flow due to wider ultrasound elevational beam width in the far field.

Analyzing separate POD decompositions for the filling and ejection phases shows that the two modalities agreed more during filling than ejection. This is due to opaque joint smaller flow structures they describe) than lower order modes. Finally, the ePIV estimates were more erratic than the oPIV estimates; this would also affect the higher order modes more than the lower order modes, as the smaller, high frequency variations would collect in the higher order modes.

5.4.3. CORRELATION COMPOUNDING OF ANGLED ACQUISITIONS

Recently, high frame rate ultrasonic imaging has demonstrated value in the study of microvascular flow, where high frame rates have been shown to improve Doppler sensitivity to slow flows [62], [128]. This study uses high frame rate imaging for the opposite: to track high velocity flows.

In cardiac imaging, high frame rate ultrasound is required to maintain speckle pattern coherence between frames, so that the displacement of the microbubble distributions can be tracked. A significant difference in ultrafast processing between the two fields is that angular compounding cannot be performed on the image data, as the speckle displacements are far too large between frames. These large displacements cause loss of coherence when performing spatial (coherent) compounding. In this study, we instead perform the compounding in the correlation space (Figure 5.2), which instead of assuming negligible scatterer displacement between angles; assumes that there is negligible scatterer acceleration between angles. Spatial compounding results in severe underestimation of the trans-mitral jet, whereas correlation compounding successfully estimates the high velocity dynamics (Figure 5.8, see Figure 5.3.a for the oPIV estimate of the same frame). The superior tracking accuracy of correlation compounding over coherent compounding has also been reported in [97], where it was shown that coherent compounding failed to resolve fast flows where correlation compounding succeeded.

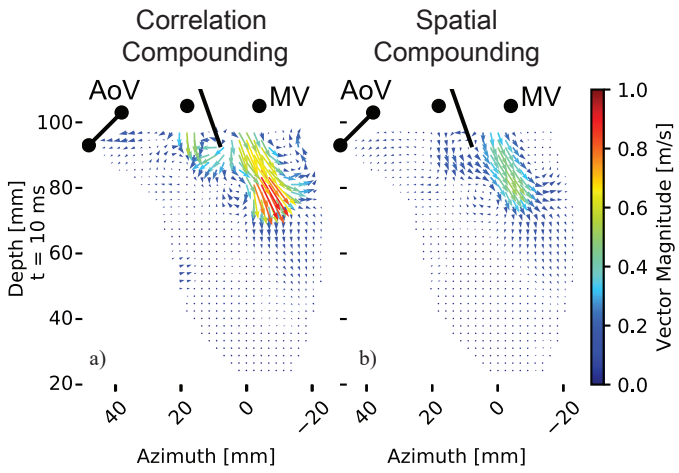

Figure 5.8: Effect of compounding angular acquisitions in the correlation domain (a) and the spatial domain (b). When angles are averaged spatially after beamforming (coherent compounding) fast moving scatterers decorrelate, degrading the signal for ePIV analysis. AoV = Aortic Valve; MV = Mitral Valve

Only three tilting angles were used in this study, initially as a compromise between speckle decorrelation and side-lobe suppression. With the use of correlation compounding more tilting angles may be viable without affecting speckle decorrelation.

5.4.4. SMOOTHING

Limited temporal and spatial smoothing was performed in this study. This was in an attempt to preserve the high velocity jet flow, which when smoothed, reduced the peak velocities detected. Decreasing the size of the interrogation windows (currently 9 mm

× 9 mm for the finest iteration) would help to reduce smoothing of the peak velocities in the jet; however, we found that halving the interrogation window size (4.5 mm × 4.5 mm) caused an increase in spurious vector results. The bubble displacement in the jet peaks at about 1.2 mm/frame, which violates the requirements of the generally accepted 'one-quarter rule' for interrogation window size [65].

Alternatively, increasing the overlap percentage (75% in this study) would increase the final grid resolution, which would generate a spatially smoother vector field (requiring less smoothing in post-processing). However, this is accompanied by a considerable computational cost. More advanced velocity field regularization algorithms may prove beneficial in preserving the high velocity flows while removing noisy fluctuations in the velocity field. E.g. Gao et al. (2015) used a Navier-Stokes based regularization scheme, however this method was sensitive to boundary conditions [117].

5.4.5. LIMITATIONS

Whereas great care was taken to align the ultrasound and laser planes, the exact orientation of the ultrasound plane could not be discerned by eye. These misalignments may mean that flow in one modality is slightly out of plane in the other. This can be alleviated by imaging in 3D, using matrix transducers for 3D ePIV, which can be validated against time resolved stereoscopic PIV. 3D imaging will also eliminate another limitation of this study which is that the velocities measured are affected by out of plane motion, where scatterers leaving the scanning plane will cause decorrelation between frames, degrading the velocity estimates.

This study assesses ePIV in an idealized *in vitro* circumstance. *In vivo* cardiac imaging will bring more challenges as image quality is further reduced due to attenuation and clutter from the ribs and lungs [129]. Furthermore, the large aperture, curvilinear probe used in this study would be impractical for transthoracic imaging. The use of a phased array probe with small aperture will bring its own challenges, such as lower resolution and a changing point-spread-function with depth due to scan conversion. These issues can be alleviated by performing the ePIV analysis in the polar domain, but this will be explored in detail in future studies.

Finally, the mechanical index of the transmission pulse used in this study was 0.09 (measured at a depth of 35 mm in 22° C water). Like in [79], this did not cause any visible bubble disruption but may require optimization for *in vivo* imaging, where physiological conditions are known to alter bubble stability [90], [93].

5.5. CONCLUSION

This study has shown that high frame rate ePIV can accurately estimate the high velocity trans-mitral jet, in an *in vitro* left ventricular setting. We have also shown that the dominant flow patterns observed by ePIV and oPIV are very similar.

ACKNOWLEDGEMENT

We thank Marcel Rutten for his valuable advice in phantom design. We acknowledge Geert Springeling, Michiel Manten, Alex Brouwer and Robert Beurskens for constructing the phantom. Special thanks to Frits Mastik for his advice throughout the study and Christiaan Schinkel for his assistance during the experiments.

6

HIGH FRAME RATE ECHOPIV CAN MEASURE THE HIGH VELOCITY DIASTOLIC FLOW PATTERNS

Based on:
Voorneveld J, Keijzer LBH, Strachinaru M, Bowen DJ, Goei JSL, ten Cate FJ, van der Steen AFW, de Jong N, Vos HJ, van den Bosch AE, Bosch JG. High Frame Rate echoPIV can Measure the High Velocity Diastolic Flow Patterns, Circulation Cardiovascular Imaging 2019; 2019;12(4). [130].

ABSTRACT

Left ventricular flow patterns may reveal signs of cardiac dysfunction at an early stage. However, standard clinically available techniques for flow estimation, such as colour and pulsed-wave Doppler, are limited to measuring only the axial velocity components. Echo-particle image velocimetry (echoPIV) can measure flow patterns in 2D, by tracking the displacement of ultrasound contrast agent microbubbles. However, echoPIV severely underestimates diastolic velocities during filling, due to the low frame rates provided by clinical scanners (using line-scanning image sequences). We show (in a patient with heart failure) that by using high frame rate echocardiography (using diverging wave sequences) echoPIV is now capable of measuring the high velocities present during diastole and also affords greater temporal resolution for studying flow patterns in the left ventricle.

6.1. INTRODUCTION

Left ventricular (LV) flow patterns have been studied as potential early stage markers of cardiac dysfunction [15]. A relatively new method of measuring LV flow patterns, named echo-particle image velocimetry (echoPIV), tracks the motion of ultrasound contrast agent (UCA) microbubbles in the blood using echocardiography. However, the low frame rates (50-70 Hz) permitted by the current generation of clinical ultrasound scanners causes velocity magnitudes to be severely underestimated during filling and ejection (<40 cm/s at 50Hz) [44]. High-frame-rate (HFR) echocardiography, using diverging-wave transmission schemes, has allowed for frame rates of up to 100 times faster than conventional line-scanning echocardiography. The image quality improvements when using HFR contrast enhanced ultrasound over conventional contrast enhanced ultrasound have recently been described [131]. Still, measurement of the high energy and high velocity trans-mitral jet has yet to be demonstrated in humans. We have shown previously, in an in vitro LV phantom study, that HFR echoPIV can accurately measure the high energy diastolic flow patterns [106]. In this work we demonstrate that this holds true in a patient with heart failure.

6.2. METHODS

A patient (19, female, 1.65 m, 66 kg) with dilated cardiomyopathy and DDD-ICD was admitted for decompensatio cordis. Apical 3-chamber views were obtained using both a clinical scanner (EPIQ 7 with X5-1 probe, Philips Healthcare, Best, the Netherlands), and a research scanner (Vantage 256, Verasonics, Kirkland, WA) with a P4-1 probe (ATL). Pulsed-wave (PW) Doppler measurements were obtained, using the clinical scanner, in the region of the mitral valve tips. UCA (SonoVue®, Bracco Imaging SpA, Milan, Italy) was then continuously infused at 0.6 ml/min (VueJect BR-INF 100, Bracco Imaging) and its arrival in the LV was verified with the clinical scanner. The research scanner was then used to obtain HFR contrast enhanced ultrasound acquisitions using a 2-angle (-7°, 7°) diverging wave sequence with 2-pulse contrast scheme (pulse inversion, mechanical index ~ 0.06 - 0.01) at a pulse repetition frequency of 4900 Hz, resulting in an imaging frame rate of 1225 Hz. EchoPIV analysis was performed in the polar domain, using custom PIV software that used correlation compounding on ensembles of 5 frames for each angle 4. The final vector-grid resolution was 1.25°by 1.25 mm. HFR echoPIV magnitudes were validated by comparing the mean temporal velocity profile to the PW Doppler spectrum captured in the same location. This study was approved by Erasmus Medical Center's medical ethics committee (NL63755.078.18).

6.3. RESULTS

The velocities measured with HFR echoPIV agreed well with the PW Doppler spectrum (Figure 6.1.a), with peak velocities up to 80 cm/s measured in this patient. This is the first demonstration of echoPIV measuring the high velocities present in the trans-mitral jet in adults. The high temporal resolution also permits study of the flow patterns in greater detail (**Supplementary Video**). For example, the large, central clockwise vortex

was observed pinching off the trans-mitral jet before migrating apically (Figure 6.1: b-d: ⋆). Smaller, more transient vortices were also observed, such as the counter-clockwise vortex between the jet and the free-wall (Figure 6.1.b: †).

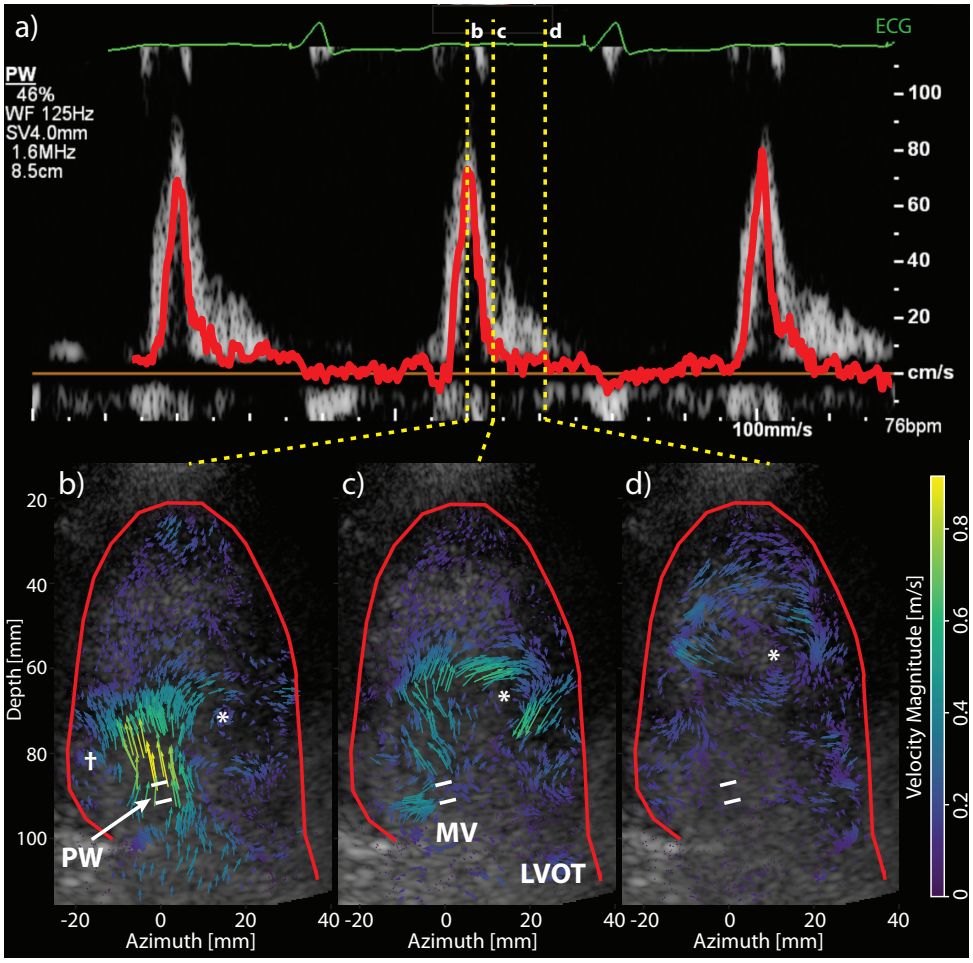

Figure 6.1: a) Mean echoPIV velocity (red) overlaid on Pulsed-wave Doppler spectrogram obtained in the mitral valve region (see PW in b). b-d) Velocity map visualization during diastolic filling (temporal locations marked in a), showing the high velocity trans-mitral jet entering the ventricle (b) and central clockwise vortex that starts basally and migrates apically (c-d). Supplementary Video included online. MV = Mitral valve, LVOT = left ventricular outflow tract. ⋆Large, persistent clockwise vortex that pinches-off the jet and migrates apically. † Small, transient counter-clockwise vortex constrained by free-wall.

6.4. CONCLUSION

We have demonstrated in a patient with heart failure that high-frame-rate echoPIV can measure the, previously unobtainable, high velocity flow patterns in 2D. This development has potential to become a useful tool in the study of intra-ventricular blood flow and its relation with ventricular function.

7

PARTICLE IMAGE VELOCIMETRY ON SIMULATED 3D HIGH-FRAME-RATE ULTRASOUND FROM PEDIATRIC MATRIX TEE TRANSDUCERS

Based on:
Voorneveld J, Bera D, Steen AFW van der, Jong N de, Bosch JG. Particle image velocimetry on simulated 3D ultrafast ultrasound from pediatric matrix TEE transducers, Proceedings SPIE Medical Imaging 2017. [132].

ABSTRACT

High-frame-rate 3D transesophageal echocardiographic (TEE) imaging, combined with 3D echo particle image velocimetry (echoPIV), would be ideal for tracking the complex blood flow patterns in the heart. We are developing a miniature pediatric matrix TEE transducer that employs micro-beamforming and allows high-frame-rate in 3D. In this paper, we assess the feasibility of 3D echoPIV with a high frame rate, small aperture transducer and the influence of the micro-beamforming technique. We compare the results of 3D echoPIV on simulated images using the micro-beamforming transducer and an idealized, fully sampled matrix transducer.

For the two transducers, we have simulated high-frame-rate imaging of an 8.4mm diameter artery having a known 4D velocity field. The simulations were performed in FieldII. 1000 3D volumes, at a rate of 1000 volumes/sec, were created using a single diverging transmission per volume. The error in the 3D velocity estimation was measured by comparing the echoPIV results of both transducers to the ground truth.

The results on the simulated volumes show that echoPIV can estimate the 4D velocity field of the arterial phantom using these small-aperture transducers suitable for pediatric 3D TEE. The micro-beamforming transducer (RMSE 44.0%) achieved comparable echoPIV accuracy to that of the fully sampled transducer (RMSE 42.6%).

7.1. INTRODUCTION

The quantification of intra-cardiac flow dynamics offers insight into cardiac function and diseases progression[9], [50]. However, Doppler echocardiography is only able to resolve one component of the complex three-dimensional flow patterns present in the cardiac chambers. *Vector Doppler*[133] and transverse oscillation[134], [135] are able to resolve two velocity components when using array probes, and can be extended to resolve all three components when using matrix probes. However, these techniques require sufficient aperture size for resolving cross-beam flow components, making imaging through the ribs or in the esophagus impractical, in the case of transthoracic echocardiography and transesophageal echocardiographic (TEE), respectively. Alternatively, echo-particle image velocimetry (echoPIV), a traditionally optical technique, instead resolves flow fields by tracking scatterer distributions between successive beamformed frames.

3D echoPIV has already been proposed for estimating intraventricular blood flow in 3D[136]. However, the high velocities (>1m/s) commonly observed in the heart are not accurately resolved due to the insufficient temporal resolution available using conventional 3D probes (< 100 volume per second).

Here high-frame-rate imaging is beneficial, as a single transmit can be used to construct a full 3D volume[137]. Understandably this results in increased data-transfer burden, which standard technology cannot yet support. Moreover, element wise delay during reception in the case of matrix transducers, with more than 1000 elements, is very challenging; where the number of channel connections in standard ultrasound systems is normally limited to 128 or 256. Therefore, we have developed a 3D TEE transducer[138], [139] with micro-beamformers (μBFs), allowing for volume acquisition rates of at least 1000 volumes/sec while reducing connection requirements by an order of magnitude.

The high volume rate achievable with this custom transducer potentially makes it suitable for 3D echoPIV estimation. However, its small aperture and the applied micro-beamforming technique may introduce limitations and/or artifacts in the echoPIV results.

Therefore, we assess the feasibility of applying 3D echoPIV to simulated 4D ultrasound volumes acquired using this small μBF transducer and a hypothetical, idealized fully sampled (FS) matrix transducer of equivalent dimensions. In this study a simple tubular flow phantom is simulated with pulsatile flow dynamics. This phantom serves as a first step before simulating cardiac flows due to its relative simplicity in development and problem solving; while still maintaining physiologically relevant flow velocities and temporal flow profiles to those observed in the heart. The performance of each transducer is assessed by comparing its echoPIV results to the known ground truth velocity profile.

7.2. METHODS

7.2.1. ULTRASOUND & TRANSDUCER SIMULATION

The micro-beamformer (μBF) transducer with a size of 5×5 mm2 and a center frequency of 5MHz has 32×32 elements of 150 μm pitch (Figure 7.1). It has 8×8 transmit elements

at its center and 864 receive elements. The receive elements are grouped into 96 3×3 sub-arrays, each with a micro-beamformer. The micro-beamformers delay and sum the sub-array signals, enabling pre-steering to 25 different angles (0°, ±17°, and ±37°in lateral and elevation direction). For this study, pre-steering was limited to 0°.

A fully sampled (FS) matrix transducer of equal size, center frequency, pitch and number of elements, but with fully addressable elements in both transmit and receive was used as a comparison for the μBF transducer.

Both probes were simulated in FieldII[140] using a spherical wave transmission, with an opening angle of ±45°, at a pulse repetition (PRF) of 1 kHz. For the FS transducer delay and sum beamforming was used for reconstructing 65×65 receive lines, covering the opening angle. In the case of the μBF transducer, two-stage beamforming was performed. First fine-delay beamforming was performed for each 3×3 sub-array, creating a single pre-beamformed signal for each sub-array (simulating the hardware of the micro-beamformers). The 96 pre-beamformed signals were then used in coarse-delay beamforming stage to reconstruct 65×65 lines in the final beamformed volume.

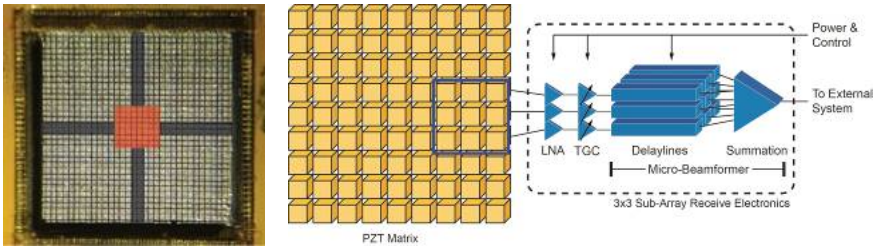

(a) (b)

Figure 7.1: μBF transducer layout. a) Picture of μBF matrix with central red highlighted area showing the 8×8 transmit elements. The vertical and horizontal grey bars indicate inactive elements. These areas contain the high voltage transmit wires to the central transmit elements. b) The remaining 864 receive elements are grouped in 96 3×3 sub-arrays with embedded micro-beamforming electronics.

7.2.2. SIMULATION OF FLOW PHANTOM

An *in-silico*, tubular blood flow phantom (Figure 7.2.A) with a diameter of 8.4 mm and 40 mm length with approximately one scatterer per cubic wavelength was simulated using a publicly available, pulsed wave femoral artery phantom[141]. The scatterers in the tube follow a Womersley flow profile (heart rate = 72 bpm, mean velocity = 0.15 m/s), producing peak pulsatile velocities between -0.2 and 1.3 m/s (Figure 7.2.B). The artery was placed in the lateral-axial plane at a depth of 50 mm and inclined at 30°with respect to the depth axis. The flow inside the artery was towards the transducer.

Scatterers were placed at random in the first frame and were displaced per their radial position within the artery and the calculated velocity field at that position. Each frame was then individually simulated in Field-II producing 1000 volumes (a sequence of one second at 1000 fps) per transducer.

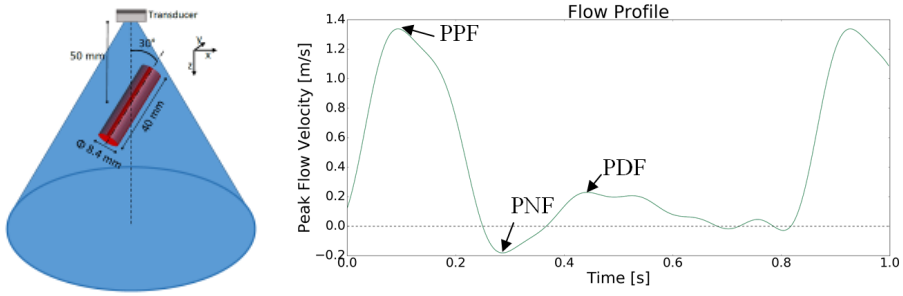

(a) (b)

Figure 7.2: a) Graphical depiction of simplified arterial flow phantom. The artery is not tilted with respect to the y-axis. b) Simulated arterial flow profile. PPF = peak positive flow; PNF = peak negative flow; PDF = peak diastolic flow

7.2.3. ECHOPIV PARAMETERS

A 3D PIV algorithm utilizing normalized cross correlation was implemented in Python. The implementation was fully vectorized, utilizing the open-source FFTW[142] library for frequency-domain based cross-correlation, allowing for 3D echoPIV estimation at ~1 fps (depending on kernel size, overlap and region-of-interest). Sub-pixel estimation was performed using a 3-point parabolic function.

For this study, echoPIV was applied in the polar domain on the beamformed envelope data derived from the Field-II simulations. The polar data was down sampled in the depth dimension and up sampled in the azimuth and elevational dimension to provide a pixel resolution of 0.3 mm × 0.35°× 0.35°in depth, azimuth, and elevation directions, respectively. Normalized cross correlation was performed with 16×8×16 pixel kernels with 50% overlap. The vessel boundaries were transformed to the polar domain to create 3D mask for preventing echoPIV estimation outside of the known flow region. For post processing: local median[121] and standard deviation filters[143] were used to remove outliers, which were subsequently replaced by trilinear interpolation of valid neighboring vectors. Finally, the vectors were temporally smoothed with a Gaussian weighted 5-point temporal moving mean filter. No spatial smoothing was applied.

The resulting vector fields were then transformed to Cartesian space for comparison with the ground truth.

7.2.4. EFFECT OF POINT SPREAD FUNCTION

To assess the effect of increasing point-spread-function (PSF) size on echoPIV results, the same simulated scatterers used in the ultrasound simulations were convolved with different sized Gaussian kernels (to reduce computational cost compared with Field-II simulation). By increasing the standard deviation of the Gaussian kernel a large PSF was simulated. Three different standard deviations were calculated: 0.5×1×1 pixels, 1×2×2 pixels and 2×5×5 pixels in the axial, azimuth, and elevational directions, respectively. The resultant volumes sequences were echoPIV processed with 8×4×8 pixel kernels with 50% overlap.

7.2.5. ERROR MEASUREMENT

EchoPIV velocity measurement error was calculated as the root mean squared error (RMSE) with respect to the ground truth (sampled from the analytical flow profile at the same coordinates as the echoPIV estimates) and expressed as a percentage of the ground truth peak velocity per frame.

7.3. RESULTS

Single 3D volumes of the scatterers and their simulated ultrasound response are shown in Figure 7.3. Grating lobes can be observed for the μBF transducer (Figure 7.3.C) which are not present with the FS transducer. The speckle point spread function (PSF) was slightly larger for the μBF transducer than the FS transducer, as was expected from previous work[144].

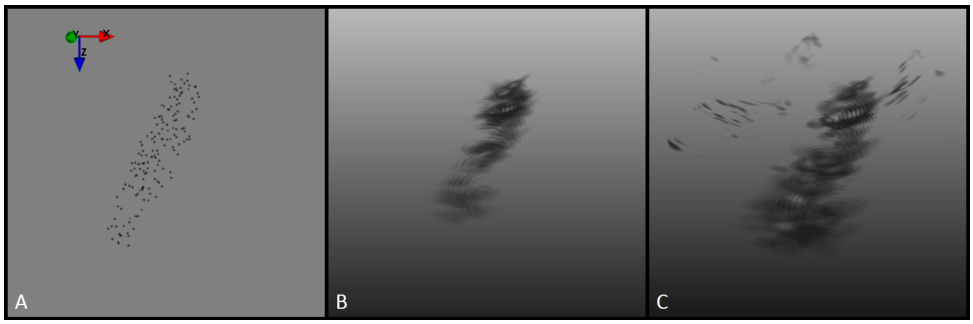

Figure 7.3: A) Scatterer placement within vessel for a single frame. B) and C) ultrasound simulations using the FS and μBF transducers, respectively. Grating lobes are more prominent with the μBF transducer.

Vector fields are depicted (Figure 7.6) at three phases of the flow-cycle, highlighted in Figure 7.2.B, for each transducer and the ground truth. For both transducers mean velocity magnitude is estimated better for periods of uniform flow (Figure 7.4 - 'A') and slower flows (Figure 7.4 - 'C' and Figure 7.6 – 'PDF'), but greatly underestimates when high spatial velocity gradients are present (Figure 7.6 – 'PPF and PNF' and Figure 7.4 – 'B'). The RMSE for both transducers over the flow cycle is depicted in Figure 7.5, where minimal difference is observed between the two (μBF = 44.0%, FS = 42.6% on average).

Figure 7 shows that by increasing the standard deviation of the convolved Gaussian kernel, the PIV velocity under-estimation increases.

7.4. DISCUSSION

This is the first time, to our knowledge, that simulations of high-frame-rate 3D ultrasound acquisitions have been used with echoPIV to estimate 4D flow. Additionally, this is the first study assessing a miniature 3D TEE transducer for 4D flow estimation capabilities. The mean temporal flow pattern estimated by echoPIV was similar to the ground truth but with underestimated magnitude in regions of fast flow or high velocity gradients (Figure 7.4 - 'B'). This study also showed that the slightly lesser image quality of the

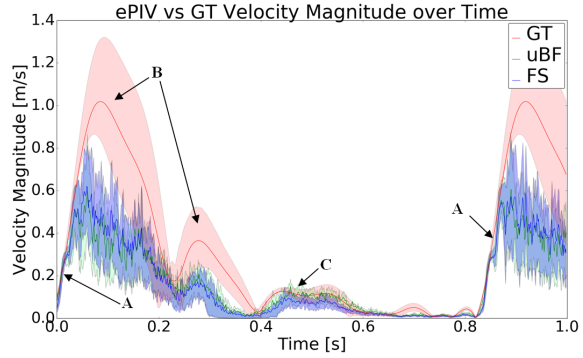

Figure 7.4: echoPIV estimated velocity magnitude for FS (blue) and μBF (green) transducers with ground truth velocity magnitude (red line) as reference. The shaded areas fill the 25th to the 75th percentile of the velocity magnitude. A) echoPIV estimation is more accurate when spatial velocity gradients are relatively low (25th and 75th percentile are close). B) When large velocity gradients are present then velocity magnitude is greatly underestimated. C) Estimation accuracy is also relatively good when flow is slow.

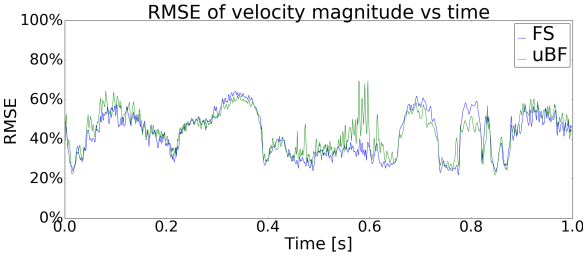

Figure 7.5: RMSE, expressed as a percentage of maximum ground truth velocity magnitude, for FS (blue) and μBF (green) transducers echoPIV results over time.

μBF transducer did not degrade the echoPIV results when compared to a FS transducer of equal dimensions.

The primary reason for the velocity underestimation is suspected to be the relatively large PSF of the transducers compared to the spatial gradients in the flow field. The resolution in the cross-beam direction is not sufficient to separate adjacent scatterers, which are travelling at different velocities due to the relatively high spatial gradients in the velocity field. This results in velocity averaging over the radius of the vessel, flattening the parabolic flow profile. Verifying this theory, the PIV analysis performed on the Gaussian-kernel-convolved scatterers (Figure 7) shows that increasing PSF accompanies more severe velocity under-estimation.

Additionally, with Fourier-domain cross-correlation methods, it has been shown that when kernels of equal size are used in both the current (t_0) and the target frame (t_1), the resultant displacement estimates have an implicit bias towards zero[143], [145]. This bias is known to increase with both increasing PSF size and inter-frame scatterer displacement[146]. This bias can be improved by implementing an iterative routine, where the velocity estimates of the prior iteration are used to offset (and optionally deform) the search area in the target frame (t_1) for the next iteration[65], [145]. Alternatively, the target frame (t_1) kernel size can be increased to reduce the information loss outside of the kernel when displacement occurs. However, this will require zero padding of the current frame (t_0) for Fourier-domain based cross-correlation methods, which may introduce unwanted high-frequency noise in the correlation space, potentially distorting the correlation signal.

Gao et al. (2013) reported a similar study where echoPIV was performed on simu-

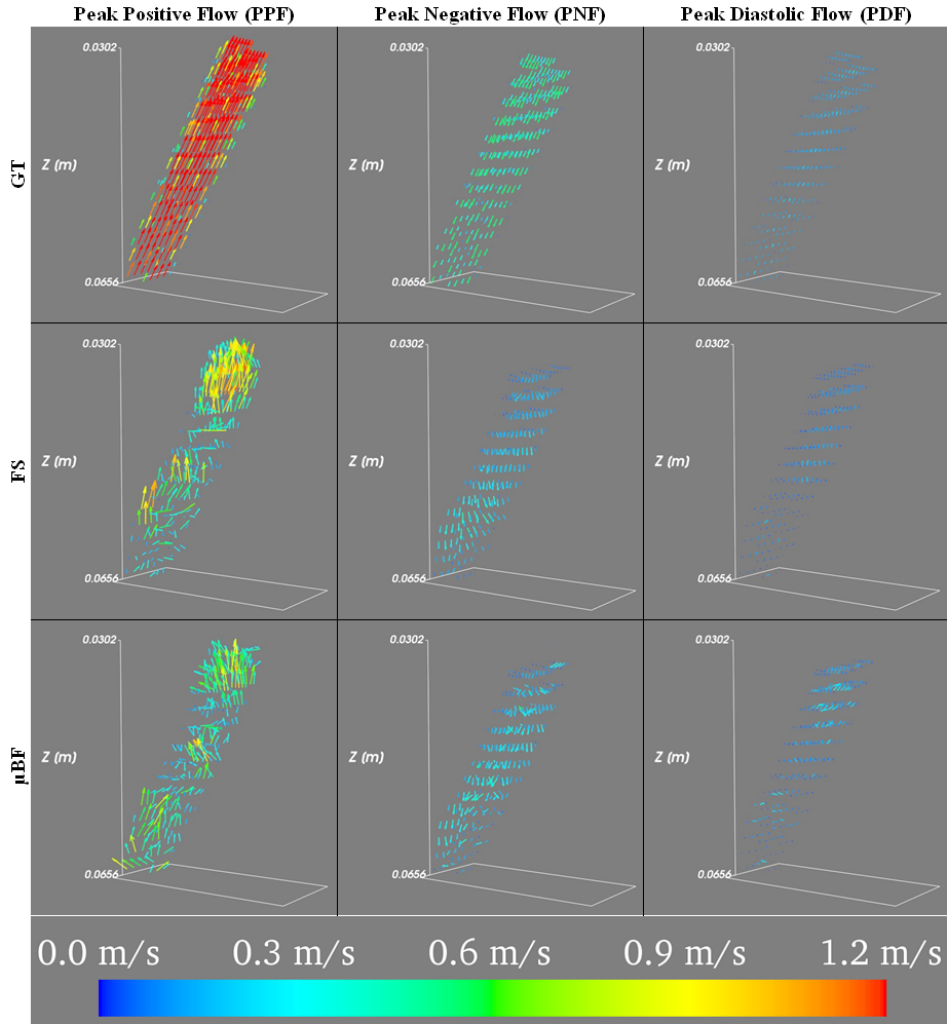

Figure 7.6: Ground truth velocity, FS and μBF transducer echoPIV estimate velocity fields at peak positive flow, peak negative flow, and peak diastolic flow stages of the cycle.

lated cardiac flow with a multiple-line acquisition protocol and also found similar results[136]. They found that velocity estimation was accurate in regions of slow-flow but degraded when fast-flow or high velocity gradients were present. Using cross-beam vector Doppler, Correia et al. (2016) reported, with an in-vitro experiment (4mm diameter tube, flow rate = 100-360 ml/min), that mean velocity estimation error increased (0.4% at 100 mL/min to 4.97% at 360 ml/min) with increasing velocities[133]. However, the ultrasound probe used in their study (Vermon, France) had double the aperture size (32×32 elements, pitch = 0.3 mm), thus providing superior spatial resolution. Their study also imaged to a maximal depth of 25mm with the vessel at 90°to the transducers axis. This

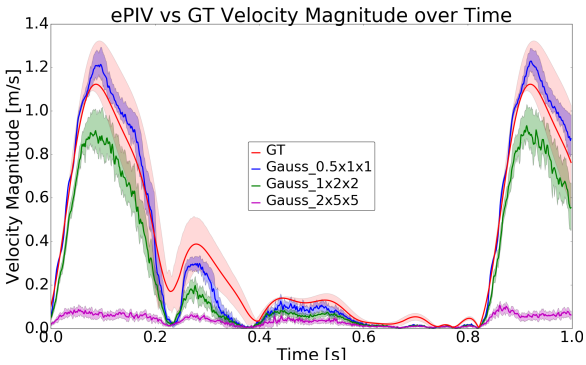

Figure 7.7: PIV analysis results on Gaussian kernel convolved versions of the same scatterers used for simulating the US volumes. By increasing the standard deviation of the Gaussian kernel an increasing PSF is simulated. Solid lines denote mean velocity magnitude, while shaded region denotes 25^{th} to 75^{th} percentile of the velocity magnitude. Gaussian kernel size (axial x azimuth x elevation) listed in increasing PSF size: blue = 0.5×1×1; green = 1×2×2; and magenta = 2×5×5; red = ground truth. Note how echoPIV underestimates the velocity magnitude more as the PSF size increases.

would provide greatest resolution (axial) in the same direction as the parabolic flow gradient, reducing velocity averaging.

Additionally, Pihl et al. (2014) simulated a 32×32 element matrix transducer with 0.3 mm pitch and used transverse oscillation to estimate the flow through a 6mm diameter tube at several different angles[134]. They did not record the large underestimations observed in this study, however, the flow phantom was centered at 30 mm depth. Additionally, they observed that estimation bias increased as the distance between sub-apertures was decreased; where at 9 elements (2.7mm) the bias was 15%. For reference the size of the transducer in this study is 5mm by 5mm.

In terms of image quality, the grating lobes observed in Figure 7.3.C are due to the μBF transducer being pre-steered with only 0°. However, for this study the grating lobes were outside the region of interest and did not influence the echoPIV results. Including more pre-steering angles is possible and will reduce the grating lobes. The reduced image quality of the μBF transducer did not result in reduced echoPIV performance, when compared to the FS transducer. This may change when the region of interest is expanded to include areas where grating lobes are prominent.

EchoPIV performance with this transducer may be better at shallower depths. These TEE transducers are designed for pediatric patients, where regions-of-interest (ROI) are both smaller and closer to the probe, allowing for imaging closer to the depth of best PSF (~20mm). Finally, echoPIV performance can potentially be improved by utilizing a multi-iterative, image deformation implementation, which has been shown to reduce the inherent zero-displacement bias present in matched kernel-size similarity estimates, as well as improve PIV accuracy in the flows with vorticity and shear[65]. Alternatively, elastic image registration[147] or non-rigid registration based optical flow[148] methods may perform better when speckle deformation is present.

8

TOMOGRAPHIC PIV IN A MODEL OF THE LEFT VENTRICLE: 3D FLOW PAST BIOLOGICAL AND MECHANICAL HEART VALVES

Based on:
Saaid H, **Voorneveld J**, Schinkel C, Westenberg JJM, Gijsen FJH, Segers P, Verdonck P, de Jong N, Bosch JG, Kenjeres S, Claessens T. Tomographic PIV in a Model of the Left Ventricle: 3D Flow Past Biological and Mechanical Heart Valves. Journal of Biomechanics; 2019; 90:40–49.[149].
Author Contribution: Phantom and experimental design; Involved in writing of manuscript.

ABSTRACT

Left ventricular flow is intrinsically complex, three-dimensional and unsteady. Its features are susceptible to cardiovascular pathology and treatment, in particular to surgical interventions involving the valves (mitral valve replacement). To improve our understanding of intra-ventricular fluid mechanics and the impact of various types of prosthetic valves thereon, we have developed a custom-designed versatile left ventricular phantom with anatomically realistic moving left ventricular membrane.

A biological, a tilting disc and a bileaflet valve (in two different orientations) were mounted in the mitral position and tested under the same settings. To investigate 3D flow within the phantom, a four-view tomographic particle image velocimetry setup has been implemented. The results compare side-by-side the evolution of the 3D flow topology, vortical structures and kinetic energy in the left ventricle domain during the cardiac cycle.

Except for the tilting disc valve, all tested prosthetic valves induced a crossed flow path, where the outflow crosses the inflow path, passing under the mitral valve. The biological valve shows a strong jet with a peak velocity about twice as high compared to all mechanical heart valves, which makes it easier to penetrate deeply into the cavity. Accordingly, the peak kinetic energy in the left ventricle in case of the biological valve is about four times higher than the mechanical heart valves.

We conclude that the tomographic particle imaging velocimetry setup provides a useful ground truth measurement of flow features and allows a comparison of the effects of different valve types on left ventricular flow patterns.

8.1. INTRODUCTION

The left ventricle (LV) is believed to preserve the momentum of the incoming blood flow during diastole by keeping it in motion during diastasis and smoothly redirecting it towards the outflow tract during systole [4], [150]. The topology of these flow structures is determined by the geometry of the LV cavity, the morphology of the mitral valve and the electrical conduction system [56], [151]. Various multidisciplinary studies have been conducted to better understand the patho-physiology of heart disease, to define clinically useful indicators of cardiac function [110], [152] and/or to understand the effect of mitral valve repair or replacement by a prosthetic device on the LV flow [153]. The choice of a biological vs. mechanical prosthesis for instance is still an open debate [154] as shown in a recent observational study by [155].

Particle image velocimetry (PIV) has been extensively used to study the effect of different prosthetic valves on the LV flow pattern [156]–[161]. A common limitation of these PIV studies is their 2D approach, yielding an incomplete view of the inherently three-dimensional (3D) flow structures in the LV and the inability to calculate all nine components of the velocity gradient tensor. There have been various attempts to overcome this limitation by reconstructing the 3D velocity vector field in the whole LV from velocity data obtained from separate measurement planes. The latter are either two-component velocity [162], [163] or three-component velocity data, obtained by the stereoscopic PIV technique [164], [165]. Both reconstructive methods take advantage of the periodicity of the cardiac cycle but require complex setups to translate or rotate the PIV system as well as time-consuming calibration and/or post processing procedures.

Tomographic PIV (tomoPIV) is considered the first "true" volumetric PIV technique [166]. In contrast to traditional planar PIV techniques, tomoPIV allows instantaneous extraction of all three velocity components over the entire volume of interest. To date, tomoPIV has been used for studying the blood flow in the aortic root [167], [168], the carotid artery [169] and the intracranial aneurysm [170].

Considering the above, the goal of the following work is twofold. First, we aim to demonstrate the feasibility of a tomographic, full-volumetric PIV technique to capture the 3D flow in a realistic and compliant LV model. Additionally, this phantom is compatible with 3D ultrasound and MRI imaging, such that 3D flow measurements acquired by these in-vivo medical imaging approaches can be compared to the optical ground truth in the future. Second, we compare the flow field generated by three structurally different prosthetic heart valves (biological, tilting disc and bileaflet) under the same running conditions.

8.2. METHODS

8.2.1. LEFT VENTRICULAR PHANTOM

MEMBRANE AND TANK

An optically transparent compliant silicone LV replica (0.5 mm thick) (Fig 8.1.b) was manufactured by painting four layers of silicone (HT 33 Transparent LT, Zhermack SpA, Rome, Italy) onto a 3D printed LV mould (Fig 8.1.a). The shape of the LV mould was extracted from the statistical mean of a dataset of segmented 4D computed tomography images of 150 patients [118], [119] (**Chapter 5**). The silicone has a refractive index of 1.413, measured by an Abbe refractometer (Bleeker, Zeist Holland).

The LV membrane was connected to the valve holders (Figure 8.1.c), and immersed (Figure 8.1.d) in a Plexiglas nine-sided polygon tank (Figure 8.2.a). The Plexiglas plates were machined and then glued together using a two-component reaction adhesive (Acrifix 192, Evonic Industries). Fig. 2a depicts the LV flow loop, which consists of a pressurized aortic chamber and an atrial chamber kept at atmospheric pressure. The outlet from the aortic chamber is connected to the left atrial chamber via an adjustable peripheral resistance valve (Vivitro Labs Inc., Victoria, BC, Canada) with a short length of silicone rubber hose.

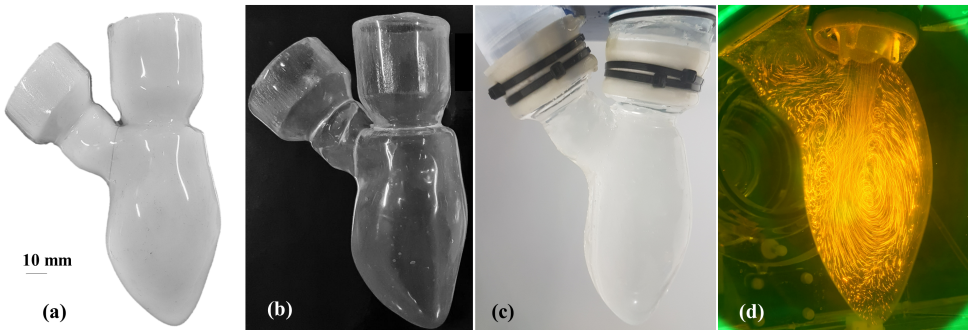

Figure 8.1: a) 3D-printed LV mould representing the endocardial shape at end systole, fitted with a mitral inflow and aortic outflow tract. b) LV silicone membrane. c) LV model attached to valve holders using cable ties. The outflow tract is tilted about 40° with respect to the mitral valve axis. d) A long exposure picture of fluorescent particles within the LV.

HYDRAULIC CIRCUIT

A pulsatile pump (Vivitro Labs Inc., BC, Canada) was used to mimic the pumping action of the LV. The hydraulic piston pump was connected to the acrylic tank (Figure 8.2.a - **9**) with semi-rigid tubing. The pump was velocity-controlled and set to generate a sinusoidal-like waveform with a frequency of 70 beats per minute and a duty cycle of 35%, resulting in a 300 ms systolic period and a stroke volume of 50 mL. Pressure transducers (6069, Utah Medical Products, Inc., Athlone, Ireland) were used to monitor the pressure in the aorta and inside the tank.

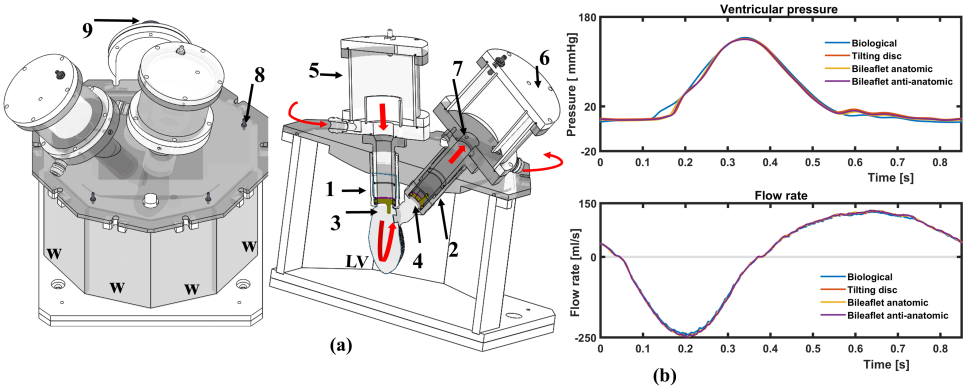

Figure 8.2: a) CAD view of the nine-sided tank. The shape of the tank provides undistorted optical access to the LV from different angles. **W** indicates the four windows used for optical access. The red arrows depict the LV flow loop. **1-2**: valve holders, **3-4**: mitral and aortic valve position, **5-6**: atrial and aortic blocks, **7**: aortic pressure catheter, **8**: multiple hose connectors for air removal and ventricular pressure monitoring, **9**: pump connector. b) Representative samples of ventricular pressure recorded during the PIV experiments and flow waveforms imposed at the pump.

WORKING FLUID & TRACER PARTICLES

A two-component working fluid was chosen to match the measured refractive index (1.4130) of the LV silicone membrane, thereby minimizing optical distortion. The ratio of the components in the fluid mixture (60% glycerol and 40% distilled water) was adjusted until its measured refractive index (1.4140) very closely matched that of the silicone. The dynamic viscosity and density of the working fluid were 14.0 mPa·s and 1160 kg/m^3, respectively. Fluorescent Rhodamine-B coated particles with a diameter of 20-50 μm and density of 1100 kg/m^{3}were used as tracers.

8.2.2. LASER & IMAGING SYSTEM

The imaging system consists of two high-speed cameras (Imager Pro HS 4M, PCO, Kelheim, Germany) set to record at 2000 fps. The setup was primarily designed to perform tomographic PIV from four different viewing angles using two cameras (Figure 8.2.a). For this purpose, a custom-made image splitter (consisting of 8 first surface mirrors) has been placed in front of each camera (Figure 8.2.a). Macro prime lenses with a focal length of 100 mm (Samyang Optics co Ltd., Korea) were used. A long-pass filter at 540 nm (Thorlabs, Inc., Newton, NJ, USA) was mounted in front of each lens to selectively capture the scattered fluorescent particle light. A volume of approximately 80×110×70 mm^{3}was illuminated by a double-cavity pulsed Nd:YLF laser (527 nm Litron Laser, England). Diverging lenses were used to shape the laser beam into a full-volume illumination.

CALIBRATION

A two-level calibration target was placed with a micrometre stage in nine positions equally spaced over 40 mm in the tank (without the LV membrane). To map the 3D space object

onto the 2D camera sensor plane, a third-order polynomial fitting method was applied. The geometrical calibration yielded an average error for all cameras and views of approximately 0.2 pixel. Subsequently, an ensemble of 200 particle images has been acquired to perform the iterative volume self-calibration procedure [171]. After four iterations, the volume self- calibration was able to reduce the disparity to less than 0.02 pixels for all cameras.

8.2.3. TOMOGRAPHIC ANALYSIS

All particle images were pre-processed to remove background intensity with a 7×7 sliding minimum kernel. Due to the Gaussian laser illumination shape, an intensity normalization filter was applied. Subsequent image processing involves 3×3 Gaussian smoothing, successive sharpening and manually masking out the non-flow regions. Following the suggested particle concentration from literature [172] a concentration of 0.04 particles per pixel was reached as an optimal measurement condition. The time separation Δt of 500 μs between image pairs was optimized to ensure that maximum particle displacement is about 6-10 pixels. All tomographic PIV data were processed with Davis 10 (LaVision, Göttingen, Germany).

8.2.4. MEASUREMENT PROTOCOL

The measurements were performed within the LV with three different heart valves mounted in the mitral position (Figure 8.4.a): a 25 mm tricuspid biological, a 24 mm tilting disc and a 25 mm bicarbon bileaflet valve which was mounted in two different orientations (anatomic and anti-anatomic). In all series a 19 mm Perimount Magna Ease (Edwards

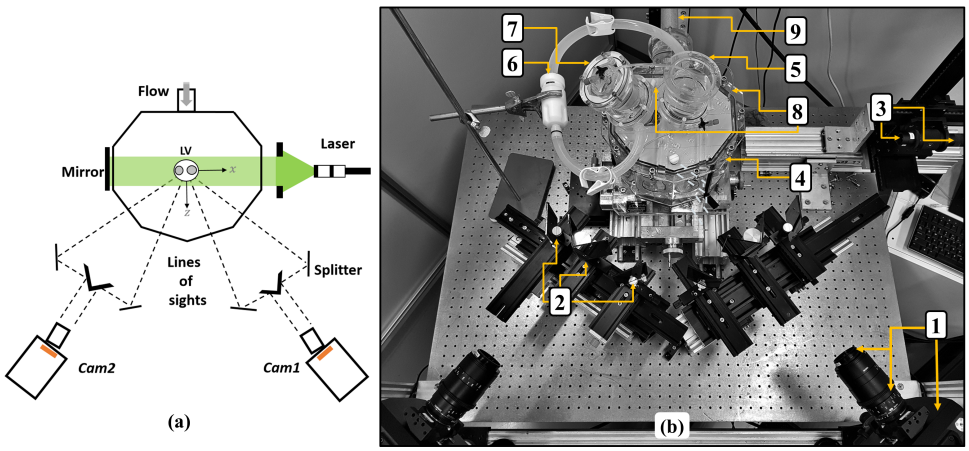

Figure 8.3: a) Schematic sketch (top view) of the tomoPIV setup. b) Picture of tomoPIV setup in linear configuration with two high-speed cameras equipped with prime lenses and filter [**1**], two mirror splitter system [**2**] and laser arm with telescopic head and optics compound [**3**]. The nine-sided tank [**4**], with atrial [**5**] and aortic blocks [**6**], connected with peripheral resistance [**7**]. Pressure transducer tubes [**8**]. The tank is connected to the pulsatile pump via a semi-flexible tube [**9**].

Lifesciences) tricuspid biological valve was used as an aortic valve. The particle images were reconstructed at 61 time points over the cardiac cycle (temporal resolution of 14 ms). The data from ten cardiac cycles were phase-averaged for each heart valve configuration.

Kinetic energy was calculated as:

$$KE = 0.5\rho \int_1^N \|\vec{v}\|^2 dV \qquad [J] \tag{8.1}$$

where ρ (density of fluid) was 1060kg/m^{3}and $\|\vec{v}\|$ is the velocity magnitude, dV is a voxel volume and N is the total number of voxels in the region of interest per frame.

8.3. RESULTS & DISCUSSION

In the following, the tomoPIV phase-averaged velocity data are presented. The first subsection illustrates the mean flow velocity field downstream of the four prosthetic valves. Further, we focus on the inflow characteristics by comparing the flow rate through transverse slices over time. In the last two subsections, we present the vortical structures and kinetic energy computed in the entire LV domain.

Figure 8.4.b compares the maximum inlet flow velocity between the four valves. The biological valve (BHV) opens slightly later than the mechanical valves (MHVs) and the transmitral flow velocity increases more rapidly for the BHV, reaching a peak value of up to 1 m/s - twice the magnitude of the MHVs. At the onset of the diastole, the tilting disc produces slightly higher velocities than the two bileaflet configurations. The two orientations of the bileaflet valve yielded virtually identical inlet velocities throughout diastole.

8.3.1. FLOW DYNAMICS

A note of caution is necessary, because of the large difference in the flow velocity range between the biological and mechanical valves (Figure 8.4.b), different colour scales were used for the iso-surfaces and velocity maps (Figure 8.5). Fig. 5 shows the mean flow topology of the tested heart valves (indicated with letters) at four characteristic phases (indicated with Roman numerals) during the cardiac cycle. The flow topology is represented by means of iso-surfaces based on the velocity magnitude and cross-sectional slices coloured with axial velocity.

Biological Valve: Initially, a strong transmitral jet is directed towards the anterior LV wall (time steps I-II). By the end of diastole (time step III), the inner core of the inflow starts disappearing (high velocity isosurface). Further, the inflow swirls towards the posterior wall, forming a counter-rotating flow pattern occupying the entire cavity. This flow feature is believed to prevent blood stasis by washing-out the apical region. The outgoing flow slides along the posterior wall and then crosses the inflow tract (time step IV). The crossed flow path shown here with the BHV (dashed line Figure 8.5) agrees with previous in vivo studies [53], [156], [173]–[175], where the flow passing the BHV was shown

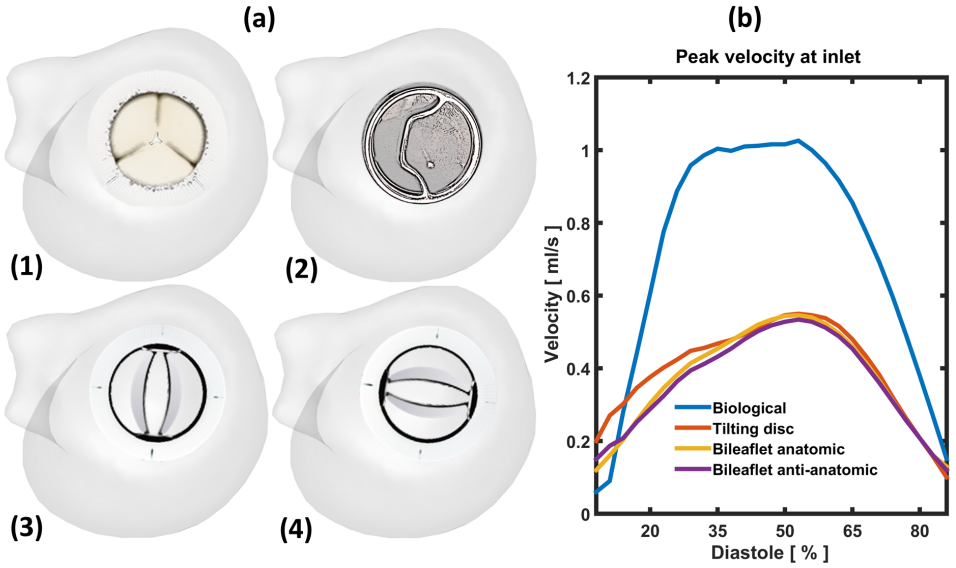

Figure 8.4: a) Snapshots of the LV model and heart valves in the mitral position: (**1**) biological Perimount 2900 (Edwards Lifesciences, Irvine, USA); (**2**) tilting disk (Björk-Shiley); (**3-4**) bileaflet (Sorin Biomedica, Saluggia, Italy) in anatomic and anti-anatomic orientation, respectively. b) peak velocity of the inflow jet during the diastolic phase.

to generate a strong jet towards the intraventricular septum and then to cross the inflow path (i.e. passing under the mitral valve) during systole (Figure 8.5.a).

Monoleaflet Valve: At the onset of the filling phase (time step I) a primary jet passes the main valve orifice. The primary jet advances along the posterior wall, while a secondary jet passes from the anterior valve orifice towards the anterior wall (time step II). At the end of diastole, the incoming flow forms a clockwise large-scale vortex (time step III) that is smoothly redirected towards the outflow tract. This looped flow path is in concordance with previous 2D-PIV investigations [160], [176], [177] (**Chapter 5**).

Bileaflet Valve: The two valve orientations exhibit minor differences in flow topology at the onset of the filling phase (Figure 8.5: c-d): in both cases the jet emanating from the outer orifices is significantly stronger than in the central orifice (time steps I-II). In the anatomic configuration (Figure 8.5.c), the jet on the anterior wall septum rolls off under the aortic valve, whereas due to the "Coandă effect" the opposite jet tends to realign with the central inflow jet (time steps II-III). In the anti-anatomic orientation (Figure 8.5.d), on the other hand, the flow pattern through the outer orifices appears to be nearly symmetric (time steps II-III). In both configurations, at mid diastole the strong central jet merges with the outer jets towards the apex. The iso-velocity surface emanating from the mitral valve dissipates before reaching the apex (Figure 8.5: c-d), as previously described in [156]. Additionally, our results indicate that in both configurations the bileaflet valve

gives rise to a crossed flow path. This confirms the findings from a prior in vivo study from [53]. Conversely, [175], using an ultrasound based vector flow mapping technique, showed that only the anti-anatomical orientation is associated with a crossed flow path. In our previous work [165], we even observed that both orientations lead to a looped flow path. Some of the discrepancies may be due to the highly simplified LV shape and the different LV diameter/valve ratio [165] or a limitation of two-dimensional echocardiography in case of [175]. Movie 1 (**Supplementary Video**) depicts the flow field throughout one cardiac cycle for each valve model.

8.3.2. INFLOW CHARACTERISTICS

For a more quantitative comparison between the BHV and the MHVs, the volume flow rate has been calculated through four cross-sections (Figure 8.6) over one cardiac cycle. As shown in Figure 8.6 (cross-section 1), the three mechanical valves open simultaneously. The two bileaflet orientations behave similarly in the first slices with a slightly higher flow rate than the biological and the tilting disc valves during the diastole. Moving towards the apex, in cross-sections 3 and 4, the penetration depth of the jet decreases drastically in the MHVs. In fact, the BHV exhibits a much higher downward flow over the filling phase compared to the bileaflet valve in anatomic configuration (cross-section 4). The stagnation phenomena in a LV have also been reported in a 2D-PIV investigation by Faludi *et al.* (2010) [53], showing that the jet entering the LV cavity collides more closely to the apex with a biological valve than with a bileaflet valve. Compared to the MHVs, the inflow jet through the BHV is more likely to reach and wash out the apical region. This potentially avoids stagnation zones and reduces the risk for thrombosis formation. In patients with dilated cardiomyopathy or myocardial infarction, where abnormal flow patterns are known to promote blood stasis between the apex and outflow tract [178]–[180], we would expect the BHV to perform better than the MHVs.

8.3.3. VORTICAL STRUCTURES

The lambda-2 (λ_2) method has been used to identify the 3D vortical flow features over the cardiac cycle [181]. In Figure 8.7, one can clearly see the formation of the vortex rings (time step I) and observe how they elongate, propagate and then dissipate during diastole. The strong inflow through the biological valve develops as a single vortex ring in the shear layer around the incoming jet (time steps I-II-III). The primary vortex ring is connected to a secondary vortex via branched tubes (trailing vortex tubes). The two vortices travel towards the mid-ventricle and start to break down in small structures before reaching the apex. The described vortex ring formation downstream the BHV is somewhat similar to the vortices generated from a cylinder with an inclined exit [182]. Comparable flow structures have also been described in previous LV fluid dynamic simulations [183]–[185] and in vivo studies [186].

The three MHVs exhibited different vortical flow features compared with the BHV. In case of the tilting disc, the flow through the posterior orifice yields a strong shear layer and interacted with the boundary layer along the lateral wall generating a curved vortex ring (Figure 8.7.b). The vortical structures then shed from the valve leaflets, progress

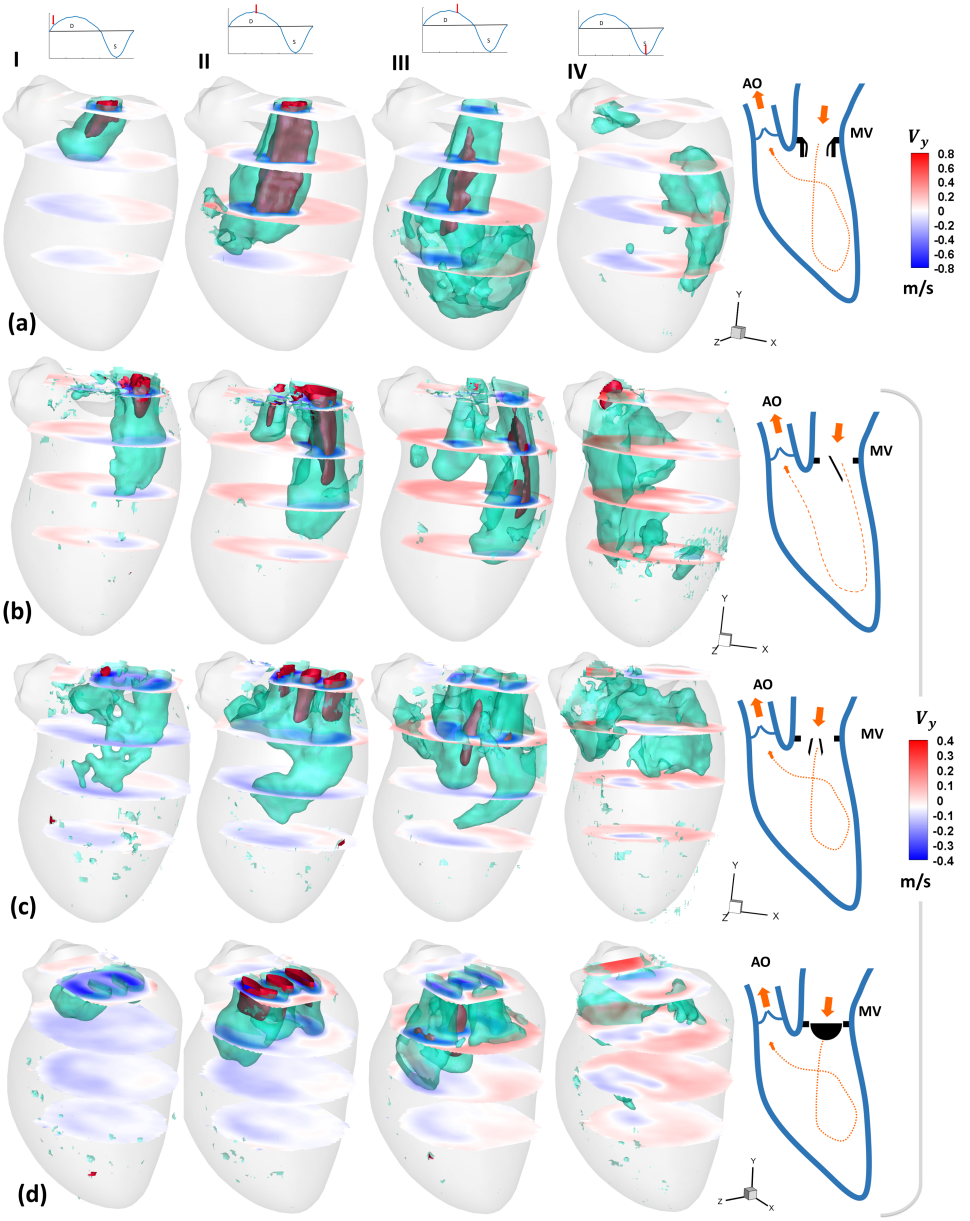

Figure 8.5: Time-sequence of the mean flow structures downstream of the mitral valves: **a**) biological, **b**) tilting disc, and bileaflet in **c**) anatomic and **d**) anti-anatomic orientation. Note that **d**) is slightly rotated about the y-axis to improve visibility of the flow structures. Two iso-velocity surfaces are shown for each valve (at 0.35 m/s and 0.75 m/s in case of the BHV and at 0.15 m/s and 0.35 m/s in case of the MHVs). Sketch on the right, shows the flow path (looped or crossed) with a dashed line. The cross-sections are colour-coded based on the axial velocity (v_y - long axis direction). Roman numerals indicate the time steps (I = 0.35s, II = 0.55s, III = 0.8s, IV = 0.2s).

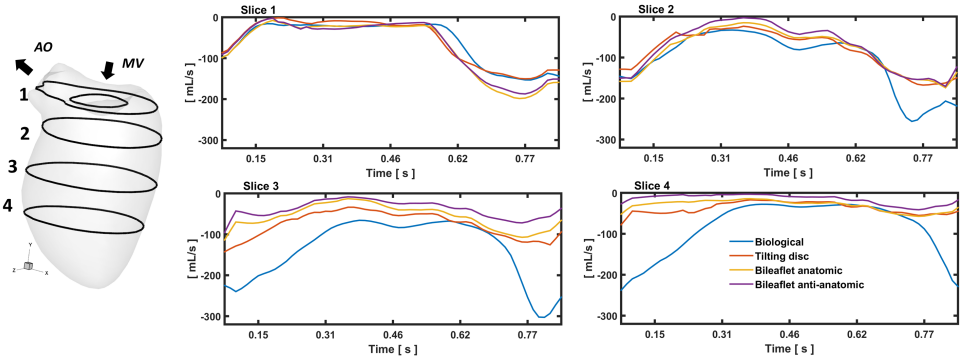

Figure 8.6: **Left**: Four equidistant (20 mm) cross-sections within the LV model. The first slice is positioned approximately 5 mm below the mitral valve. **Right**: Volume flow rate computed through four cross-sections for each valve. Only the downward flow was considered, i.e. positively signed velocities (v_y) were blanked. The MHVs open approximately at 0.54s whereas the biological open at 0.58s.

toward the mid regions, and finally dissipate by the end of the diastole due to viscous interaction with the ventricular wall.

Due to the leaflet geometry of the bileaflet valve, the inflow is spread over multiple orifices, rendering the formation of a single vortex impossible. Thus, the bileaflet valve induces incomplete vortex rings through the three orifices (Figure 8.7: c-d). At the onset of the filling phase, the flow is dominated by tubular structures generated from the outer orifices. Further into diastole (time step IV), a jet is formed from the central orifice with higher propagation velocity, forming a concentric coherent structure. The latter interact rapidly with each other and with the surrounding LV wall, disintegrating into smaller flow structures. Additionally, the so-called vortex ring was observed only downstream the biological valve with the formation of multiple vortex rings. The complete evolution of the vortical flow structures past the prosthetic heart valves over the cardiac cycle is provided as a supplementary video (**Movie 2**).

8.3.4. KINETIC ENERGY

The time course of integral kinetic energy (KE) computed for the entire LV domain is shown in Figure 8.8. The peak value of the kinetic energy passing the BHV is approximately four times higher than for the MHVs, as could be expected from the two-fold difference in the velocity magnitude profile during the cardiac cycle (Figure 8.4). A significant difference in terms of KE between BHV and bileaflet valve has been also reported in a recent numerical study by [187]. All mechanical valves exhibit a similarly shaped KE profile throughout the cardiac cycle. The tilting disc lead to higher KE levels during mid diastole and systole than did the bileaflet valve. In case of the bileaflet valve, the anatomic orientation yielded a slightly higher KE than the anti-anatomic configuration.

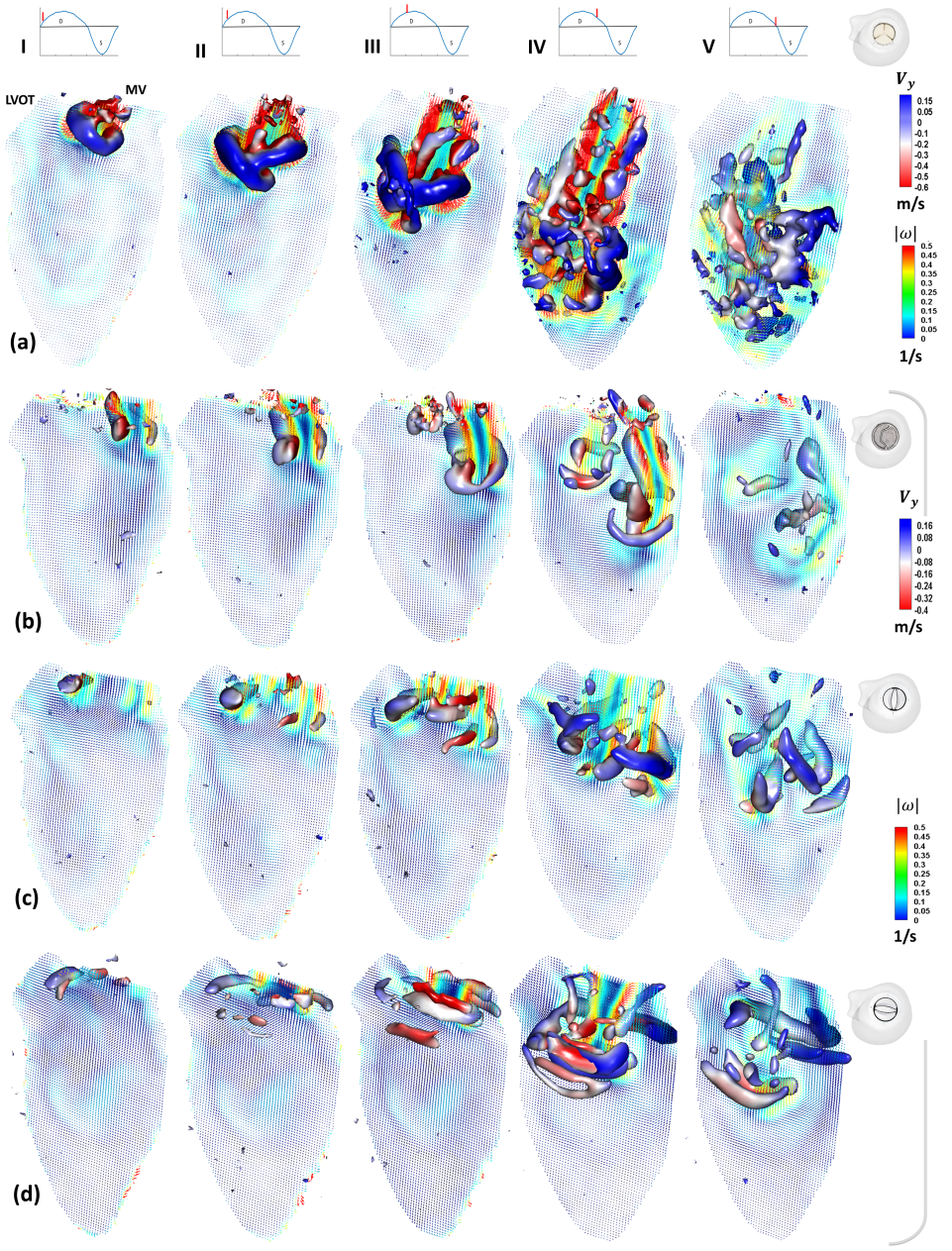

Figure 8.7: 3D vortical structures recognized by lambda-2 method are visualized as iso-surface (λ_2 = -0.015) and colour-coded with the axial velocity component. The 2D velocity vector field maps are coloured based on vorticity magnitude. **a**) Biological, **b**) tilting disc, and bileaflet in anatomic (**c**) and anti-anatomic (**d**) orientation. Roman numerals indicate the time steps (I=0.35s, II=0.45s, III=0.55s, IV=0.65s, V=0.85s).

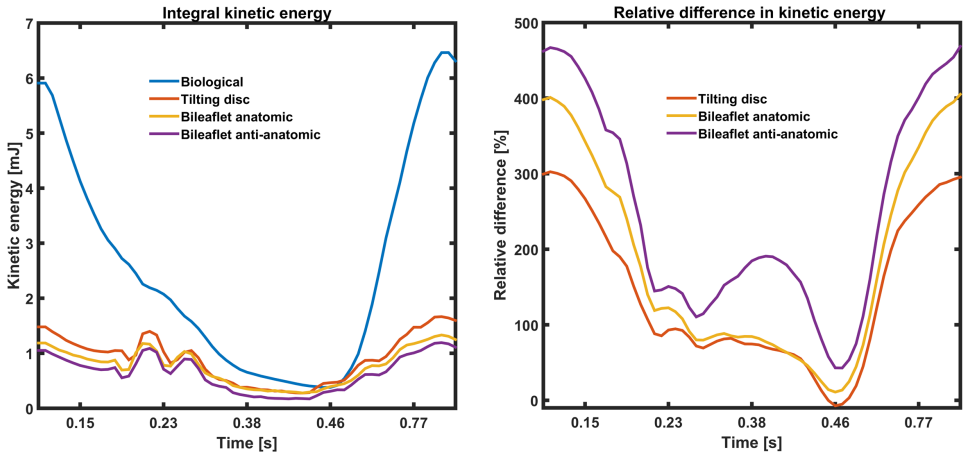

Figure 8.8: **Left**: the evolution of the kinetic energy within the LV domain, computed over the cardiac cycle. **Right**: The percentage difference of KE using the biological valve relative to each of the mechanical valves.

8.3.5. LIMITATIONS

Despite the aforementioned advantages of the employed technique, some limitations are worthwhile mentioning. TomoPIV hardware and software are generally more complex and expensive than 2D PIV or multiplane scanning setups. However, to reduce the cost of the PIV apparatus, a four-view tomoPIV imaging system has been implemented using a combination of only two cameras (instead of four) and a mirror system. Also, while tomoPIV does not require physical alignment between illumination and the calibration target, it is more sensitive to vibrations compared to stereoscopic PIV, which may lead to camera misalignment during the acquisition. To overcome this, we followed a well-established procedure for physical calibration, followed by the volume-self calibration. Due to computational cost and amount of data storage, we have presented only the averaged flow field data based on 10 cycles. A semi-quantitative convergence analysis (consisting of a comparison between the phase averaged data obtained from 10, 20 and 30 cycles) showed no discernible difference between 20 and 30 cycles. Only at peak early inflow a 7% difference in flow velocity was found between the results obtained with 10 cycles and the converged flow velocity data using 30 cycles. Moreover, we would like to mention that more advanced Lagrangian software algorithms, such as Shake-The-Box [188], may be more appropriate to analyse the time-resolved data in the future. Furthermore, the piston pump was driven by a sinusoidal-like wave form that does not represent diastasis and the late filling (A-wave). Consequently, it was not possible to investigate the interaction between the flow structures induced at the early filling and the fresh fluid entering during the late filling wave, as described in vivo [186] and in a recent numerical simulation study [177], using a similar LV geometry and a more realistic flow waveform. Also, the working fluid mixture has a dynamic viscosity four times higher than blood, which may have affected the flow resistance and consequently the formation and viscous dissipation rate of the vortical structures.

8.4. CONCLUSION

This work demonstrated the feasibility and usefulness of tomographic PIV, to study 3D flow dynamics in a compliant model. To the best of our knowledge, this study provides the first tomographic PIV study of the 3D flow pattern in a flexible left ventricular shape membrane, downstream of biological and mechanical valves.

We have analysed the effect of three types of prosthetic mitral heart valves on intraventricular flow under the same hydraulic conditions. The qualitative and quantitative flow analyses suggest that the biological valve generates flow patterns similar to those observed in vivo after a BHV valve replacement. Except for the tilting disc, all tested prosthetic valves induced a crossed flow path, where the outflow crosses the inflow path, passing under the mitral valve. Further, the inflow jet in the BHV penetrated deeper into the LV cavity compared to the MHVs. The λ_2 method for vortex identification showed the formation of multiple vortex rings in the presence of the BHV. The kinetic energy level associated with the BHV during diastole is approximately four times higher than the MHVs. Finally, we showed that the anatomic orientation of the bileaflet valve yields an overall slightly higher kinetic energy than the anti-anatomic configuration. Yet, none of our performed analyses reveal that one orientation of the bileaflet valve is to be preferred over the other.

ACKNOWLEDGEMENT

We acknowledge Michiel Manten and Geert Springeling of Erasmus Medical Center, for their assistance in fabricating the phantom. This work was supported in part by ZonMw within the Innovative Medical Devices Initiative (IMDI) program (project Heart Failure and 4D Flow).

9

4D echo-Particle Image Velocimetry in a left ventricular phantom

Submitted

ABSTRACT

Left ventricular (LV) blood flow is an inherently complex time-varying 3D phenomenon, where 2D quantification often ignores the effect of out-of-plane motion. In this study we describe high frame rate 4D echo-particle image velocimetry (echoPIV) using a prototype matrix transesophageal transducer and a dynamic LV phantom for testing the accuracy of echoPIV in the presence of complex flow patterns. Optical time-resolved tomographic PIV (tomoPIV) was used as a reference standard for comparison.

EchoPIV and tomoPIV agreed on the general profile of the LV flow patterns but echoPIV smoothed-out the smaller flow structures. EchoPIV also underestimated the flow rates at greater imaging depths, where the PIV kernel size and transducer point-spread-function were large relative to the velocity gradients. We demonstrate that 4D echoPIV could be performed in just four heart cycles, which would require only a short breath-hold, providing promising results. However, methods for resolving high velocity gradients in regions of poor spatial resolution are required before clinical translation.

9.1. INTRODUCTION

Left ventricular (LV) blood flow patterns are of increasing interest in the study and early diagnosis of LV dysfunction, with particular focus on the trans-mitral jet and its resulting intra-ventricular vortex dynamics [8], [15], [107], [108], [111], [189]. Currently, the primary *in vivo* techniques used for studying LV flow dynamics are phase-contrast magnetic resonance imaging (PC-MRI) and echocardiography.

PC-MRI has the advantage of being able to measure flow patterns in 3D (often called 4D-Flow MRI) and not requiring contrast agent injection, but requires long acquisition times (averaging over hundreds of cardiac cycles), expensive infrastructure and equipment and suffers low temporal resolution (only acquiring 20-30 phases per cardiac cycle) [190].

Alternatively, clinically available echocardiographic blood flow imaging techniques are bed-side and can be acquired at 15-100 frames per second; but are currently limited in the flow components that can be measured. Pulsed-wave Doppler can accurately measure blood velocities, but only the velocity component parallel to the ultrasound beam (axial) and in a small interrogation-region at a time. Alternatively, color Doppler can visualize blood flow over a region in 2D, but again only the axial velocity component. Also, aliasing is common when high velocities are present. As LV blood flow patterns are inherently 4D (time-varying 3D), echocardiographic techniques that can estimate 4D blood flow patterns, resolving all 3 spatial components, are required.

Some experimental ultrasound techniques have emerged to address the need for 4D blood flow measurement. For instance, vector Doppler, estimates the lateral velocity components by using multiple angled Doppler acquisitions [191]. Similarly, transverse oscillation estimates lateral displacement by introducing a lateral modulation into the received signal [192], [193]. However, transverse oscillation and vector Doppler require larger apertures for greater depths of interest, which is difficult with cardiac imaging due to the small inter-costal windows available.

Alternatively, Vector flow mapping calculates lateral velocity components from color Doppler acquisitions and segmentations of the LV wall using a model based approach [29], [194]. Gomez et al. (2015) demonstrated a 4D implementation of this technique in pediatric patients using multi-beat acquisitions of color Doppler and BMode imaging sequences[195]. Grønli et al. (2018) expanded this method to adults with the addition of a hybrid blood-speckle tracking and Doppler estimator to circumvent aliasing. Whether VFM over-simplifies complex *in vivo* flows remains to be tested [196].

Blood-speckle tracking estimates the displacement of blood-speckle patterns [35]. For the blood velocities expected in the LV (1 m/s, higher for regurgitation jets) very high frame rates are required to limit the inter-frame speckle displacement so that tracking is still possible. Wigen et al. (2018) demonstrated 3D blood speckle tracking in healthy adult volunteers, using multi-beat (7 heartbeats total) 3D volumes and multi-beat 10°wide 'thin-slice' acquisitions [197]. Both methods compared well with PC-MRI but mentioned signal-to-noise ratio (SNR) and clutter as significant challenges going forward. Here ultrasound contrast agents (UCA) microbubbles are useful as they provide large SNR improvements over native blood backscatter. The tracking of microbubbles

instead of native blood-speckle is called echo-particle image velocimetry (echoPIV).

Like speckle tracking, echoPIV also requires high-frame-rate (HFR) echocardiography to accurately track the high velocities present in the LV [43], [117], [136]. We have previously demonstrated that HFR echoPIV can accurately estimate the high velocities present in the LV *in vitro* (**Chapter 5**) and *in vivo* (**Chapter 6**) in 2D. Translation to 3D requires HFR 3D echocardiography.

In this study we assess the accuracy of 4D echoPIV using a prototype matrix transesophageal probe. The architecture of the probe permits volumetric imaging in a 20°× 20°field of view at the pulse repetition frequency (PRF, 4 kHz in this study). In order to image the whole LV (60°× 60°) a multi-beat acquisition scheme of just 4 cycles was used with 4 beams per cycle, allowing for a frame rate of 1 kHz. The presented technique would allow for 4D flow-pattern estimation over the whole LV in just 4 heart beats. The accuracy of HFR echoPIV using this acquisition scheme is assessed by comparison with time-resolved tomographic PIV (tomoPIV). TomoPIV provides high spatial and temporal resolution 4D velocity data in a single cycle but requires optical access. For this purpose we have designed a dynamic LV phantom that can be imaged with echoPIV, tomoPIV and (additionally) 4D-flow MRI.

9.2. METHODS

9.2.1. LEFT VENTRICULAR PHANTOM

A detailed explanation of the LV phantom used in this study is provided in **Chapter 8**, but a brief overview will be provided here. An optically and acoustically transparent silicone LV shell (~0.5 mm thick) was modelled on the mean shape of a set of 150 computed tomography patient LV segmentations [118], [119]. The LV was fitted with bio-prosthetic mitral (25 mm, Perimount, Edwards Lifesciences Corp., Irvine, CA, USA) and aortic (19 mm, Perimount Magna Ease, Edwards Lifesciences Corp.) valves and contained in a rigid acrylic pressure chamber with 9 faces to allow for optical access (excluding lid and base, see Figure 9.1.a). The mitral and aortic tracts of the LV were connected to atrial and compliance chambers, which were connected via a tube with an adjustable resistance valve (ViVitro Labs Inc., Victoria, BC, Canada), forming the LV flow circuit. The rigid pressure chamber was connected to a programmable piston pump (SuperPump, ViVitro Labs), forming the hydraulic circuit. The hydraulic circuit varied the volume in the rigid chamber, causing the ventricle to expand and contract, pumping fluid through the flow circuit. Both the hydraulic and LV flow circuit were filled with a glycerol in water mixture (60:40 by volume, density = 1160 kg/m^3, dynamic viscosity = 14.0 mPa·s, sound speed=1790 m/s) to match the refractive index of the silicone LV (1.413). The piston pump oscillated in a sinusoidal pattern (70 beats per minute, 50ml stroke volume) causing the LV to pump the fluid through the flow circuit (red arrows – Figure 9.1.a). The pump provided an electronic trigger signal for synchronizing acquisitions to a specific phase of the cycle.

9.2.2. TOMOGRAPHIC PARTICLE IMAGE VELOCIMETRY (TOMOPIV)

A brief overview of the tomographic particle image velocimetry (tomoPIV) setup is provided here, for a detailed description see **Chapter 8**. Two high-speed CMOS cameras

(Imager Pro HS 4M, PCO, Kelheim, Germany), recording at 2000 frames per second, were placed behind two sets of custom-built image mirror-splitter systems, to effectively create four independent views of the LV (Figure 9.1.b). The whole LV volume was then illuminated using a pulsed Nd:YLF laser (527 nm, Litron Laser, Warwickshire, England) passing through a diverging lens system (Figure 9.1.b) pulsing at 2 kHz (synchronized with the cameras). Fluorescent Rhodamine-B coated particles (diameter = 20-50 μm, density = 1100 kg/m3) were used as tracer particles and long-pass 540 nm filters (Thorlabs Inc., Newton, NJ, USA) were used to selectively capture the fluorescent signals from the particles. A single pump cycle was captured (857 ms) and processed with Davis 10 software (LaVision, Göttingen, Germany). An iterative window refinement scheme was used, starting with a kernel size of 7.843 mm3 for two iterations, reducing to 5.233 mm3 and finally 3.843 mm3, all with an overlap of 75%. The final spatial grid resolution was 0.963 mm^{3}and the temporal resolution was 0.5 ms. The measured point-spread-function of a single tracer particle was ~ 0.3 mm isotropic. Note that while in **Chapter 8** only 60 phases of the cycle were computed (to reduce computational demand of averaging 10 cycles), in this study all 2000 frames were computed for 1 cycle (time-resolved analysis with no phase averaging).

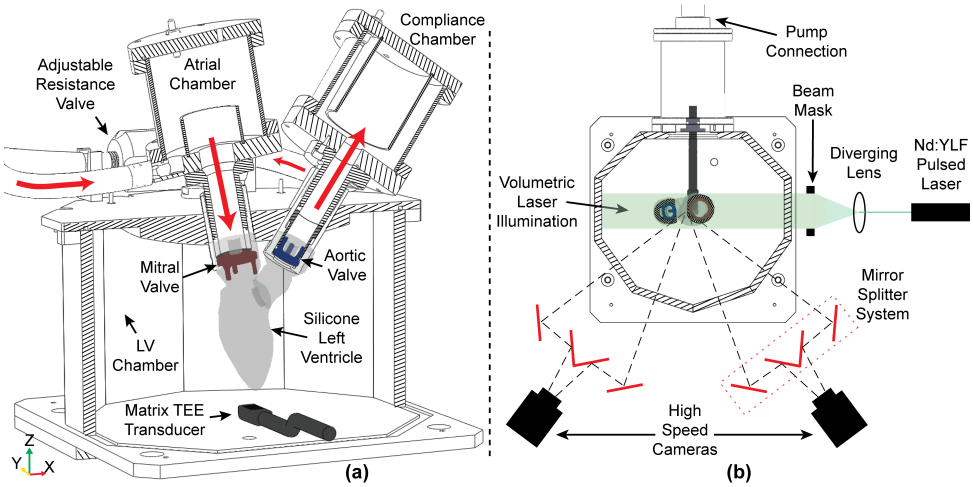

Figure 9.1: a) Partial section view of LV phantom with the matrix TEE transducer shown in its approximate location. Bio-prosthetic mitral (red) and aortic (blue) valves are shown in their position. Red arrows indicate direction of flow circuit. Atrial and compliance chambers are connected by a tube with an adjustable resistance valve. b) Schematic top view of LV phantom showing tomographic PIV setup, see text for details.

9.2.3. ULTRASOUND

A prototype matrix transesophageal (TEE) probe (Oldelft, Delft, the Netherlands) was used for imaging (central frequency 5 MHz). It had separated transmit (128 elements, 5.76 × 0.9 mm^2) and receive (2048 elements, 8.7 × 8.7 mm^2) apertures of piezoelectric elements mounted on top of a front-end application-specific integrated circuit (ASIC). The receive aperture is grouped into 128 groups of 4×4 elements, where micro-beamforming

is performed on the ASIC for each group, thereby reducing the channel count to 128 in receive (Figure 9.2.a). A detailed explanation of the probe is provided in [198]. The reduced channel count allowed for the probe to be used with a single Vantage 256 ultrasound system (Verasonics Inc., Kirkland, WA, USA). The probe was positioned below the ventricle, typical of an apical view. The probe was placed approximately 5 mm below and 10 mm septal of the ventricle's apex.

The maximum beam width that could be used (preventing grating lobes in receive) was 20°× 20°, however this was not sufficient for imaging the full LV volume (Figure 9.2.b). Thus, in order to cover the whole LV (60°× 60°), a rectangular grid of four beam steering angles was used in both the elevational and azimuthal directions (-20°, -5°, 5°and 20°) resulting in 4×4 = 16 beam angles (Figure 9.3). PRF was limited to 4 kHz - to prevent reflection artifacts from the LV chamber lid occurring at higher PRFs (despite the use of acoustic dampening material on the inside of the lid). Consequently, the use of 16 sequential beams would have resulted in a frame rate of 250 Hz which was not sufficient for high-velocity particle tracking. Therefore, we used a gated sequence of 4 beams per pump cycle over 4 cycles to adequately sample the spatial field of view required, while maintaining a frame rate of 1 kHz (see Figure 9.3). Note that this gated sequence is not suited for B-mode imaging of the bubbles as their position is not cyclical. However, for velocity mapping this scheme is acceptable in the case that flow patterns are repeated each cycle and that cycle periods are consistent, so that the motion of the bubbles is cyclical. In the case of this experiment these assumptions were reasonable.

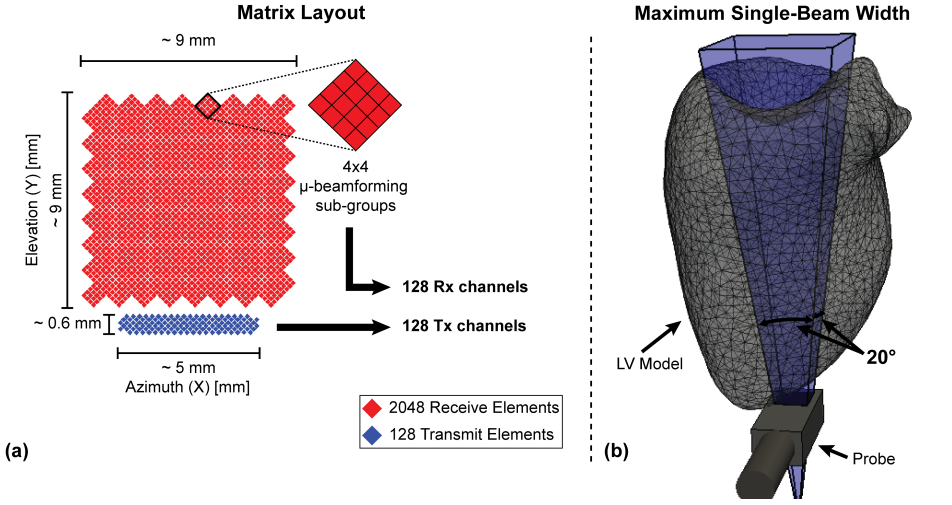

Figure 9.2: a) Schematic layout of matrix elements, note the separated transmit (Tx) and receive (Rx) apertures. The channel requirements in receive are reduced from 2048 to 128 by micro-beamforming in local 4×4 sub-arrays. b) The probe architecture imposes a maximum single-beam opening angle of 20°x 20°in receive. This is insufficient to image the entire LV, thus multiple steered-beams are required to image the required field of view.

It was our intention to use diluted ultrasound contrast agent as ultrasound tracer particles. However, the operation of the phantom setup spontaneously generated small

air bubbles in the flow circuit with sizes expected to be between 10 and 100 μm which already provided an acceptable concentration of tracer particles. Therefore, no ultrasound contrast agent was added.

A diverging wave transmission was performed using a 3-cycle, 5 MHz tone-burst with a PRF of 4 kHz. Peak-negative pressure was measured to be between 260 kPa at 20 mm depth from the probe to 60 kPa at 80 mm depth. Details of the transmit and receive scheme are provided in Table 9.1.

Table 9.1: Ultrasound Parameters

Transmit	
Center Frequency	5 MHz
Pulse Repetition Frequency	4 kHz
Virtual Focus Depth	-21 mm
Apodization	Rectangular
Receive	
Field of View (per beam)	120 mm × 20°× 20°
Field of View (total)	120 mm × 60°× 60°
Apodization	Rectangular
Sample Spacing	180 μm × 0.6°× 0.6°
Number of Gated Cycles	4
Frame Rate (per cycle)	1 kHz

9.2.4. BEAMFORMING & ECHOPIV

Acquired RF data were first clutter filtered (see Table 9.2) and then beamformed using Verasonics software (v3.0.10) in Cartesian coordinate space and envelope detected before inverse-scan conversion to spherical coordinate space. The conversion to spherical space was performed to keep the point-spread-function consistent over depth. Custom PIV software written in Python (v3.6) was used to perform PIV analysis (see Table 9.2) between successive acquisitions with the same beam angle.

Ensemble averaging of 5 successive correlation volumes (correlation averaging) was used, producing a vector frame rate of 200 Hz. An iterative window deformation algorithm was used where the second image volume was iteratively deformed using the previous iterations displacement estimates as a deformation field [26]. Before echoPIV analysis the tomoPIV data were used to derive a static mask of the LV. For each beam this mask defined where displacement estimation should be performed. After displacements had been estimated for all 16 beams they were combined, averaging overlapping vectors where applicable.

Vector data were then scan converted onto a regular Cartesian grid, using the grid spacing at 50 mm depth as the cross-beam grid spacing. Finally, local-median outlier removal and replacement was performed and vectors were regularized on the Cartesian grid using separate temporal and spatial Gaussian convolution filters.

9.2.5. VISUALIZATION & COMPARISON

Vector Comparison: Vector data were visualized and flow rates computed using Paraview (v5.6, [199]). Before comparison the tomoPIV data was down-sampled to match the grid spacing of the echoPIV data using a local mean both spatially and temporally. Flow rate through three XY planes (25 mm, 50 mm and 75 mm deep from the probe) as well as a plane intersecting the outflow tract were computed and compared for both echoPIV and tomoPIV. The average velocity magnitude in a 4 mm section in center of the jet (at the same plane depths as the flow calculations) was computed too.

Signal-to-Noise Ratio (SNR): To estimate the noise reference signal, a no-transmit acquisition was recorded with all other transmit parameters held constant. The SNR could then be calculated using the formula:

$$SNR = 20 \cdot \log_{10}\left(\frac{I_{transmit}}{I_{notransmit}}\right) \tag{9.1}$$

where $I_{transmit}$ and $I_{notransmit}$ are the average signal amplitudes for recordings with transmit on and off, respectively.

Point-Spread-Function (PSF): PSF was measured at different depths by measuring the full-width-half-maximum envelope signals of isolated bubbles along the three Cartesian axes.

Cycle	Azimuthal Steering (X)	Elevational Steering (Y)
1	-20°, -5°	-20°, -5°
2	5°, 20°	-20°, -5°
3	-20°, -5°	5°, 20°
4	5°, 20°	5°, 20°

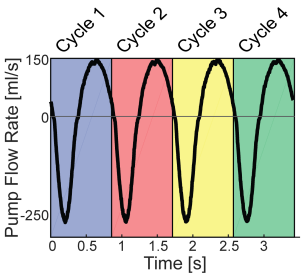

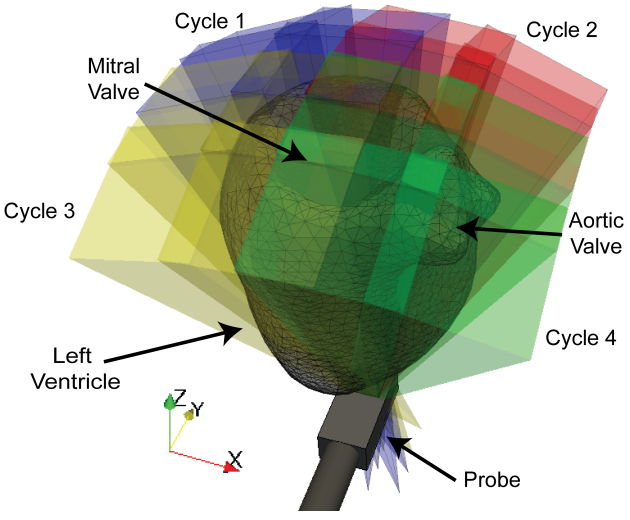

Figure 9.3: Spatial sampling of the full LV volume is gated over 4 pump cycles, with 4 different beams being acquired successively each cycle (16 total). Thus, a region of 60°× 60°can be sampled while maintaining a frame rate of 1 kHz, but requiring 4 cycles to acquire.

Table 9.2: EchoPIV Parameters

EchoPIV	
Clutter Filter	55 Hz High Pass 8^{th} order Butterworth
Similarity Measure	Normalized cross-correlation (FFT)
Kernel Size	6 mm × 5°× 5°
Iterations	4
Window Deformation	Bi-cubic Interpolation
Overlap	50% × 75% × 75%
Particles	10-100 μm Air-bubbles
Final Grid (Spherical)	3 mm × 1.25°$times$ 1.25°
Final Grid (Cartesian)	3 mm × 1.4 mm $times$ 1.4 mm
Correlation Averages	5 frames (5 ms)
Vector Frame Rate	200 Hz
Subpixel Estimator	3x1D Gaussian Peak Fit
Regularization	
Outlier Detection	Universal Outlier Detector [121]
Gaussian Temporal Moving Average	Standard Dev. (σ) = 5 ms, Truncation = 3σ
Gaussian Spatial Smoothing	σ = 1.6 × 0.9 × 0.9 mm^3, σ = Truncation = 1.6 σ

9.3. RESULTS

9.3.1. DESCRIPTION OF FLOW FIELD

Shortly after mitral valve opening, a high-velocity jet forms which is angled towards the septal LV wall (Figure 9.4:b and j). Initially a vortex ring develops at the head of the jet but the septal side of the ring is diminished when it collides with the septal wall (Figure 9.4.d). From this moment the posterior side of the vortex ring expands, redirecting flow along the posterior-inferior side of the LV towards the base (Figure 9.4:d and l). Once the mitral valve closes the fluid swirls in a general clockwise manner along both the Azimuthal and Elevational (X and Y) axis, with many smaller vortices appearing along the jet's primary flow path (Figure 9.4:f and n). Once the aortic valve opens, flow travels upwards along the posterior-inferior wall of the LV and up along the base, passing under the mitral valve, before exiting the LV through the outflow tract in a helical pattern (with higher velocities at the top of the outflow tract than at the bottom - Figure 9.4.h).

9.3.2. QUALITATIVE COMPARISON

During the initial stages of filling, when the jet is beginning to form, echoPIV grossly underestimates the velocity and volume of the jet (Figure 9.4:a vs b and Figure 9.4: i vs j). Once the jet has progressed deeper into the LV (closer to the probe) echoPIV estimates similar velocity magnitudes to tomoPIV but still estimates the jet to be thinner in volume (Figure 9.4:c vs d and Figure 9.4:k vs l). Also, during this phase, echoPIV and tomoPIV observe similar shapes and positions of the vortex rings, but the magnitudes are larger in

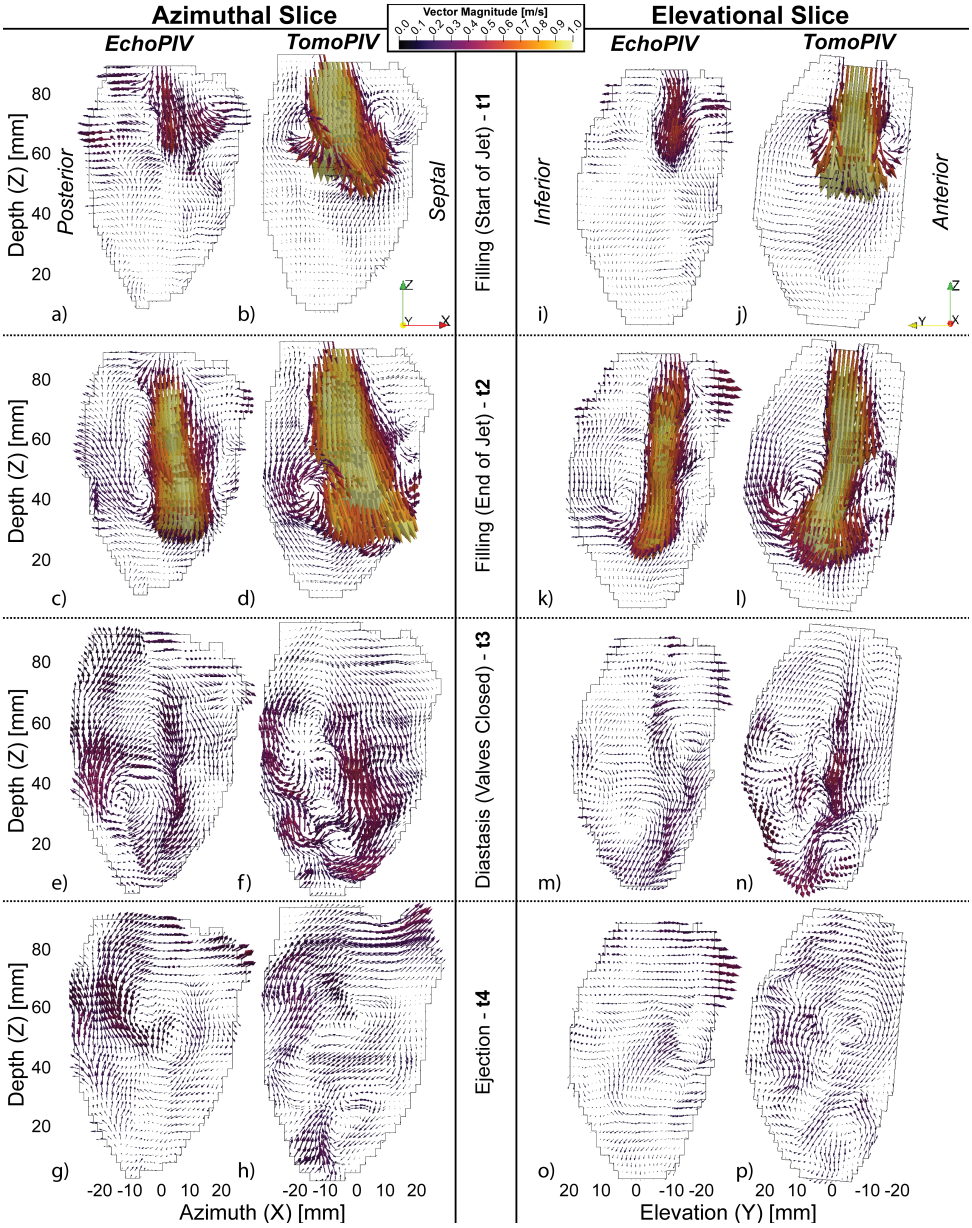

Figure 9.4: a-h) Azimuthal and (i-p) elevational slices through the center of the mitral valve at different phases of the pump cycle ($t_1 - t_4$, see Figure 9.5.b). See text for details. Supplementary video available (**online**).

tomoPIV. During diastasis, echoPIV and tomoPIV agree in the general swirling of the flow but a more detailed (winding) flow pattern is observed in the tomoPIV (Figure 9.4:e vs f and Figure 9.4:m vs n). During ejection, echoPIV observes similar flow to the tomoPIV, moving up the posterior wall turning to travel along the base, but no ejection is detected in the region of the outflow tract.

9.3.3. QUANTITATIVE COMPARISON

VOLUME FLOW RATE

In order to quantitatively assess the accuracy of echoPIV we calculated the flow rate through various planes (Figure 9.5.a), including: flow through the aortic outflow tract (Figure 9.5.c); filling flow rates (only flow with negative Z velocity components) calculated through horizontal (XY) planes at depths of 25 mm (Figure 9.5.d), 50 mm (Figure 9.5.e) and 75 mm (Figure 9.5.f) from the probe.

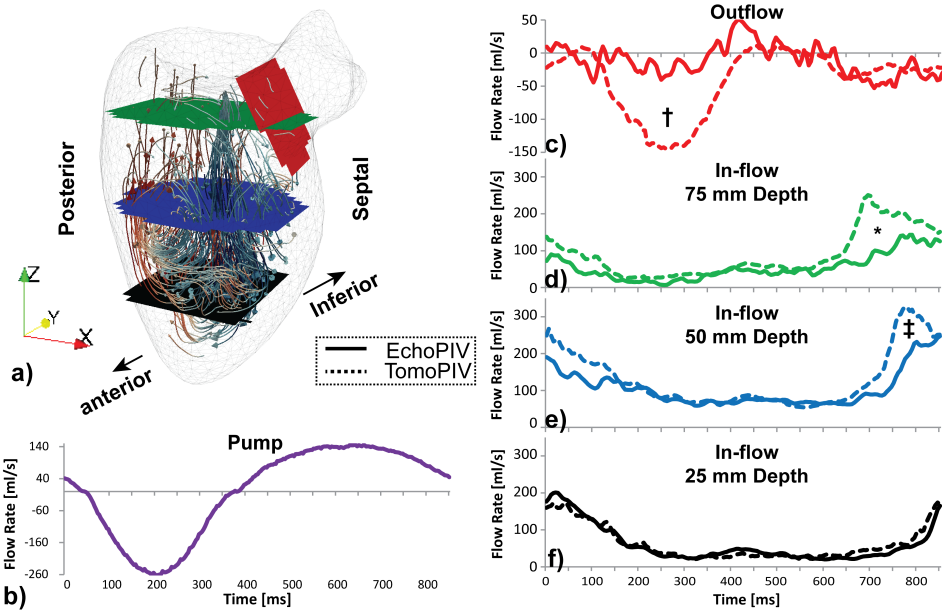

Figure 9.5: a) 3D path-line visualization of tomoPIV data at ~ t_2, with colored slices corresponding to the through-plane flow rate curves shown in c-f). b) Pump flow rate curve with t_1 to t_4 indicating the time points shown in Figure 9.4.c) Flow rate comparison through the outflow tract and (d-f) through horizontal planes at 75 mm (c), 50 mm (d) and 25 mm (e) depth from the transducer, limited to flow moving in the –Z direction only (inflow). Symbols ⋆, † and ‡ refer to notable flow differences discussed in the text.

EchoPIV severely underestimates the flow rate through the outflow tract during ejection (Figure 9.5.c - †), with a maximum flow rate of 54 ml/s compared with 145 ml/s for tomoPIV. An increase in flow through the plane is detected compared to the rest of the cycle, but the magnitude is severely underestimated.

During filling, a large underestimation is also observed at the 75mm depth plane

(Figure 9.5.d - ⋆) with a difference in maxima of 94 ml/s at the time of jet formation, and a mean underestimation of 34 ml/s over the whole cycle. For the 50mm depth plane the underestimation of peak flow rate reduces to 75 ml/s (Figure 9.5.e - ‡), with a mean underestimation of 31 ml/s over the whole cycle. In the 25 mm plane, echoPIV overestimates the peak velocity by 21 ml/s with a mean difference of 4 ml/s less than tomoPIV over the whole cycle (Figure 9.5.f).

VELOCITY MAGNITUDE

Velocity magnitudes at the same depths as depicted in Figure 9.5.a are shown in Figure 9.6 (average velocity in a 4 mm diameter sphere in the center of the jet). Similarly, we see that echoPIV underestimated the high velocities more in the planes further away from the probe. At 75 mm depth the RMSE of echoPIV's velocity magnitude was 18 cm/s (17%). This underestimation reduced to 12 cm/s (12%) at 50mm depth and 8 cm/s (12%) at 25 mm depth. RMS error for outflow was 15 cm/s (40%).

Velocity profiles, measured at the 75 mm plane (Figure 9.5.a – green), during jet formation and after the jet had fully formed (t_1 and t_2, Figure 9.6.b) are shown in Figure 9.7. Note that echoPIV highly underestimated the velocity profile during the early stages of filling (t_1, Figure 9.7:a & b); but correctly measured the profile a short time later (t_2, Figure 9.7:c & d). Although, while the velocity magnitude was correctly measured at t_2, the width of the profile is still underestimated.

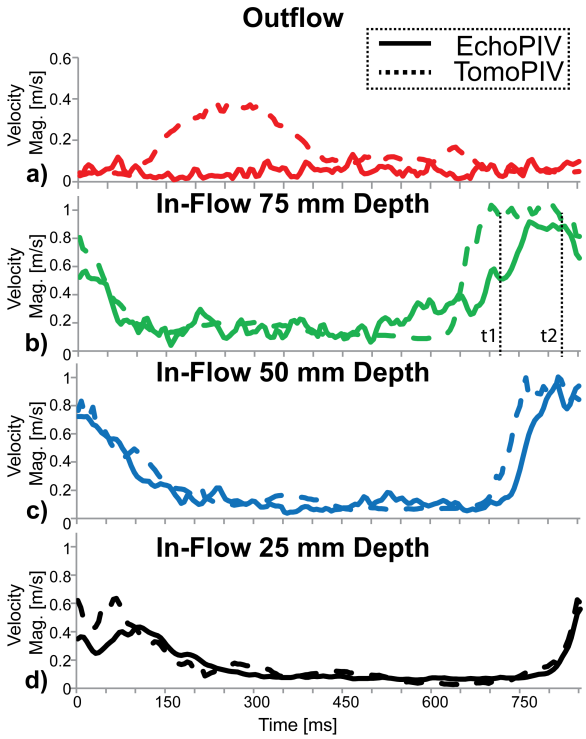

Figure 9.6: Velocity magnitude comparison through a 4 mm diameter sphere in the center of the jet at different depths (the same depths as indicated in Figure 9.5.a). Solid / dashed lines represent the average velocity magnitude for echoPIV and tomoPIV. Note that echoPIV underestimates velocities more at farther distances from the probe. Time points t_1 and t_2 shown again for clarity, see Figure 9.7 for velocity profiles these times.

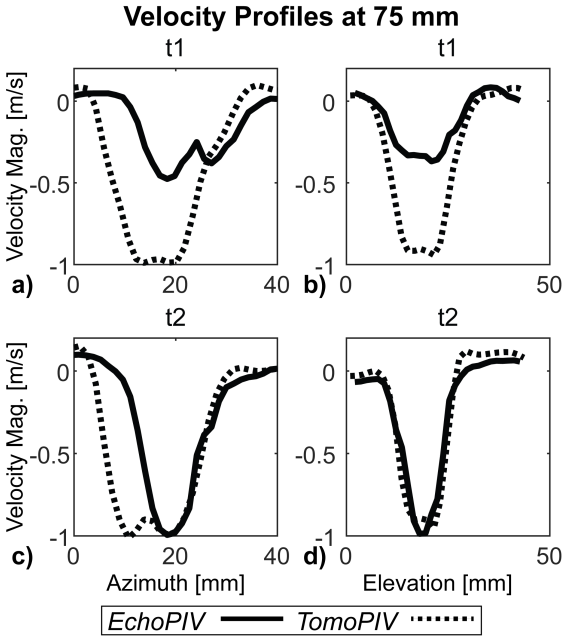

Figure 9.7: Instantaneous velocity profiles, through the 75 mm plane (see Figure 9.5.a), at time points t_1 (top row: a, b - jet formation) and t_2 (bottom row: c, d - jet formed, see Figure 9.6.b) along azimuthal (left column: a, c) and elevational (right column: b, d) axes. Note that echoPIV underestimates the peak velocity profile magnitude at t_1 but not at t_2.

SNR & PSF

Calculated SNR and PSF values are shown in Table 9.3. Between 25 mm and 75 mm depth SNR decreased by 10 dB and the lateral PSF (X and Y) increased 4-fold. The PSF measured from the reconstructed tomoPIV volumes was 0.3 mm isotropic.

Table 9.3: SNR & PSF over Depth

Depth	**SNR**	**PSF [mm]**		
[mm]	**[dB]**	X	Y	Z
25	27	1.1	1.0	0.6
50	22	2.0	2.2	0.7
75	17	3.5	4.1	0.7

9.4. DISCUSSION

Flow structures imitating the trans-mitral filling jet were produced by the LV phantom and measured in 4D by both tomoPIV and echoPIV at high temporal resolution (1 kHz for imaging, 200 Hz for velocity vectors – due to correlation averaging of 5 frames). Both techniques agreed on the general flow patterns observed, but echoPIV underestimated the velocity magnitudes and flow rates in the deeper regions, i.e. close to the mitral and aortic valves.

The two modalities agreed on the development of the central vortex on the poste-

rior/inferior side of the LV. The part of the vortex ring on the septal and anterior side of the LV was less defined in echoPIV than tomoPIV. This could be due to the lateral width of the vortex on the septal/anterior side, where the lower lateral resolution of echoPIV was not able to resolve the flow gradients.

9.4.1. UNDERESTIMATION IN JET

EchoPIV estimated the trans-mitral jet to be of similar shape and follow the same path as tomoPIV. However, echoPIV largely underestimated the volume flow rate and velocity magnitudes of the jet at the start of filling (Figure 9.4.a versus b, and i versus j). The echoPIV estimate was more accurate closer to the probe (Figure 9.4.c versus d, k versus l), but the width of the jet was still estimated to be thinner than with tomoPIV. Note that echoPIV was able to measure similar velocity magnitudes as tomoPIV (Figure 9.7:c & d) but estimated a thinner profile spatially and a delayed temporal response.

The increasing flow rate underestimation with distance from the probe suggests that the PSF, kernel size, SNR and/or clutter are responsible, as discussed further below.

PSF & KERNEL SIZE:

The kernel size used (6 mm × 5°× 5°) corresponds to approximately 6 × 6.5 × 6.5 mm^3at a distance of 75 mm from the probe, which is large relative to the final tomoPIV kernel size (3.843 mm^3). The jet diameter was roughly 15 mm, and the relatively large lateral kernel size of 6.5 mm may cause averaging of the jet edges with the surrounding slow flow regions, resulting in underestimation of the jet profile that we see in Figure 9.7.c). Note that the kernel size could not be reduced further as the lateral PSF width at that depth was ~ 4 mm after scan-conversion. In our experience, reducing the kernel size to smaller than the PSF has led to a large increase in erroneous vectors. Note that echoPIV's lateral PSF was ~13 times larger than tomoPIV's at 75 mm distance from the probe.

Wigen et al. (2018), using their 3D hybrid autocorrelation / blood-speckle tracking estimator, reported an increasing underestimation of faster lateral velocities, but not for fast axial velocities, which were calculated using a de-aliased autocorrelation estimator [197]. Whether the different trend in results compared to ours is caused by their larger probe aperture or by the different tracking techniques requires further studies.

A similar interaction between velocity gradient and spatial resolution was found almost 30 years ago, where Foster et al. (1990) found (using pulsed wave Doppler) that longer range-gates caused more velocity magnitude underestimation than shorter range-gates, in flow profiles with steep velocity gradients [200].

SNR:

In the case of SNR, we calculated that SNR decreased by 10 dB from 25 mm to 75 mm (Table 3). A study by Ekroll et al. (2018) showed that reducing SNR caused increased lateral bias in 2D speckle tracking[201]. However the bias in this work was primarily axial, whereas Ekroll et al. only showed appreciable increases in axial bias at 0 dB SNR. Thus, we do not expect that SNR is the primary source of underestimation seen in the trans-mitral jet. However, SNR may play a significant role in the underestimation seen during ejection, where displacement is primarily lateral.

CLUTTER:

Holbek et al. (2017), when using 3D transverse oscillation, observed a similar underestimation in flow rate and even an overestimation of peak-velocity magnitude compared with PC-MRI[192]. They attributed the flow rate underestimation to underestimation of the velocities close to the vessel wall, where the clutter filter removed the moving blood signal. This caused 'leakage' of low velocities into the blood flow profile, reducing the overall flow rate.

While not necessarily related to clutter in our case, the same 'leakage' effect is believed to play a role in the jet. We believe that in regions with high velocity gradients, the average of the velocities present in the resolution cell are estimated.

9.4.2. GATED ACQUISITION SEQUENCE

The proposed acquisition sequence of 4 gated cycles of 4 beams per cycle allowed for a frame rate of 1 kHz while still scanning a field-of-view of 60°× 60°. The goal, of course, for echoPIV is for fully time-resolved 4D velocity estimation in a single heart-beat. However, this work serves as an intermediate step; where the requirement for multiple beams was mandated by the probe architecture as a maximum beam-width of 20°× 20°was possible without experiencing grating lobes in receive. The PRF was limited to 4 kHz to avoid reflection artifacts from the phantom lid, which appeared in the middle of the LV at higher PRF (> 5 kHz PRF should have been possible at 120 mm depth). A higher PRF would have permitted more beams per cycle, while keeping the frame rate constant; thereby reducing the number of gated cycles required for imaging the required field of view. Another method to reduce the number of gated cycles would be to reduce the number of elements grouped together for channel reduction; as this would effectively reduce the pitch in receive so a wider beam could be formed without grating lobes.

9.4.3. FLOW PATTERNS

The flow patterns generated by the LV phantom share some key aspects with physiological LV flows. For example, the high velocity trans-mitral jet with its accompanying vortex ring structure (Figure 9.4:b & j), and the dominant central vortex structure (Figure 9.4:d & l) which redirects the jet upwards towards the base of the LV. Note that flow is not split into an early and late filling phase, as is the case physiologically. This is because the piston-pump moved in a sinusoidal pattern (Figure 9.5.b). Interpretation of the physiological consequences of flow patterns observed in this study should take this temporal profile into consideration. Additionally, the LV shell does not include trabecular structures, nor does it contract and relax with a twisting action that is observed in the human LV [202]. However, the purpose of this phantom was to create reproducible flow patterns on a scale like those observed *in vivo*, with less simplistic flow patterns than other common validation phantoms, such as straight tube (laminar flow experiments) [203], [204] or the spinning disk phantom [32], [197], [203]. This was accomplished in a setup which can be imaged optically, acoustically and by magnetic resonance imaging.

9.4.4. LIMITATIONS & FUTURE PERSPECTIVES

The probe used in this experiment was a TEE probe, but the imaging angle chosen is an apical transthoracic view. If a more typical TEE view were used the distance to the mitral valve area would be reduced to less than 70 mm, by viewing the LV parallel to its long axis. This shorter imaging depth would allow for a higher PRF. On the other hand, viewing the LV perpendicular to its long axis would mandate a larger lateral field of view, possibly requiring more gated acquisitions to fully sample the LV spatially.

Improving lateral resolution is expected to reduce the spatial smoothing of the jet velocity profile and allow for smaller flow structures to be resolved. Increasing aperture size is difficult for TEE probes due to power dissipation and spatial constraints. However, transthoracic probes have slightly more manageable power dissipation constraints, but the aperture still has to fit between the ribs ~ 15-20 mm.

SNR at depth can be improved by transmitting at a lower frequency; however this will result in significantly lower lateral resolution. Using pulse inversion and second harmonic filtering may help, by transmitting at 2-3 MHz and receiving at 4-6 MHz, thereby increasing penetration depth and reducing tissue clutter simultaneously.

In this study we used air-bubbles as a contrast medium; *in vivo* ultrasound contrast agent microbubbles would be used instead. Air-bubbles were used as they already appeared spontaneously in the phantom's operation, and earlier iterations of the experiment indicated that addition of microbubbles did not improve the tracking result over the spontaneous air-bubbles.

In order to reduce spurious vector results we used a correlation ensemble of 5 frames. Increasing the correlation ensemble length will further improve SNR in the case of low velocity gradients, but will be susceptible to correlation peak broadening in the presence of high velocity gradients. Our choice to ensemble average 5 frames reduced the vector frame rate to 200 fps; however this could also be performed using a moving-average, so that the frame rate could have been preserved at 1000 fps (at the cost of computational time).

Finally, the proposed LV phantom is also MRI compatible. Future work will assess 4D flow MRI accuracy against tomoPIV, facilitating comparison between 4D echoPIV with 4D flow MRI.

9.5. CONCLUSION

We have demonstrated, *in vitro*, that 4D echoPIV of the whole LV can be performed in just four heart cycles. The general flow patterns compared well with tomoPIV, an optical technique with far superior spatial resolution. Significant underestimations in flow rates were observed in the basal region of the LV, close to the mitral and aortic valve, which were located furthest from the probe. The reason for underestimation is suspected to be due to spatial smoothing where point-spread-function is large relative to the spatial velocity gradients.

ACKNOWLEDGEMENT

We would like to thank Franc van den Adel (Oldelft Ultrasound) for his work in designing and building the matrix probe. We acknowledge Henry den Bok (Delft University of Technology) for technical assistance with the probe setup. We also thank Geert Springeling, Michiel Manten and Robert Beurskens (Erasmus MC) for fabricating the LV phantom.

This work was supported in part by ZonMw within the Innovative Medical Devices Initiative (IMDI) program (project Heart Failure and 4D Flow)

10

DISCUSSION

10.1. KEY FINDINGS OF THIS THESIS

10.1.1. TWO-DIMENSIONAL WORK

Over the course of this thesis we have developed and tested high-frame-rate (HFR) echo-particle image velocimetry (echoPIV) in a variety of different flow conditions. We started with a simple laminar pipe-flow experiment (**Chapter 2**), finding that microbubbles provided improved tracking accuracy over blood mimicking fluid at greater depths. We then validated HFR echoPIV *in vivo*, in healthy volunteers (**Chapter 4**), where we found good agreement between HFR echoPIV and phase contrast magnetic resonance imaging (PC-MRI), even for the high velocity systolic flows. Additionally, in our *in vivo* experiments, we found that we needed to apply very low acoustic pressures to prevent bubble destruction when using HFR imaging. We also found that singular value decomposition-based (SVD) clutter-filtering provided better ultrasound contrast agent detection than amplitude modulation *in vivo* (**Chapter 3**).

For assessing left ventricular (LV) flow, we developed a dynamic LV phantom, so we could compare HFR echoPIV with time-resolved optical PIV - a gold standard velocimetry technique in fluid dynamics research (**Chapter 5**). Using the LV phantom, we found that HFR echoPIV could accurately measure the high velocity flow patterns associated with diastolic flow. We also found that using coherent compounding in the presence of fast moving scatterers caused strong underestimation of fast flows. By instead using correlation compounding between angular acquisitions, the fast flows could be measured. We then demonstrated that HFR echoPIV could also measure the high velocity diastolic flow patterns *in vivo*, in a patient (**Chapter 6**).

10.1.2. THREE-DIMENSIONAL WORK

We expanded HFR echoPIV to 3D, first in a simulated pipe-flow phantom with a Womersley blood flow profile (**Chapter 7**). A simulated pediatric transesophageal (TEE) matrix

transducer using micro-beamforming and an ideal, fully sampled matrix of the same size were used to scan the phantom at HFR. We found that the low lateral resolution of the small aperture transducers resulted in strong underestimation of high velocity flows. Moving forward, we designed a new LV phantom, capable of 3D optical imaging using tomographic PIV. First, we used tomographic PIV to study the 3D flow fields resulting from different mitral valve prostheses (**Chapter 8**). Then we used the tomographic PIV results as a ground truth for assessing the accuracy of 4D echoPIV using an adult matrix TEE transducer (**Chapter 9**), with quadruple the aperture-area of the pediatric transducer simulated previously. We showed that we could image a 60°by 60°by 100 mm region of interest at a frame rate of 1000 frames per second using only 4 gated heart cycles.

HFR echoPIV in 2D and 3D will be discussed separately in this chapter, due to their different stages of maturity.

10.2. 2D HIGH FRAME RATE ECHOPIV

This thesis shows that 2D HFR echoPIV can measure the high velocity blood flow patterns that are associated with systole in the abdominal aorta (AA) and both systole and diastole in the LV. This section will discuss the potential benefits of 2D HFR echoPIV as well as some foreseeable challenges to its clinical translation.

10.2.1. BENIFITS OF HFR ECHOPIV FOR CLINICAL USE

Doppler flow measurement techniques are common practice clinically. Also, echoPIV studies using conventional line-scanning echocardiography are numerous. What new information does HFR echoPIV bring to the table?

Pulse wave Doppler can measure the full range of velocities present in the trans-mitral jet. However, this information is only available in a small region of interest and only the axial component of the velocity is estimated - severely limiting the number of fluid dynamics parameters that can be estimated. Alternatively, echoPIV can be performed on standard B-mode image sequences obtained with clinical scanners using commercially available software (e.g. HyperFlow, AMID, Italy) [9], [47], [50], [51], [54], [56]. This allows for full time-resolved velocity fields to be estimated, but the draw-back is that high velocities are severely underestimated [42]–[44], [117]. This is where HFR echoPIV fits in: now both the high velocity magnitudes and the flow patterns can be captured in a single set of acquisitions, allowing for fluid dynamics-based parameters to be more accurately calculated.

Quantitative fluid dynamics properties such as vorticity (and its derivatives), local pressure gradients, kinetic energy and kinetic energy dissipation are sensitive to the velocity magnitude. By accurately measuring the velocity magnitudes it is expected that these existing parameters can become more sensitive to changes in LV function. The use of HFR also allows for 'slowing down' complex transient 2D flow patterns, such as the formation of the trans-mitral jet and its accompanying vortex ring in the LV, or reverse-flow in the abdominal aorta - potentially revealing new facets of blood flow dynamics in the cardiovascular system.

10.2.2. CHALLENGES IN CLINICAL TRANSLATION

The move from experimental studies to using HFR echoPIV in clinical practice still requires addressing some technical and practical challenges.

IMAGE QUALITY

In **Chapters 3 & 4** we assessed the feasibility of HFR echoPIV in the abdominal aortas of healthy volunteers. Feasibility was very good in these volunteers; however they had very low body-mass indices and good image quality. In patients image quality is expected to be worse, with more attenuation and phase aberration from higher levels of fatty tissue. Additionally, in patients with significant arterial stenosis, it is not uncommon for large calcified lesions to be present around the artery. These calcifications can cause signal loss ("shadowing") inside the blood pool, making bubble tracking difficult to impossible. Angled acquisitions may help to some extent, where different views of the blood pool may be acquired, allowing for intelligent selection of only the uncorrupted signal.

In cardiac imaging, specular reflection from the ribs and lungs can cause increased clutter signal [129] and even complete shadowing of entire regions of the LV. Additionally, the use of diverging waves makes clutter from the valves and tissue more prominent than with focused beams, due to the stronger side-lobes. Fortunately the use of HFR imaging permits new ways of filtering clutter from bubble signals, such as singular value decomposition [62] and adaptive clutter filters [205].

REAL-TIME FEEDBACK

During this study HFR sequences were captured and stored for offline beamforming and processing. Thus limited real-time feedback of data fidelity was available to the sonographer, limiting feasibility. Processing of the received data can be split into three steps: 1) B-mode formation, 2) clutter-filtering and 3) vector processing. The highest priority of these steps for live view imaging is B-mode formation. For our *in vivo* imaging studies (**Chapters 3, 4 & 6**), we used a separate clinical scanner to find the anatomical region we were interested in and then a local quality line-scanning live view on the Verasonics to find the same landmarks as seen on the clinical scanner. However, it was not always easy to find the same landmarks as found on the clinical scanner. In some cases, even once the landmarks had been found, the subjects' breathing motion resulted in deviations from the intended view, in the worst cases leading to complete image loss (from rib shadowing).

Fortunately, a good live view image quality should be possible with pulse-inversion and diverging wave imaging sequences. We, as well as Toulemonde et al. (2018a [206]; 2018b [131]), have found that performing ensemble averaging of the HFR contrast image sequences provided very good image quality (of the microbubbles), even surpassing that of conventional line scanning contrast imaging modes. Real-time imaging with ensemble-averaged diverging wave sequences should be possible, because many of the operations can be performed before beamforming (such as pulse inversion and ensemble averaging), reducing the computational requirements to what is already possible on existing hardware. On clutter-filtering, while we found that singular value decomposition (SVD) based clutter filtering outperformed amplitude modulation in the abdominal

aorta (**Chapter 3**); SVD required much longer processing times than amplitude modulation. However, SVD has been implemented previously for real-time blood flow imaging in a pigeon brain [207], and accelerated versions of the SVD algorithm also exist [208], indicating that real-time SVD filtering may be possible as well.

Real-time processing of echoPIV to obtain live-view vector overlays is probably less feasible than real-time B-mode imaging. However, a low spatial resolution live-view may be possible by limiting processing to only a few interrogation areas and only a single iteration step. High fidelity processing can then be done offline, as is common with many analysis software packages (e.g. TomTec Arena, TomTec Imaging Systems GmbH, Germany).

PARAMETER TUNING

EchoPIV is based on optical PIV, which was primarily used in research environments by trained experts in PIV processing. This means that many parameters usually need to be fine-tuned for optimal results. For use in the clinic, many of these parameter choices should be automated, such as kernel size selection, degree of overlap, and regularization method. However, given the ease of use of commercial echoPIV software such as HyperFlow, this should be possible too.

NEED FOR ULTRASOUND CONTRAST AGENT

The need for ultrasound contrast agent limits the use of echoPIV as an early stage screening tool for heart and arterial diseases. Other vector flow imaging techniques, such as vector flow mapping, speckle tracking, vector Doppler and transverse oscillation do not need contrast agent injection. However, the use of ultrasound contrast agent microbubbles has some distinct advantages, such as increased SNR and control over the degree of sparsity in the image set. Perhaps patients who are not suitable for vector flow imaging via non-contrast methods can be recommended for echoPIV analysis instead, forming an intermediate step between routine examinations (non-contrast echocardiography) and needing an MRI scan. This is common in stress echocardiography today, where patients with poor LV wall opacification are often recommended for ultrasound contrast agent administration to maximize diagnostic potential [209].

The distinct line drawn between different flow measurement techniques is also not necessary, where combinations thereof could be beneficial. For instance, using vector flow mapping as a regularization step for echoPIV analysis, or using transverse oscillation to obtain a 'second opinion' on lateral estimates.

10.2.3. FUTURE PERSPECTIVES FOR CLINICAL STUDY

While HFR echoPIV has been demonstrated in this thesis, there is still much more work to be done. First, the demonstration of HFR echoPIV in the LV of a single patient (**Chapter 6**) should be expanded to more patients (this is on-going research at the time of writing this thesis). The intraventricular flow patterns of healthy volunteers should be re-evaluated using HFR echoPIV. Healthy hearts have been examined with conventional line-scanning echoPIV [46], [47], [53], but re-examination of healthy LV dynamics at the frame rates permitted by HFR echoPIV is required for future comparison in patients.

Stress echocardiography is well established for diagnosis of coronary heart disease, but is increasingly used for a wider variety of diagnostic functions [210]. HFR echoPIV may reveal differences in compensation to increased cardiac output between healthy and dysfunctional ventricles, by studying the adaption of their intraventricular flow patterns to increased demand.

The presented implementation of echoPIV in this thesis always used a static fluid boundary (mask). Automatic segmentation of the LV (or vessel) wall would be beneficial for ensuring that tracking of blood and tissue is not confused. The boundary motion can also be used to help in regularization of the vector data [117], [196]. In the case of the abdominal aorta, a dynamic segmentation of the arterial wall can also assist in calculation of wall-shear stress.

10.2.4. TECHNICAL DEVELOPMENT

FRAME-RATE

In **Chapter 2**, we acquired data at 5000 frames per second (fps). However, we found that using echoPIV at 5000 fps caused larger bias than at 1000 fps for slower flows (~0.25 m/s: unpublished - NVMU spring meeting presentation 2016). We believe that this was due to errors in subpixel peak finding that are known (from optical PIV) to be dependent on the degree of subpixel shift [211]. By increasing the lag of the cross-correlation (skipping frames), the subpixel shift can be extended, allowing more accurate tracking of slower velocity flows. In this case the high velocity flows (~1 m/s) were still trackable at 1000 fps.

However, in LVs with valvular regurgitation/stenosis or in vessels with stenosis, jets are known to form with very high velocities (severe stenosis classified as more than 4 m/s [212]). In these cases, higher frame rates would be necessary to capture the jet velocities, but that would reduce the accuracy of tracking for lower velocities (due to the relatively low sub-pixel displacement between frames). In this case a method of dynamically changing the lag for different regions of the image may help to improve the dynamic range of HFR echoPIV.

Alternatively, more advanced subpixel estimators can be used, where simple 2x1D (or 3x1D in 3D) Gaussian fitting was used in this thesis. Azar et al. (2010) found that 2D (or 3D) polynomial fitting reduced subpixel estimation error compared with multiple 1D polynomial fits by an order of magnitude[213]. Oversampling of the image data and/or correlation function can also be used to increase subpixel accuracy, however this incurs significant computational costs [214].

COHERENT COMPOUNDING

Coherent compounding of multiple angles has been used extensively in microvascular flow quantification studies for improving image resolution and contrast [77], [95], [215]. However, when a relatively high degree of motion is present between angled acquisitions speckle artifacts and signal loss occur [96], [206]. Some methods have been proposed to compensate for the motion between angles, and thereby restore image quality [96], [216]–[220]. In this thesis we instead perform compounding in the correlation

domain (Correlation compounding), where instead of assuming zero displacement between frames, we assume negligible acceleration. It should be noted that a similar idea was presented (at roughly the same time) named 'incoherent ensemble correlation' by Leow and Tang (2018) [97].

However, when imaging deep regions of interest with phased array transducers the use of angles may not be beneficial anymore, due to the limited aperture and large imaging depth (small angle differences start to look very similar). In the case of LV imaging, with depths of up to 15 cm and apertures of less than 20 mm, the use of angled transmissions may not be worth the loss of frame rate.

RESOLUTION

In Chapters 7 and 9 we observed that high frame rate alone is insufficient for measuring flow profiles with steep spatial (and temporal) gradients. In **Chapter 7** we show that resolution has a significant impact on the bias of echoPIV estimates. In **Chapter 9** we see that the depth dependent lateral resolution of diverging wave imaging can lead to significant bias at greater depths (~70 mm in **Chapter 2**). Therefore, improving lateral resolution is an important focus point for future work.

Increasing the transducer aperture or transmit frequency are theoretically the easiest ways to improve lateral resolution. However, aperture in 2D echocardiography is limited by the spacing between the ribs, and in 3D by the number of connections required and increased power dissipation for large matrix transducers. Increases in transmit frequency imply increases in attenuation (which is counter-productive to imaging deep structures) and can result in reduced microbubble signal levels as the frequency deviates from the microbubbles' resonant frequencies. Alternatively, we can use different beamforming strategies that harness the sparsity and coherence of microbubble imaging. Examples of such beamformers are minimum variance beamforming [221] or short-lag spatial coherence beamforming [222]. While these advanced beamformers usually incur high processing costs, there are real-time implementations [223] that may be feasible for beamforming thousands of frames. Whether these beamformers are suitable for high velocity flow tracking remains to be seen, but is worth exploration.

The echoPIV implementations (2D and 3D) did not make use of the axial phase information when performing cross-correlation, only the envelope of the beamformed signals was used. Using the RF data may improve tracking results, as has been shown in tissue strain imaging [224].

TISSUE/CLUTTER SUPPRESSION

Even with the use of ultrasound contrast agent microbubbles, clutter is still a problem in blood flow tracking with echoPIV. The reader will notice that singular value decomposition (SVD) based clutter filtering was used in the pipe-flow phantom (**Chapter 2**) and the abdominal aorta (**Chapters 3 & 4**); whereas a frequency based high-pass filter was used in the LV studies (**Chapters 5, 6 & 9**). We found that SVD worked well in the abdominal aorta but did not experience the same success in the LV, where valve motion would cause 'flash' artifacts. The reason and solution for these flash artifacts is ongoing research.

Adaptive clutter filters were not used in this thesis but are worth exploring in future [205], [225], [226].

MICROBUBBLES

In **Chapter 3** we attempted to find an optimal microbubble concentration and acoustic pressure to use for HFR imaging. Our work on microbubble concentration was for the most part inconclusive, where we found that higher concentrations provided higher signal levels and better tracking correlation during diastole, but slightly lower tracking correlation during systole. We expected that lower concentrations would improve tracking in the presence of strong velocity gradients, but perhaps the velocity gradients in the abdominal aorta were not strong enough to see a significant difference. Future work in the LV is planned to assess the effect of microbubble concentration on tracking performance.

Regarding acoustic pressure, we found that we needed to apply very low pressures (mechanical index < 0.03) to prevent bubble destruction during systole. During diastole bubble destruction still occurred, due to the extended exposure time. In the LV finding an optimal acoustic pressure is more difficult due to the wide range of depths being interrogated (approximately 20 mm to 120 mm). Thus, a good pressure at 120 mm would likely cause severe bubble destruction at 20 mm. This is still ongoing research.

In this thesis SonoVue® (Bracco S.p.A., Italy) was used exclusively as tracer particles for echoPIV. It is possible that other contrast agents would be more resilient or better suited to extended periods of plane / diverging wave excitation. For example, monodisperse microbubbles have been shown to have much higher scattering coefficients (when driven at resonance frequency) than standard poly-disperse microbubbles, potentially improving SNR at low transmit pressures [227].

10.3. 3D HIGH FRAME RATE ECHOPIV

In this thesis we demonstrated echoPIV on two different TEE transducers: a small pediatric matrix transducer (**Chapter 7**) and an adult matrix transducer (**Chapter 9**). For the pediatric transducer, a diverging wave transmission scheme was used to illuminate the full simulated arterial phantom volume at 1000 volumes per second.

With the adult transducer, high-volume-rate imaging was achieved (*in vitro*) using a gated acquisition of four beams-per-heartbeat over four heartbeats (16 beams total) to maintain a volume rate of 1000 volumes per second over a 60°× 60°field of view. This transmission scheme was used for 4D echoPIV analysis in a dynamic LV phantom, using tomographic PIV as a ground truth.

10.3.1. CHALLENGES

LATERAL RESOLUTION

The tracking results of the simulated arterial phantom were not very promising with the pediatric transducer. The experiment evaluated if we could estimate the high velocity flows expected in the trans-mitral jet. However, we found that the lateral resolution was

insufficient relative to the velocity gradients in the velocity profile, causing severe underestimation whenever steep velocity gradients were present. The simulated lateral resolution (FWHM of lateral PSF) of the pediatric transducer was ~ 5°, which translates to ~ 8 mm at 75 mm depth. For the 15mm diameter jet in **Chapter 9**, we believed this would have resulted in similar severe underestimations as those observed in **Chapter 7**. With the adult matrix transducer, the receive aperture was quadruple the area of the pediatric transducer, improving lateral resolution (~ 3°). However, lateral resolution was still a problem at more than 75 mm from the probe (~4 mm), where the formation of the jet through the mitral valve was severely underestimated. Although, the jet was still tracked well at shallower depths, showing good correspondence with the tomographic PIV results in terms of velocity magnitude, flow rate and the size and position of the vortex ring.

In **Chapter 9** the adult matrix TEE transducer was used in a transthoracic view, positioned at the apex oriented axially along the long axis of the LV. If, instead, we had chosen a more typical TEE view (oriented more perpendicular to the long axis of the LV) then the maximum depth required would have been reduced: improving lateral resolution and allowing for a higher pulse repetition frequency to be used. The downside of this approach is that the field of view required may be larger due to the long-axis view, requiring more beams to spatially sample the whole LV.

GRATING LOBES

The use of micro-beamforming groups results in grating lobes being generated during the coarse beamforming stage in receive (beamforming of the sub-arrays in software) [228]. Combining more elements into a sub-array results in reduced channel connections but also increases the effective pitch for the coarse beamforming stage, bringing grating lobes closer to the main lobe. With the pediatric transducer in **Chapter 7**, only 3x3 elements were combined in a sub-array, while 4x4 elements were combined in **Chapter 9**. Thus, it can be seen that by keeping the number of output channel connections constant, there is a trade-off between lateral resolution and grating lobe suppression. Grating lobes can be further suppressed by transmitting a narrower beam, so that less energy is transmitted to potential scatterrers in the grating lobe direction. However, this also requires a trade-off in frame-rate, if the field of view is kept constant, so that more beams are required to sample the same viewing angle.

PROCESSING TIME

Micro-beamforming, as used on the adult TEE transducer, greatly reduced the data bandwidth required for acquisition and storage of the received echo signals. However, beamforming in 3D is significantly more resource intensive than 2D beamforming and take significantly longer (~100 frames per second in 2D versus ~1 volume per second in 3D). With long beamforming and echoPIV computation times, exploratory parameter optimization becomes limited. For this reason, the echoPIV implementation used in **Chapter 9** utilized the GPU (Titan X, 12 GB) for performing the numerous FFT based 3D cross-correlations. However, far more optimizations are required for clinical use, as the typical time to process a dataset was in the order of 2 – 4 hours. Data storage may also become a

concern, as a single beamformed dataset was 40 GB in the adult TEE study (**Chapter 9**). Once a robust and sufficiently accurate 4D echoPIV system has been developed and validated, the focus of research will shift to improving performance. Too early optimization often reduces flexibility which is not desirable in the early stages of research.

VISUALIZATION

Being able to visualize the quantified flow data is important. Fortunately, many open source software packages exist for 3D rendering of volumes and vector fields (Paraview, MayAvi, Vtk, OpenGL). However, once the data is rendered it still needs to be displayed in 2D on your computer monitor. This makes exploring complex 4D flow data difficult and time consuming. Methods for efficiently interacting with 4D flow data would be beneficial not only to researchers developing 4D flow tracking techniques, but eventually also to the clinicians that use them. The recent advances in virtual/augmented reality headsets may offer more effective ways of interacting with complex 4D data-sets.

10.3.2. PERSPECTIVES FOR 4D ECHOPIV

BENEFITS OF 4D FLOW INFORMATION

The translation of 4D echoPIV to the clinic would allow for assessment of interesting fluid dynamics parameters with minimal assumptions, such as kinetic energy and its dissipation, pressure gradients and blood wash-out rate. Studying the development of vortices in the heart could be performed in 4D, removing planar flow assumptions as in current 2D studies. These parameters are currently evaluated by 4D-Flow MRI but at limited temporal resolution (20-30 phases per cycle). Using 4D echoPIV this could be increased by one or two orders of magnitude, potentially revealing transient flow patterns and events that are not visible using 4D-Flow MRI [112].

The relationship between pressure and volume in the LV contains a wealth of information on cardiac health and is visualized with a pressure-volume loop. Unfortunately pressure-volume loops are currently only obtainable in the clinic using invasive catheterization procedures. However, recent research has explored non-invasively calculating PV-loops using numerical models and MRI measured LV volumes over time [229]. These methods can be further improved using 4D flow data from 4D echoPIV (or 4D flow-MRI) to calculate local pressure gradients within the LV.

BENEFITS OF HFR 3D ULTRASOUND

The use of the HFR 3D ultrasound sequence described in **Chapter 9** may also be beneficial for applications outside of intra-cavity blood flow imaging. Such as 3D shear wave imaging [230], [231], 3D perfusion imaging, tracking valve dynamics and flow imaging in the coronary arteries and micro-circulation [232], [233].

COMPARISON WITH 4D-FLOW MRI

The LV phantom described in **Chapters 8 & 9** is also compatible with MRI imaging. At the time of writing this thesis we have acquired 4D-flow MRI acquisitions of the LV phantom and are busy with comparing the accuracy of 4D-flow MRI against tomographic PIV. This

will allow for direct comparison of 4D echoPIV with 4D-flow MRI using an independent reference technique (tomographic PIV).

10.4. CONCLUSION

The aim of this thesis was to measure the high velocity flow patterns in the LV and greater vessels. We sought to achieve this aim by using HFR echoPIV. In this thesis we have described methods in 2D to accurately quantify the high velocity blood flow patterns in both the LV and abdominal aorta, both *in vitro* and *in vivo*. Our feasibility study in the abdominal aorta of health volunteers prompted a continuation study on a larger set of patients undergoing different therapy options for stenotic lesions in the aorto-iliac tract (on-going at the time of writing this thesis). The feasibility of HFR echoPIV for quantifying intra-cardiac blood flow patterns was demonstrated and a continuation study is also planned on a larger population of patients.

In 3D we have used a prototype matrix TEE transducer to volumetrically image at 1000 volumes per second. We demonstrated that this imaging scheme could be used with echoPIV to image 4D blood flow patterns in a dynamic LV phantom. While further refinement is needed to overcome resolution constraints, imaging 4D LV blood flow patterns is on the horizon.

We have also developed a dynamic 3D LV phantom, capable of being imaged with optical, ultrasound and MRI. This phantom can be used in future to develop and test new probes, acquisition protocols and algorithms for flow imaging, with a tomographic PIV derived ground truth.

REFERENCES

[1] S. Tyrovolas, P. A. Lotufo, *et al.*, "Global, Regional, and National Burden of Cardiovascular Diseases for 10 Causes, 1990 to 2015", *Journal of the American College of Cardiology*, vol. 70, no. 1, pp. 1–25, 2017. DOI: 10.1016/j.jacc.2017.04.052.

[2] J. J. Charonko, R. Kumar, K. Stewart, W. C. Little, and P. P. Vlachos, "Vortices Formed on the Mitral Valve Tips Aid Normal Left Ventricular Filling", *Annals of Biomedical Engineering*, vol. 41, no. 5, pp. 1049–1061, May 2013. DOI: 10.1007/s10439-013-0755-0.

[3] F. Domenichini and G. Pedrizzetti, "Intraventricular vortex flow changes in the infarcted left ventricle: Numerical results in an idealised 3D shape", *Computer Methods in Biomechanics and Biomedical Engineering*, vol. 14, no. 1, pp. 95–101, 2011. DOI: 10.1080/10255842.2010.485987.

[4] P. J. Kilner, G.-Z. Yang, A. J. Wilkes, R. H. Mohiaddin, D. N. Firmin, and M. H. Yacoub, "Asymmetric redirection of flow through the heart", *Nature*, vol. 404, no. 6779, pp. 759–761, Apr. 2000. DOI: 10.1038/35008075.

[5] J. S. Meisner, C. Yoran, *et al.*, "Left ventricular filling dynamics: influence of left ventricular relaxation and left atrial pressure.", *Circulation*, vol. 74, no. 1, pp. 187–196, 2011. DOI: 10.1161/01.cir.74.1.187.

[6] G. Pedrizzetti, A. R. Martiniello, V. Bianchi, A. D'Onofrio, P. Caso, and G. Tonti, "Changes in electrical activation modify the orientation of left ventricular flow momentum: novel observations using echocardiographic particle image velocimetry", *European Heart Journal – Cardiovascular Imaging*, vol. 17, no. 2, pp. 203–209, Feb. 2016. DOI: 10.1093/ehjci/jev137.

[7] A. Pasipoularides, "Mechanotransduction Mechanisms for Intraventricular Diastolic Vortex Forces and Myocardial Deformations: Part 2", *Journal of Cardiovascular Translational Research*, vol. 8, no. 5, pp. 293–318, Jul. 2015. DOI: 10.1007/s12265-015-9630-8.

[8] A. Pasipoularides, "Mechanotransduction Mechanisms for Intraventricular Diastolic Vortex Forces and Myocardial Deformations: Part 1", *Journal of Cardiovascular Translational Research*, vol. 8, no. 5, pp. 293–318, Jul. 2015. DOI: 10.1007/s12265-015-9611-y.

[9] G. Pedrizzetti, G. La Canna, O. Alfieri, and G. Tonti, "The vortex—an early predictor of cardiovascular outcome?", *Nature Reviews Cardiology*, vol. 11, no. 9, pp. 545–553, Jun. 2014. DOI: 10.1038/nrcardio.2014.75.

[10] C. K. Zarins, D. P. Giddens, B. K. Bharadvaj, V. S. Sottiurai, R. F. Mabon, and S. Glagov, "Carotid bifurcation atherosclerosis. Quantitative correlation of plaque localization with flow velocity profiles and wall shear stress.", *Circulation research*, vol. 53, no. 4, pp. 502–14, Oct. 1983.

[11] E. J. Benjamin, S. S. Virani, *et al.*, *Heart disease and stroke statistics - 2018 update: A report from the American Heart Association*, 12. 2018, vol. 137, E67–E492. DOI: 10.1161/CIR.0000000000000558. arXiv: NIHMS150003.

[12] P. A. Heidenreich, N. M. Albert, *et al.*, "Forecasting the impact of heart failure in the united states a policy statement from the american heart association", *Circulation: Heart Failure*, vol. 6, no. 3, pp. 606–619, 2013. DOI: 10.1161/HHF.0b013e318291329a.

[13] J. A. J. Jensen, "Estimation of blood velocities using ultrasound: A Signal Processing Approach", Doctoral Thesis, 1996, p. 317.

[14] J. A. Jensen, S. I. Nikolov, *et al.*, "Recent advances in blood flow vector velocity imaging", *IEEE International Ultrasonics Symposium, IUS*, pp. 262–271, 2011. DOI: 10.1109/ULTSYM.2011.0064.

[15] P. P. Sengupta, G. Pedrizzetti, *et al.*, "Emerging trends in CV flow visualization", *JACC: Cardiovascular Imaging*, vol. 5, no. 3, pp. 305–316, 2012. DOI: 10.1016/j.jcmg.2012.01.003.

[16] J. A. Jensen, S. Nikolov, A. C. Yu, and D. Garcia, "Ultrasound Vector Flow Imaging: I: Sequential Systems", *IEEE Transactions on Ultrasonics, Ferroelectrics, and Frequency Control*, vol. 3010, no. 2, pp. 1–1, 2016. DOI: 10.1109/TUFFC.2016.2600763.

[17] J. Jensen, S. Nikolov, A. C. H. Yu, and D. Garcia, "Ultrasound Vector Flow Imaging: II: Parallel Systems", *IEEE Transactions on Ultrasonics, Ferroelectrics, and Frequency Control*, vol. 3010, no. c, pp. 1–1, 2016. DOI: 10.1109/TUFFC.2016.2598180.

[18] B. Dunmire, K. W. Beach, K. H. Labs, M. Plett, and D. E. Strandness, "Cross-beam vector Doppler ultrasound for angle-independent velocity measurements", *Ultrasound in Medicine and Biology*, vol. 26, no. 8, pp. 1213–1235, 2000. DOI: 10.1016/S0301-5629(00)00287-8.

[19] M. D. Fox, "Multiple crossed-beam ultrasound Doppler velocimetry", *IEEE Transactions on Sonics and Ultrasonics*, vol. 25, no. 5, pp. 281–286, 1978. DOI: 10.1109/T-SU.1978.31028.

[20] J. R. Overbeck, K. W. Beach, and D. E. Strandness, "Vector doppler: Accurate measurement of blood velocity in two dimensions", *Ultrasound in Medicine and Biology*, vol. 18, no. 1, pp. 19–31, 1992. DOI: 10.1016/0301-5629(92)90004-T.

[21] F. Calliada, M. Fanizza, *et al.*, "High-frame rate vector flow imaging of the carotid bifurcation", *Insights into Imaging*, vol. 8, no. 3, pp. 319–328, 2017. DOI: 10.1007/s13244-017-0554-5.

[22] J. Jensen and P. Munk, "A new method for estimation of velocity vectors", *IEEE Transactions on Ultrasonics, Ferroelectrics and Frequency Control*, vol. 45, no. 3, pp. 837–851, May 1998. DOI: 10.1109/58.677749.

[23] J. A. Jensen, A. H. Brandt, and M. B. Nielsen, "Convex array vector velocity imaging using transverse oscillation and its optimization", *IEEE Transactions on Ultrasonics, Ferroelectrics, and Frequency Control*, vol. 62, no. 12, pp. 2043–2053, 2015. DOI: 10.1109/TUFFC.2015.006970.

[24] M. J. Pihl, J. Marcher, and J. Jensen, "Phased-array vector velocity estimation using transverse oscillations", *IEEE Transactions on Ultrasonics, Ferroelectrics, and Frequency Control*, vol. 59, no. 12, pp. 2662–2675, 2012. DOI: 10.1109/TUFFC.2012.2507.

[25] S. Holbek, K. L. Hansen, *et al.*, "Real-time 2-d phased array vector flow imaging", *IEEE Transactions on Ultrasonics, Ferroelectrics, and Frequency Control*, vol. 65, no. 7, pp. 1205–1213, 2018. DOI: 10.1109/TUFFC.2018.2838518.

[26] M. M. Pedersen, M. J. Pihl, *et al.*, "Comparison of Real-Time In Vivo Spectral and Vector Velocity Estimation", *Ultrasound in Medicine and Biology*, vol. 38, no. 1, pp. 145–151, 2012. DOI: 10.1016/j.ultrasmedbio.2011.10.003.

[27] S. Ohtsuki and M. Tanaka, "The flow velocity distribution from the doppler information on a plane in three-Dimensional flow", *Journal of Visualization*, vol. 9, no. 1, pp. 69–82, 2006. DOI: 10.1007/BF03181570.

[28] T. Uejima, A. Koike, *et al.*, "A New Echocardiographic Method for Identifying Vortex Flow in the Left Ventricle: Numerical Validation", *Ultrasound in Medicine & Biology*, vol. 36, no. 5, pp. 772–788, May 2010. DOI: 10.1016/j.ultrasmedbio.2010.02.017.

[29] D. Garcia, J. C. del Álamo, *et al.*, "Two-Dimensional Intraventricular Flow Mapping by Digital Processing Conventional Color-Doppler Echocardiography Images", *IEEE Transactions on Medical Imaging*, vol. 29, no. 10, pp. 1701–1713, Oct. 2010. DOI: 10.1109/TMI.2010.2049656.

[30] T. Tanaka, R. Asami, *et al.*, "Intracardiac VFM technique using diagnostic ultrasound system", *Hitachi Review*, vol. 64, no. 8, pp. 488–492, 2015.

[31] F. Mehregan, F. Tournoux, *et al.*, "Doppler Vortography: A Color Doppler Approach to Quantification of Intraventricular Blood Flow Vortices", *Ultrasound in Medicine & Biology*, vol. 40, no. 1, pp. 210–221, Jan. 2014. DOI: 10.1016/j.ultrasmedbio.2013.09.013.

[32] F. Tournoux, D. Garcia, *et al.*, "Intracardiac Vortex dynamics by high-frame-rate doppler vortography-in vivo comparison with vector flow mapping and 4-d flow mri", *IEEE Transactions on Ultrasonics, Ferroelectrics, and Frequency Control*, vol. 64, no. 2, pp. 424–432, 2017. DOI: 10.1109/TUFFC.2016.2632707.

[33] R. F. Wagner, S. W. Smith, J. M. Sandrik, and H. Lopez, "Statistics of Speckle in Ultrasound B-Scans", *IEEE Transactions on Sonics and Ultrasonics*, vol. 30, no. 3, pp. 156–163, 1983. DOI: 10.1109/T-SU.1983.31404.

[34] S. Fadnes, S. A. Nyrnes, H. Torp, and L. Lovstakken, "Shunt Flow Evaluation in Congenital Heart Disease Based on Two-Dimensional Speckle Tracking", *Ultrasound in Medicine & Biology*, vol. 40, no. 10, pp. 2379–2391, Oct. 2014. DOI: 10.1016/j.ultrasmedbio.2014.03.029.

[35] S. Fadnes, M. S. Wigen, S. A. Nyrnes, and L. Lovstakken, "In Vivo Intracardiac Vector Flow Imaging Using Phased Array Transducers for Pediatric Cardiology", *IEEE Transactions on Ultrasonics, Ferroelectrics, and Frequency Control*, vol. 64, no. 9, pp. 1318–1326, Sep. 2017. DOI: 10.1109/TUFFC.2017.2689799.

[36] H. Takahashi, H. Hasegawa, and H. Kanai, "Echo speckle imaging of blood particles with high-frame-rate echocardiography", *Japanese Journal of Applied Physics*, vol. 53, no. 7S, 07KF08, 2014. DOI: 10.7567/JJAP.53.07KF08.

[37] N. de Jong, F. J. Ten Cate, C. T. Lancée, J. R. T. C. Roelandt, and N. Bom, "Principles and Recent Developments in Ultrasound Contrast Agents", *Ultrasonics*, vol. 29, no. 4, pp. 324–330, 1991. DOI: Doi10.1016/0041-624x(91)90030-C.

[38] T. Segers, "Monodisperse bubbles and droplets for medical applications", PhD Thesis, University of Twente, Enschede, The Netherlands, May 2015. DOI: 10.3990/1.9789036538992.

[39] G. A. Brock-Fisher, M. D. Poland, and P. G. Rafter, *Means for increasing sensitivity in non-linear ultrasound imaging systems*, 1996.

[40] C. S. Chapman and J. C. Lazenby, *Ultrasound imaging system employing phase inversion subtraction to enhance the image*, 1997.

[41] J. Hwang and D. Simpson, *Two pulse technique for ultrasonic harmonic imaging*, 1999.

[42] H. B. Kim, J. R. Hertzberg, and R. Shandas, "Development and validation of echo PIV", *Experiments in Fluids*, vol. 36, no. 3, pp. 455–462, 2004. DOI: 10.1007/s00348-003-0743-5.

[43] A. Kheradvar, H. Houle, *et al.*, "Echocardiographic Particle Image Velocimetry: A Novel Technique for Quantification of Left Ventricular Blood Vorticity Pattern", *Journal of the American Society of Echocardiography*, vol. 23, no. 1, pp. 86–94, Jan. 2010. DOI: 10.1016/j.echo.2009.09.007.

[44] C. Prinz, R. Faludi, *et al.*, "Can echocardiographic particle image velocimetry correctly detect motion patterns as they occur in blood inside heart chambers? A validation study using moving phantoms", *Cardiovascular Ultrasound*, vol. 10, no. 1, p. 24, Dec. 2012. DOI: 10.1186/1476-7120-10-24.

[45] H. Gao, P. Claus, M. S. Amzulescu, I. Stankovic, J. D'Hooge, and J. U. Voigt, "How to optimize intracardiac blood flow tracking by echocardiographic particle image velocimetry? Exploring the influence of data acquisition using computer-generated data sets", *European Heart Journal Cardiovascular Imaging*, vol. 13, no. 6, pp. 490–499, 2012. DOI: 10.1093/ejechocard/jer285.

[46] S. Cimino, G. Pedrizzetti, *et al.*, "In vivo analysis of intraventricular fluid dynamics in healthy hearts", *European Journal of Mechanics, B/Fluids*, vol. 35, pp. 40–46, 2012. DOI: 10.1016/j.euromechflu.2012.03.014.

[47] L. Agati, S. Cimino, *et al.*, "Quantitative analysis of intraventricular blood flow dynamics by echocardiographic particle image velocimetry in patients with acute myocardial infarction at different stages of left ventricular dysfunction.", *European heart journal cardiovascular Imaging*, no. Lv, pp. 1–10, 2014. DOI: 10.1093/ehjci/jeu106.

[48] J.-W. Son, W.-J. Park, *et al.*, "Abnormal Left Ventricular Vortex Flow Patterns in Association With Left Ventricular Apical Thrombus Formation in Patients With Anterior Myocardial Infarction", *Circulation Journal*, vol. 76, no. 11, pp. 2640–2646, 2012. DOI: 10.1253/circj.CJ-12-0360.

[49] G.-R. Hong, G. Pedrizzetti, *et al.*, "Characterization and quantification of vortex flow in the human left ventricle by contrast echocardiography using vector particle image velocimetry.", *JACC. Cardiovascular imaging*, vol. 1, no. 6, pp. 705–717, 2008. DOI: 10.1016/j.jcmg.2008.06.008.

[50] H. Abe, G. Caracciolo, *et al.*, "Contrast echocardiography for assessing left ventricular vortex strength in heart failure: A prospective cohort study", *European Heart Journal Cardiovascular Imaging*, vol. 14, no. 11, pp. 1049–1060, 2013. DOI: 10.1093/ehjci/jet049.

[51] G. Goliasch, K. Goscinska-Bis, *et al.*, "CRT improves LV filling dynamics: Insights from echocardiographic particle imaging velocimetry", *JACC: Cardiovascular Imaging*, vol. 6, no. 6, pp. 704–713, 2013. DOI: 10.1016/j.jcmg.2013.04.004.

[52] S. Cimino, D. Palombizio, *et al.*, "Significant increase of flow kinetic energy in "nonresponders" patients to cardiac resynchronization therapy", *Echocardiography*, vol. 34, no. 5, pp. 709–715, 2017. DOI: 10.1111/echo.13518.

[53] R. Faludi, M. Szulik, *et al.*, "Left ventricular flow patterns in healthy subjects and patients with prosthetic mitral valves: An in vivo study using echocardiographic particle image velocimetry", *Journal of Thoracic and Cardiovascular Surgery*, vol. 139, no. 6, pp. 1501–1510, 2010. DOI: 10.1016/j.jtcvs.2009.07.060.

[54] S. Kutty, L. Li, *et al.*, "Effects of Right Ventricular Hemodynamic Burden on Intraventricular Flow in Tetralogy of Fallot: An Echocardiographic Contrast Particle Imaging Velocimetry Study", *Journal of the American Society of Echocardiography*, vol. 27, no. 12, pp. 1311–1318, 2014. DOI: 10.1016/j.echo.2014.09.016.

[55] K.-H. Park, J.-W. Son, *et al.*, "Characterization of the Left Atrial Vortex Flow by Two-Dimensional Transesophageal Contrast Echocardiography Using Particle Image Velocimetry", *Ultrasound in Medicine & Biology*, vol. 39, no. 1, pp. 62–71, 2012. DOI: 10.1016/j.ultrasmedbio.2012.08.013.

[56] D. Mele, V. Smarrazzo, *et al.*, "Intracardiac Flow Analysis: Techniques and Potential Clinical Applications", *Journal of the American Society of Echocardiography*, 2019. DOI: 10.1016/j.echo.2018.10.018.

[57] C. Poelma, "Ultrasound Imaging Velocimetry: a review", *Experiments in Fluids*, vol. 58, no. 1, p. 3, Jan. 2017. DOI: 10.1007/s00348-016-2283-9.

[58] M. Tanter and M. Fink, "Ultrafast imaging in biomedical ultrasound", *IEEE Transactions on Ultrasonics, Ferroelectrics, and Frequency Control*, vol. 61, no. 1, pp. 102–119, 2014. DOI: 10.1109/TUFFC.2014.6689779.

[59] C. Papadacci, M. Pernot, M. Couade, M. Fink, and M. Tanter, "High-contrast ultrafast imaging of the heart", *IEEE Transactions on Ultrasonics, Ferroelectrics, and Frequency Control*, vol. 61, no. 2, pp. 288–301, 2014. DOI: 10.1109/TUFFC.2014.6722614.

[60] J. Voorneveld, P. Kruizinga, *et al.*, "Native blood speckle vs ultrasound contrast agent for particle image velocimetry with ultrafast ultrasound - in vitro experiments", in *2016 IEEE International Ultrasonics Symposium (IUS)*, IEEE, Sep. 2016, pp. 1–4. DOI: 10.1109/ULTSYM.2016.7728614.

[61] C. H. Leow, E. Bazigou, R. J. Eckersley, A. C. Yu, P. D. Weinberg, and M.-X. Tang, "Flow Velocity Mapping Using Contrast Enhanced High-Frame-Rate Plane Wave Ultrasound and Image Tracking: Methods and Initial in Vitro and in Vivo Evaluation", *Ultrasound in Medicine & Biology*, vol. 41, no. 11, pp. 2913–2925, Nov. 2015. DOI: 10.1016/j.ultrasmedbio.2015.06.012.

[62] C. Demene, T. Deffieux, *et al.*, "Spatiotemporal Clutter Filtering of Ultrafast Ultrasound Data Highly Increases Doppler and fUltrasound Sensitivity", *IEEE Transactions on Medical Imaging*, vol. 34, no. 11, pp. 2271–2285, Nov. 2015. DOI: 10.1109/TMI.2015.2428634.

[63] K. V. Ramnarine, D. K. Nassiri, P. R. Hoskins, and J. Lubbers, "Validation of a new blood-mimicking fluid for use in Doppler flow test objects", *Ultrasound in Medicine and Biology*, vol. 24, no. 3, pp. 451–459, 1998. DOI: 10.1016/S0301-5629(97)00277-9.

[64] J. Y. Lu, "2D and 3D High Frame Rate Imaging with Limited Diffraction Beams", *IEEE Transactions on Ultrasonics, Ferroelectrics, and Frequency Control*, vol. 44, no. 4, pp. 839–856, 1997. DOI: 10.1109/58.655200.

[65] W. Thielicke and E. J. Stamhuis, "PIVlab – Towards User-friendly, Affordable and Accurate Digital Particle Image Velocimetry in MATLAB", *Journal of Open Research Software*, vol. 2, no. 22, pp. 10 280–10 285, Oct. 2014. DOI: 10.5334/jors.bl. arXiv: K26HX2P53NR16411.

[66] J. Voorneveld, S. Engelhard, *et al.*, "High Frame Rate Contrast-Enhanced Ultrasound for Velocimetry in the Human Abdominal Aorta", *IEEE Transactions on Ultrasonics, Ferroelectrics, and Frequency Control*, vol. 65, no. 12, pp. 2245–2254, 2018. DOI: 10.1109/TUFFC.2018.2846416.

[67] D. E. Conway, M. R. Williams, S. G. Eskin, and L. V. McIntire, "Endothelial cell responses to atheroprone flow are driven by two separate flow components: low time-average shear stress and fluid flow reversal", *AJP: Heart and Circulatory Physiology*, vol. 298, no. 2, H367–H374, 2010. DOI: 10.1152/ajpheart.00565.2009.

[68] A. Harloff, A. Nußbaumer, *et al.*, "In vivo assessment of wall shear stress in the atherosclerotic aorta using flow-sensitive 4D MRI", *Magnetic Resonance in Medicine*, vol. 63, no. 6, pp. 1529–1536, Apr. 2010. DOI: 10.1002/mrm.22383.

[69] L. H. Timmins, D. S. Molony, *et al.*, "Oscillatory wall shear stress is a dominant flow characteristic affecting lesion progression patterns and plaque vulnerability in patients with coronary artery disease", *Journal of The Royal Society Interface*, vol. 14, no. 127, p. 20 160 972, Feb. 2017. DOI: 10.1098/rsif.2016.0972.

[70] J. C. Lasheras, "The Biomechanics of Arterial Aneurysms", *Annual Review of Fluid Mechanics*, vol. 39, no. 1, pp. 293–319, Jan. 2007. DOI: 10.1146/annurev.fluid.39.050905.110128.

[71] J. T. Boersen, E. Groot Jebbink, *et al.*, "Flow and wall shear stress characterization after endovascular aneurysm repair and endovascular aneurysm sealing in an infrarenal aneurysm model", *Journal of Vascular Surgery*, vol. 66, no. 6, pp. 1844–1853, Dec. 2017. DOI: 10.1016/j.jvs.2016.10.077.

[72] E. Groot Jebbink, V. Mathai, *et al.*, "Hemodynamic comparison of stent configurations used for aortoiliac occlusive disease", *Journal of Vascular Surgery*, vol. 66, no. 1, pp. 251–260, 2017. DOI: 10.1016/j.jvs.2016.07.128.

[73] S. F. C. Stewart, "Effects of transducer, velocity, Doppler angle, and instrument settings on the accuracy of color Doppler ultrasound", *Ultrasound in Medicine and Biology*, vol. 27, no. 4, pp. 551–564, 2001. DOI: 10.1016/S0301-5629(01)00357-X.

[74] P. Tortoli, M. Lenge, D. Righi, G. Ciuti, H. Liebgott, and S. Ricci, "Comparison of Carotid Artery Blood Velocity Measurements by Vector and Standard Doppler Approaches", *Ultrasound in Medicine & Biology*, vol. 41, no. 5, pp. 1354–1362, May 2015. DOI: 10.1016/j.ultrasmedbio.2015.01.008.

[75] L. N. Bohs, B. H. Friemel, and G. E. Trahey, "Experimental velocity profiles and volumetric flow via two-dimensional speckle tracking", *Ultrasound in Medicine & Biology*, vol. 21, no. 7, pp. 885–898, Jan. 1995. DOI: 10.1016/0301-5629(95)00034-O.

[76] Y. Desailly, A.-M. Tissier, J.-M. Correas, F. Wintzenrieth, M. Tanter, and O. Couture, "Contrast enhanced ultrasound by real-time spatiotemporal filtering of ultrafast images", *Physics in Medicine and Biology*, vol. 62, no. 1, pp. 31–42, 2017. DOI: 10.1088/1361-6560/62/1/31.

[77] O. Couture, M. Fink, and M. Tanter, "Ultrasound contrast plane wave imaging", *IEEE Transactions on Ultrasonics, Ferroelectrics, and Frequency Control*, vol. 59, no. 12, pp. 2676–2683, 2012. DOI: 10.1109/TUFFC.2012.2508.

[78] C. Tremblay-Darveau, R. Williams, L. Milot, M. Bruce, and P. N. Burns, "Combined perfusion and doppler imaging using plane-wave nonlinear detection and microbubble contrast agents", *IEEE Transactions on Ultrasonics, Ferroelectrics, and Frequency Control*, vol. 61, no. 12, pp. 1988–2000, 2014. DOI: 10.1109/TUFFC.2014.006573.

[79] M. Toulemonde, R. J. Eckersley, and M.-X. Tang, "High frame rate contrast enhanced echocardiography : Microbubbles stability and contrast evaluation", in *IEEE International Ultrasonics Symposium (IUS)*, 2017.

[80] L. Liu, H. Zheng, *et al.*, "Development of a custom-designed echo particle image velocimetry system for multi-component hemodynamic measurements: system characterization and initial experimental results.", *Physics in medicine and biology*, vol. 53, no. 5, pp. 1397–1412, 2008. DOI: 10.1088/0031-9155/53/5/015.

[81] T. A. Whittingham, "Contrast-Specific Imaging Techniques: Technical Perspective", in *Contrast Media in Ultrasonography*, Berlin/Heidelberg: Springer-Verlag, 2005, pp. 43–70. DOI: 10.1007/3-540-27214-3_4.

[82] A. Yu and L. Lovstakken, "Eigen-based clutter filter design for ultrasound color flow imaging: a review", *IEEE Transactions on Ultrasonics, Ferroelectrics and Frequency Control*, vol. 57, no. 5, pp. 1096–1111, May 2010. DOI: 10.1109/TUFFC.2010.1521.

[83] J. Viti, H. Vos, N. De Jong, F. Guidi, and P. Tortoli, "Detection of Contrast Agents: Plane Wave vs Focused Transmission", *IEEE Transactions on Ultrasonics, Ferroelectrics, and Frequency Control*, vol. 63, no. 2, pp. 203–211, 2016. DOI: 10.1109/TUFFC.2015.2504546.

[84] R. J. Adrian and J. Westerweel, *Particle Image Velocimetry*. Cambridge University Press, 2011.

[85] B. Y. Yiu, S. S. Lai, and A. C. Yu, "Vector Projectile Imaging: Time-Resolved Dynamic Visualization of Complex Flow Patterns", *Ultrasound in Medicine and Biology*, vol. 40, no. 9, pp. 2295–2309, 2014. DOI: 10.1016/j.ultrasmedbio.2014.03.014.

[86] F. A. Duck, "Nonlinear acoustics in diagnostic ultrasound", *Ultrasound in Medicine & Biology*, vol. 28, no. 1, pp. 1–18, Jan. 2002. DOI: 10.1016/S0301-5629(01)00463-X.

[87] M.-x. Tang and R. Eckersley, "Nonlinear propagation of ultrasound through microbubble contrast agents and implications for imaging", *IEEE Transactions on Ultrasonics, Ferroelectrics and Frequency Control*, vol. 53, no. 12, pp. 2406–2415, Dec. 2006. DOI: 10.1109/TUFFC.2006.189.

[88] G. L. ten Kate, G. G. Renaud, *et al.*, "Far-Wall Pseudoenhancement During Contrast-Enhanced Ultrasound of the Carotid Arteries: Clinical Description and In Vitro Reproduction", *Ultrasound in Medicine & Biology*, vol. 38, no. 4, pp. 593–600, Apr. 2012. DOI: 10.1016/j.ultrasmedbio.2011.12.019.

[89] J. S. Lum, D. M. Stobbe, T. W. Murray, and M. A. Borden, "Single microbubble measurements of temperature dependent viscoelastic properties", in *2017 IEEE International Ultrasonics Symposium (IUS)*, IEEE, Sep. 2017. DOI: 10.1109/ULTSYM.2017.8092134.

[90] H. Mulvana, E. Stride, J. V. Hajnal, and R. J. Eckersley, "Temperature Dependent Behavior of Ultrasound Contrast Agents", *Ultrasound in Medicine & Biology*, vol. 36, no. 6, pp. 925–934, Jun. 2010. DOI: 10.1016/j.ultrasmedbio.2010.03.003.

[91] H. Vos, M. Emmer, and N. de Jong, "Oscillation of single microbubbles at room versus body temperature", in *2008 IEEE Ultrasonics Symposium*, IEEE, Nov. 2008, pp. 982–984. DOI: 10.1109/ULTSYM.2008.0237.

[92] A. A. Brayman, M. Azadniv, M. W. Miller, and R. S. Meltzer, "Effect of static pressure on acoustic transmittance of Albunex (R) microbubble suspensions", *The Journal of the Acoustical Society of America*, vol. 99, no. 4, pp. 2403–2408, Apr. 1996. DOI: 10.1121/1.415428.

[93] M. Itani and R. F. Mattrey, "The Effect of Inhaled Gases on Ultrasound Contrast Agent Longevity In Vivo", *Molecular Imaging and Biology*, vol. 14, no. 1, pp. 40–46, Feb. 2012. DOI: 10.1007/s11307-011-0475-5.

[94] J. J. Kwan and M. A. Borden, "Microbubble Dissolution in a Multigas Environment", *Langmuir*, vol. 26, no. 9, pp. 6542–6548, May 2010. DOI: 10.1021/la904088p.

[95] G. Montaldo, M. Tanter, J. Bercoff, N. Benech, and M. Fink, "Coherent plane-wave compounding for very high frame rate ultrasonography and transient elastography", *IEEE Transactions on Ultrasonics, Ferroelectrics, and Frequency Control*, vol. 56, no. 3, pp. 489–506, 2009. DOI: 10.1109/TUFFC.2009.1067.

[96] B. Denarie, T. A. Tangen, *et al.*, "Coherent plane wave compounding for very high frame rate ultrasonography of rapidly moving targets", *IEEE Transactions on Medical Imaging*, vol. 32, no. 7, pp. 1265–1276, 2013. DOI: 10.1109/TMI.2013.2255310.

[97] C. H. Leow and M.-X. Tang, "Spatio-Temporal Flow and Wall Shear Stress Mapping Based on Incoherent Ensemble-Correlation of Ultrafast Contrast Enhanced Ultrasound Images", *Ultrasound in Medicine & Biology*, vol. 44, no. 1, pp. 134–152, Jan. 2018. DOI: 10.1016/j.ultrasmedbio.2017.08.930.

[98] United states Food and Drug Administration, *Guidance for Industry and FDA Staff - Information for Manufacturers Seeking Marketing Clearance of Diagnostic Ultrasound Systems and Transducers*, 2008.

[99] S. A. Engelhard, J. Voorneveld, *et al.*, "High-Frame-Rate, Contrast-enhanced Ultrasound Particle Image Velocimetry in the Abdominal Aorta: first human results", *Radiology*, vol. 289, no. 1, pp. 119–125, Jul. 2018. DOI: 10.1148/radiol.2018172979.

[100] J. B. Michel, J. L. Martin-Ventura, *et al.*, "Novel aspects of the pathogenesis of aneurysms of the abdominal aorta in humans", *Cardiovascular Research*, vol. 90, no. 1, pp. 18–27, 2011. DOI: 10.1093/cvr/cvq337.

[101] A. Greiner, H. Mu, *et al.*, "Does Stent Overlap Influence the Patency Rate of Aortoiliac Kissing Stents ?", *Journal of Endovascular Therapy*, vol. 12, pp. 696–703, 2005.

[102] M. J. Sharafuddin, J. J. Hoballah, *et al.*, "Long-term outcome following stent reconstruction of the aortic bifurcation and the role of geometric determinants.", *Annals of vascular surgery*, vol. 22, no. 3, pp. 346–57, 2008. DOI: 10.1016/j.avsg.2007.12.013.

[103] F. Zhang, C. Lanning, *et al.*, "In vitro and preliminary in vivo validation of echo particle image velocimetry in carotid vascular imaging", *Ultrasound in Medicine and Biology*, vol. 37, no. 3, pp. 450–464, 2011. DOI: 10.1016/j.ultrasmedbio.2010.11.017.

[104] P. Garg, J. J. Westenberg, *et al.*, "Comparison of fast acquisition strategies in whole-heart four-dimensional flow cardiac MR: Two-center, 1.5 Tesla, phantom and in vivo validation study", *Journal of Magnetic Resonance Imaging*, vol. 47, no. 1, pp. 272–281, Jan. 2018. DOI: 10.1002/jmri.25746.

[105] J. Kwan and M. Borden, "Microbubble shell break-up and collapse during gas exchange", in *2010 IEEE International Ultrasonics Symposium*, IEEE, Oct. 2010, pp. 897–899. DOI: 10.1109/ULTSYM.2010.5935938.

[106] J. Voorneveld, A. Muralidharan, *et al.*, "High Frame Rate Ultrasound Particle Image Velocimetry for Estimating High Velocity Flow Patterns in the Left Ventricle", *IEEE Transactions on Ultrasonics, Ferroelectrics, and Frequency Control*, vol. 65, no. 12, pp. 2222–2232, 2017. DOI: 10.1109/TUFFC.2017.2786340.

[107] A. Kheradvar, R. Assadi, A. Falahatpisheh, and P. P. Sengupta, "Assessment of Transmitral Vortex Formation in Patients with Diastolic Dysfunction", *Journal of the American Society of Echocardiography*, vol. 25, no. 2, pp. 220–227, Feb. 2012. DOI: 10.1016/j.echo.2011.10.003.

[108] P. Martínez-Legazpi, J. Bermejo, *et al.*, "Contribution of the Diastolic Vortex Ring to Left Ventricular Filling", *Journal of the American College of Cardiology*, vol. 64, no. 16, pp. 1711–1721, Oct. 2014. DOI: 10.1016/j.jacc.2014.06.1205.

[109] G. Pedrizzetti and F. Domenichini, "Left Ventricular Fluid Mechanics: The Long Way from Theoretical Models to Clinical Applications", *Annals of Biomedical Engineering*, vol. 43, no. 1, pp. 26–40, Jan. 2015. DOI: 10.1007/s10439-014-1101-x.

[110] M. Gharib, E. Rambod, A. Kheradvar, D. J. Sahn, and J. O. Dabiri, "Optimal vortex formation as an index of cardiac health", *Proceedings of the National Academy of Sciences*, vol. 103, no. 16, pp. 6305–6308, Apr. 2006. DOI: 10.1073/pnas.0600520103.

[111] P. M. Arvidsson, S. J. Kovács, *et al.*, "Vortex ring behavior provides the epigenetic blueprint for the human heart", *Scientific Reports*, vol. 6, no. 1, p. 22 021, Apr. 2016. DOI: 10.1038/srep22021.

[112] C. Chnafa, S. Mendez, and F. Nicoud, "Image-Based Simulations Show Important Flow Fluctuations in a Normal Left Ventricle: What Could be the Implications?", *Annals of Biomedical Engineering*, vol. 44, no. 11, pp. 3346–3358, Nov. 2016. DOI: 10.1007/s10439-016-1614-6.

[113] K. L. Hansen, H. Møller-Sørensen, J. Kjaergaard, M. B. Jensen, J. A. Jensen, and M. B. Nielsen, "Aortic Valve Stenosis Increases Helical Flow and Flow Complexity: A Study of Intra-Operative Cardiac Vector Flow Imaging", *Ultrasound in Medicine & Biology*, vol. 43, no. 8, pp. 1607–1617, Aug. 2017. DOI: 10.1016/j.ultrasmedbio.2017.03.018.

[114] K. L. Hansen, M. M. Pedersen, *et al.*, "Intraoperative Cardiac Ultrasound Examination Using Vector Flow Imaging", *Ultrasonic Imaging*, vol. 35, no. 4, pp. 318–332, Oct. 2013. DOI: 10.1177/0161734613505552.

[115] J. A. Jensen, "Directional Transverse Oscillation Vector Flow Estimation", *IEEE Transactions on Ultrasonics, Ferroelectrics, and Frequency Control*, vol. 64, no. 8, pp. 1194–1204, Aug. 2017. DOI: 10.1109/TUFFC.2017.2710361.

[116] J. Van Cauwenberge, L. Lovstakken, *et al.*, "Assessing the Performance of Ultrafast Vector Flow Imaging in the Neonatal Heart via Multiphysics Modeling and In Vitro Experiments", *IEEE Transactions on Ultrasonics, Ferroelectrics, and Frequency Control*, vol. 63, no. 11, pp. 1772–1785, Nov. 2016. DOI: 10.1109/TUFFC.2016.2596804.

[117] H. Gao, N. Bijnens, D. Coisne, M. Lugiez, M. Rutten, and J. D'hooge, "2-D Left Ventricular Flow Estimation by Combining Speckle Tracking With Navier–Stokes-Based Regularization: An In Silico, In Vitro and In Vivo Study", *Ultrasound in Medicine & Biology*, vol. 41, no. 1, pp. 99–113, Jan. 2015. DOI: 10.1016/j.ultrasmedbio.2014.08.022.

[118] C. T. Metz, N. Baka, *et al.*, "Regression-Based Cardiac Motion Prediction From Single-Phase CTA", *IEEE Transactions on Medical Imaging*, vol. 31, no. 6, pp. 1311–1325, Jun. 2012. DOI: 10.1109/TMI.2012.2190938.

[119] H. A. Kirişli, M. Schaap, *et al.*, "Evaluation of a multi-atlas based method for segmentation of cardiac CTA data: a large-scale, multicenter, and multivendor study", *Medical Physics*, vol. 37, no. 12, pp. 6279–6291, Nov. 2010. DOI: 10.1118/1.3512795.

[120] J. Westerweel, "Digital particle image velocimetry - Theory and Application", Ph.D. dissertation, Delft University of Technology, 1993.

[121] J. Westerweel and F. Scarano, "Universal outlier detection for PIV data", *Experiments in Fluids*, vol. 39, no. 6, pp. 1096–1100, Dec. 2005. DOI: 10.1007/s00348-005-0016-6.

[122] S. Kefayati and T. L. Poepping, "Transitional flow analysis in the carotid artery bifurcation by proper orthogonal decomposition and particle image velocimetry", *Medical Engineering & Physics*, vol. 35, no. 7, pp. 898–909, Jul. 2013. DOI: 10.1016/j.medengphy.2012.08.020.

[123] K. E. Meyer, J. M. Pedersen, and O. ÖzcaN, "A turbulent jet in crossflow analysed with proper orthogonal decomposition", *Journal of Fluid Mechanics*, vol. 583, p. 199, Jul. 2007. DOI: 10.1017/S0022112007006143.

[124] L. Grinberg, A. Yakhot, and G. E. Karniadakis, "Analyzing Transient Turbulence in a Stenosed Carotid Artery by Proper Orthogonal Decomposition", *Annals of Biomedical Engineering*, vol. 37, no. 11, pp. 2200–2217, Nov. 2009. DOI: 10.1007/s10439-009-9769-z.

[125] A. Chatterjee, "An introduction to the proper orthogonal decomposition", *Current Science*, vol. 78, no. 7, pp. 808–817, 2000. DOI: 10.1109/LPT.2009.2020494. arXiv: 052186571997805218657 15.

[126] K. E. Meyer, D. Cavar, and J. M. Pedersen, "POD as tool for comparison of PIV and LES data", *7th International Symposium on Particle Image Velocimetry*, pp. 1–12, 2007.

[127] L. Sirovich, "Turbulence and the dynamics of coherent structures part i: coherent structures", *Quarterly of Applied Mathematics*, vol. XLV, no. 3, pp. 561–571, 1987. DOI: 10.3109/10717544.2013.779332.

[128] B.-F. Osmanski, S. Pezet, A. Ricobaraza, Z. Lenkei, and M. Tanter, "Functional ultrasound imaging of intrinsic connectivity in the living rat brain with high spatiotemporal resolution", *Nature Communications*, vol. 5, p. 5023, Oct. 2014. DOI: 10.1038/ncomms6023.

[129] A. Fatemi, H. Torp, S. Aakhus, and A. Rodriguez-Molares, "Increased clutter level in echocardiography due to specular reflection", in *Proc. SPIE , Medical Imaging 2017: Ultrasonic Imaging and Tomography*, N. Duric and B. Heyde, Eds., Mar. 2017, p. 101391D. DOI: 10.1117/12.2255721.

[130] J. Voorneveld, L. B. Keijzer, *et al.*, "High-Frame-Rate Echo-Particle Image Velocimetry Can Measure the High-Velocity Diastolic Flow Patterns", *Circulation: Cardiovascular Imaging*, vol. 12, no. 4, Apr. 2019. DOI: 10.1161/CIRCIMAGING.119.008856.

[131] M. E. Toulemonde, R. Corbett, *et al.*, "High Frame-Rate Contrast Echocardiography: In-Human Demonstration", *JACC: Cardiovascular Imaging*, vol. 11, no. 6, pp. 923–924, 2018. DOI: 10.1016/j.jcmg.2017.09.011.

[132] J. D. Voorneveld, D. Bera, A. van der Steen, N. de Jong, and J. G. Bosch, "Particle image velocimetry on simulated 3D ultrafast ultrasound from pediatric matrix TEE transducers", in *Proc. SPIE, Medical Imaging 2017*, vol. 10139, 2017, pp. 1–9. DOI: 10.1117/12.2254436.

[133] M. Correia, J. Provost, M. Tanter, M. Pernot, and I. Langevin, "In-vivo 4D Ultrafast Vector Flow Imaging : quantitative assessment of arterial blood flow", in *IEEE International Ultrasonics Symposium (IUS)*, 2016, pp. 2–5.

[134] M. J. Pihl, M. B. Stuart, B. G. Tomov, M. F. Rasmussen, and J. A. Jensen, "A Transverse Oscillation Approach for Estimation of Three-Dimensional Velocity Vectors , Part II : Experimental Validation", *IEEE Transactions on Ultrasonics, Ferroelectrics, and Frequency Control*, vol. 61, no. 10, pp. 1608–1618, 2014.

[135] M. J. Pihl and J. A. Jensen, "A Transverse Oscillation Approach for Estimation of Three-Dimensional Velocity Vectors , Part I : Concept and Simulation Study", *IEEE Transactions on Ultrasonics, Ferroelectrics, and Frequency Control*, vol. 61, no. 10, pp. 1599–1607, 2014.

[136] H. Gao, B. Heyde, and J. D'hooge, "3D Intra-cardiac flow estimation using speckle tracking: A feasibility study in synthetic ultrasound data", in *2013 IEEE International Ultrasonics Symposium (IUS)*, IEEE, Jul. 2013, pp. 68–71. DOI: 10.1109/ULTSYM.2013.0018.

[137] J. Provost, C. Papadacci, *et al.*, "3D ultrafast ultrasound imaging in vivo", *Physics in Medicine and Biology*, vol. 59, no. 19, pp. L1–L13, 2014. DOI: 10.1088/0031-9155/59/19/L1.

[138] C. Chen, Z. Chen, *et al.*, "A Front-End ASIC With Receive Sub-array Beamforming Integrated With a 32 x 32 PZT Matrix Transducer for 3-D Transesophageal Echocardiography", *IEEE Journal of Solid-State Circuits*, pp. 1–13, 2017. DOI: 10.1109/JSSC.2016.2638433.

[139] C. Chen, S. Raghunathan, *et al.*, "A Prototype PZT Matrix Transducer with Low-Power Integrated Receive ASIC for 3D Transesophageal Echocardiography", *IEEE Transactions on Ultrasonics, Ferroelectrics, and Frequency Control*, vol. 3010, no. c, pp. 1–1, 2015. DOI: 10.1109/TUFFC.2015.2496580.

[140] J. A. Jensen, "Field: A Program for Simulating Ultrasound Systems", *Medical and Biological Engineering and Computing*, vol. 34, no. Supplement 1, pp. 351–352, 1996.

[141] J. Jensen, *Field II PW Phantom*, 2012.

[142] M. Frigo and S. G. Johnson, "The design and implementation of FFTW3", *Proceedings of the IEEE*, vol. 93, no. 2, pp. 216–231, 2005. DOI: 10.1109/JPROC.2004.840301.

[143] M. Raffel, C. Willert, and J. Kompenhans, *Particle Image Velocimetry: A Practical Guide*, 2nd ed. 2007. DOI: 10.1007/978-3-540-72308-0.

[144] D. Bera, H. Vos, *et al.*, "Three-dimensional beamforming combining micro-beamformed RF datasets", in *2016 IEEE International Ultrasonics Symposium (IUS)*, 2016, pp. 1–4. DOI: 10.1109/ULTSYM.2016.7728449.

[145] F. Scarano and M. L. Riethmuller, "Advances in iterative multigrid PIV image processing", *Experiments in Fluids*, vol. 29, no. 7, S051–S060, Dec. 2000. DOI: 10.1007/s003480070007.

[146] J. Westerweel, "Fundamentals of digital particle image velocimetry", *Measurement Science and Technology*, vol. 8, no. 12, pp. 1379–1392, 1999. DOI: 10.1088/0957-0233/8/12/002.

[147] B. Heyde, R. Jasaityte, *et al.*, "Elastic image registration versus speckle tracking for 2-d myocardial motion estimation: A direct comparison in vivo", *IEEE Transactions on Medical Imaging*, vol. 32, no. 2, pp. 449–459, 2013. DOI: 10.1109/TMI.2012.2230114.

[148] P. Weinzaepfel, Z. Harchaoui, *et al.*, "DeepFlow : Large displacement optical flow with deep matching", in *ICCV*, 2013, pp. 1385–1392.

[149] H. Saaid, J. Voorneveld, *et al.*, "Tomographic PIV in a model of the left ventricle: 3D flow past biological and mechanical heart valves", *Journal of Biomechanics*, vol. 90, pp. 40–49, Jun. 2019. DOI: 10.1016/j.jbiomech.2019.04.024.

[150] W. Y. Kim, P. G. Walker, *et al.*, "Left ventricular blood flow patterns in normal subjects: A quantitative analysis by three-dimensional magnetic resonance velocity mapping", *Journal of the American College of Cardiology*, vol. 26, no. 1, pp. 224–238, Jul. 1995. DOI: 10.1016/0735-1097(95)00141-L.

[151] J. Bermejo, P. Martínez-Legazpi, and J. C. Del Álamo, "The Clinical Assessment of Intraventricular Flows", *Annual Review of Fluid Mechanics*, vol. 47, no. 1, pp. 315–342, 2015. DOI: 10.1146/annurev-fluid-010814-014728.

[152] M. Belohlavek, "Vortex formation time: an emerging echocardiographic index of left ventricular filling efficiency?", *European Heart Journal - Cardiovascular Imaging*, vol. 13, no. 5, pp. 367–369, May 2012. DOI: 10.1093/ejechocard/jer311.

[153] V. Raghav, S. Sastry, and N. Saikrishnan, "Experimental Assessment of Flow Fields Associated with Heart Valve Prostheses Using Particle Image Velocimetry (PIV): Recommendations for Best Practices", *Cardiovascular Engineering and Technology*, vol. 9, no. 3, pp. 273–287, Sep. 2018. DOI: 10.1007/s13239-018-0348-z.

[154] J. Chikwe, "Prosthesis Type for Aortic- and Mitral-Valve Replacement", *New England Journal of Medicine*, vol. 378, no. 8, pp. 776–779, Feb. 2018. DOI: 10.1056/NEJMc1716336.

[155] A. B. Goldstone, P. Chiu, *et al.*, "Mechanical or Biologic Prostheses for Aortic-Valve and Mitral-Valve Replacement", *New England Journal of Medicine*, vol. 377, no. 19, pp. 1847–1857, Nov. 2017. DOI: 10.1056/NEJMoa1613792.

[156] O. Pierrakos, P. P. Vlachos, and D. P. Telionis, "Time-Resolved DPIV Analysis of Vortex Dynamics in a Left Ventricular Model Through Bileaflet Mechanical and Porcine Heart Valve Prostheses", *Journal of Biomechanical Engineering*, vol. 126, no. 6, p. 714, 2004. DOI: 10.1115/1.1824124.

[157] A. Kheradvar, J. Kasalko, D. Johnson, and M. Gharib, "An in vitro study of changing profile heights in mitral bioprostheses and their influence on flow.", *ASAIO journal (American Society for Artificial Internal Organs : 1992)*, vol. 52, no. 1, pp. 34–38, 2006. DOI: 10.1097/01.mat.0000191203.09932.8c.

[158] G. Querzoli, S. Fortini, and A. Cenedese, "Effect of the prosthetic mitral valve on vortex dynamics and turbulence of the left ventricular flow", *Physics of Fluids*, vol. 22, no. 4, p. 041 901, Apr. 2010. DOI: 10.1063/1.3371720.

[159] A. Falahatpisheh and A. Kheradvar, "High-speed particle image velocimetry to assess cardiac fluid dynamics in vitro: From performance to validation", *European Journal of Mechanics - B/Fluids*, vol. 35, pp. 2–8, Sep. 2012. DOI: 10.1016/j.euromechflu.2012.01.019.

[160] M. Vukićević, S. Fortini, G. Querzoli, S. Espa, and G. Pedrizzetti, "Experimental study of an asymmetric heart valve prototype", *European Journal of Mechanics - B/Fluids*, vol. 35, pp. 54–60, Sep. 2012. DOI: 10.1016/j.euromechflu.2012.01.014.

[161] J. Wang, Q. Gao, R. Wei, and J. Wang, "Experimental study on the effect of an artificial cardiac valve on the left ventricular flow", *Experiments in Fluids*, vol. 58, no. 9, p. 126, Sep. 2017. DOI: 10.1007/s00348-017-2409-8.

[162] S. Fortini, G. Querzoli, S. Espa, and A. Cenedese, "Three-dimensional structure of the flow inside the left ventricle of the human heart", *Experiments in Fluids*, vol. 54, no. 11, p. 1609, Nov. 2013. DOI: 10.1007/s00348-013-1609-0.

[163] A. Falahatpisheh, G. Pedrizzetti, and A. Kheradvar, "Three-dimensional reconstruction of cardiac flows based on multi-planar velocity fields", *Experiments in Fluids*, vol. 55, no. 11, 2014. DOI: 10.1007/s00348-014-1848-8.

[164] S. G.-D. Tan, S. Kim, J. K. F. Hon, and H. L. Leo, "A D-Shaped Bileaflet Bioprosthesis which Replicates Physiological Left Ventricular Flow Patterns", *PLOS ONE*, vol. 11, no. 6, I. Borazjani, Ed., e0156580, Jun. 2016. DOI: 10.1371/journal.pone.0156580.

[165] H. Saaid, P. Segers, M. Novara, T. Claessens, and P. Verdonck, "Single calibration multiplane stereo-PIV: the effect of mitral valve orientation on three-dimensional flow in a left ventricle model", *Experiments in Fluids*, vol. 59, no. 3, p. 49, Mar. 2018. DOI: 10.1007/s00348-018-2504-5.

[166] G. E. Elsinga, F. Scarano, B. Wieneke, and B. W. Van Oudheusden, "Tomographic particle image velocimetry", *Experiments in Fluids*, vol. 41, no. 6, pp. 933–947, 2006. DOI: 10.1007/s00348-006-0212-z.

[167] D. Hasler, A. Landolt, and D. Obrist, "Tomographic PIV behind a prosthetic heart valve", *Experiments in Fluids*, vol. 57, no. 5, p. 80, May 2016. DOI: 10.1007/s00348-016-2158-0.

[168] D. Hasler and D. Obrist, "Three-dimensional flow structures past a bio-prosthetic valve in an in-vitro model of the aortic root.", *PloS one*, vol. 13, no. 3, e0194384, 2018. DOI: 10.1371/journal.pone.0194384.

[169] N. A. Buchmann, C. Atkinson, M. C. Jeremy, and J. Soria, "Tomographic particle image velocimetry investigation of the flow in a modeled human carotid artery bifurcation", *Experiments in Fluids*, vol. 50, no. 4, pp. 1131–1151, Apr. 2011. DOI: 10.1007/s00348-011-1042-1.

[170] C. Roloff, D. Stucht, O. Beuing, and P. Berg, "Comparison of intracranial aneurysm flow quantification techniques: standard PIV vs stereoscopic PIV vs tomographic PIV vs phase-contrast MRI vs CFD", *Journal of NeuroInterventional Surgery*, vol. 11, no. 3, pp. 275–282, Mar. 2019. DOI: 10.1136/neurintsurg-2018-013921.

[171] B. Wieneke, "Volume self-calibration for 3D particle image velocimetry", *Experiments in Fluids*, vol. 45, no. 4, pp. 549–556, Oct. 2008. DOI: 10.1007/s00348-008-0521-5.

[172] F. Scarano, "Tomographic PIV: Principles and practice", *Measurement Science and Technology*, vol. 24, no. 1, 2013. DOI: 10.1088/0957-0233/24/1/012001.

[173] G. Pedrizzetti, F. Domenichini, and G. Tonti, "On the Left Ventricular Vortex Reversal after Mitral Valve Replacement", *Annals of Biomedical Engineering*, vol. 38, no. 3, pp. 769–773, Mar. 2010. DOI: 10.1007/s10439-010-9928-2.

[174] K. Akiyama, N. Nakamura, *et al.*, "Flow-dynamics assessment of mitral-valve surgery by intraoperative vector flow mapping", *Interactive CardioVascular and Thoracic Surgery*, vol. 24, no. 6, pp. 869–875, Jun. 2017. DOI: 10.1093/icvts/ivx033.

[175] K. Nakashima, K. Itatani, *et al.*, "Energy dynamics of the intraventricular vortex after mitral valve surgery", *Heart and Vessels*, vol. 32, no. 9, pp. 1123–1129, Sep. 2017. DOI: 10.1007/s00380-017-0967-6.

[176] A. Cenedese, Z. Del Prete, M. Miozzi, and G. Querzoli, "A laboratory investigation of the flow in the left ventricle of a human heart with prosthetic, tilting-disk valves", *Experiments in Fluids*, vol. 39, no. 2, pp. 322–335, Aug. 2005. DOI: 10.1007/s00348-005-1006-4.

[177] S. S. Khalafvand, J. D. Voorneveld, *et al.*, "Assessment of human left ventricle flow using statistical shape modelling and computational fluid dynamics", *Journal of Biomechanics*, vol. 74, pp. 116–125, 2018. DOI: 10.1016/j.jbiomech.2018.04.030.

[178] J. M. Van Dantzig, B. J. Delemarre, H. Bot, R. W. Koster, and C. A. Visser, "Doppler left ventricular flow pattern versus conventional predictors of left ventricular thrombus after acute myocardial infarction", *Journal of the American College of Cardiology*, vol. 25, no. 6, pp. 1341–1346, May 1995. DOI: 10.1016/0735-1097(94)00548-5.

[179] P. P. Sengupta, R. Burke, B. K. Khandheria, and M. Belohlavek, *Following the Flow in Chambers*, 2008. DOI: 10.1016/j.hfc.2008.02.005.

[180] S. Hendabadi, J. Bermejo, *et al.*, "Topology of blood transport in the human left ventricle by novel processing of doppler echocardiography", *Annals of Biomedical Engineering*, vol. 41, no. 12, pp. 2603–2616, 2013. DOI: 10.1007/s10439-013-0853-z.

[181] J. Jeong and F. Hussain, "On the identification of a vortex", *Journal of Fluid Mechanics*, vol. 285, no. -1, p. 69, Feb. 1995. DOI: 10.1017/S0022112095000462.

[182] D. R. Troolin and E. K. Longmire, "Volumetric velocity measurements of vortex rings from inclined exits", *Experiments in Fluids*, vol. 48, no. 3, pp. 409–420, Mar. 2010. DOI: 10.1007/s00348-009-0745-z.

[183] H. Watanabe, S. Sugiura, and T. Hisada, "The looped heart does not save energy by maintaining the momentum of blood flowing in the ventricle", *American Journal of Physiology-Heart and Circulatory Physiology*, vol. 294, no. 5, H2191–H2196, May 2008. DOI: 10.1152/ajpheart.00041.2008.

[184] N. L'Heureux, N. Dusserre, A. Marini, S. Garrido, L. de la Fuente, and T. McAllister, "Technology insight: the evolution of tissue-engineered vascular grafts–from research to clinical practice.", *Nature clinical practice. Cardiovascular medicine*, vol. 4, no. 7, pp. 389–95, Jul. 2007. DOI: 10.1038/ncpcardio0930.

[185] S. S. Khalafvand, F. Xu, J. Westenberg, F. Gijsen, and S. Kenjeres, "Intraventricular blood flow with a fully dynamic mitral valve model", *Computers in Biology and Medicine*, vol. 104, no. September 2018, pp. 197–204, Jan. 2019. DOI: 10.1016/j.compbiomed.2018.11.024.

[186] M. S. M. Elbaz, E. E. Calkoen, J. J. M. Westenberg, B. P. F. Lelieveldt, A. A. W. Roest, and R. J. van der Geest, "Vortex flow during early and late left ventricular filling in normal subjects: quantitative characterization using retrospectively-gated 4D flow cardiovascular magnetic resonance and three-dimensional vortex core analysis", *Journal of Cardiovascular Magnetic Resonance*, vol. 16, no. 1, p. 78, Dec. 2014. DOI: 10.1186/s12968-014-0078-9.

[187] V. Meschini, M. D. de Tullio, G. Querzoli, and R. Verzicco, "Flow structure in healthy and pathological left ventricles with natural and prosthetic mitral valves", *Journal of Fluid Mechanics*, vol. 834, pp. 271–307, Jan. 2018. DOI: 10.1017/jfm.2017.725.

[188] D. Schanz, S. Gesemann, and A. Schröder, "Shake-The-Box: Lagrangian particle tracking at high particle image densities", *Experiments in Fluids*, vol. 57, no. 5, p. 70, May 2016. DOI: 10.1007/s00348-016-2157-1.

[189] G. Pedrizzetti, A. R. Martiniello, V. Bianchi, A. D'Onofrio, P. Caso, and G. Tonti, "Cardiac fluid dynamics anticipates heart adaptation", *Journal of Biomechanics*, vol. 48, no. 2, pp. 388–391, 2015. DOI: 10.1016/j.jbiomech.2014.11.049.

[190] P. Dyverfeldt, M. Bissell, *et al.*, "4D flow cardiovascular magnetic resonance consensus statement", *Journal of Cardiovascular Magnetic Resonance*, vol. 17, no. 1, pp. 1–19, 2015. DOI: 10.1186/s12968-015-0174-5.

[191] M. Correia, J. Provost, M. Tanter, and M. Pernot, "4D ultrafast ultrasound flow imaging: in vivo quantification of arterial volumetric flow rate in a single heartbeat", *Physics in Medicine and Biology*, vol. 61, no. 23, pp. L48–L61, 2016. DOI: 10.1088/0031-9155/61/23/L48.

[192] S. Holbek, C. Ewertsen, *et al.*, "Ultrasonic 3-D Vector Flow Method for Quantitative In Vivo Peak Velocity and Flow Rate Estimation", *IEEE Transactions on Ultrasonics, Ferroelectrics, and Frequency Control*, vol. 64, no. 3, pp. 544–554, 2017. DOI: 10.1109/TUFFC.2016.2639318.

[193] S. Holbek, K. L. Hansen, *et al.*, "Common Carotid Artery Flow Measured by 3-D Ultrasonic Vector Flow Imaging and Validated with Magnetic Resonance Imaging", *Ultrasound in Medicine & Biology*, vol. 43, no. 10, pp. 2213–2220, Oct. 2017. DOI: 10.1016/j.ultrasmedbio.2017.06.007.

[194] K. C. Assi, E. Gay, *et al.*, "Intraventricular vector flow mapping - A Doppler-based regularized problem with automatic model selection", *Physics in Medicine and Biology*, vol. 62, no. 17, pp. 7131–7147, 2017. DOI: 10.1088/1361-6560/aa7fe7.

[195] A. Gomez, A. De Vecchi, *et al.*, "4D Blood Flow Reconstruction over the Entire Ventricle from Wall Motion and Blood Velocity Derived from Ultrasound Data", *IEEE Transactions on Medical Imaging*, vol. 0062, no. c, pp. 1–1, 2015. DOI: 10.1109/TMI.2015.2428932.

[196] T. Grønli, M. Wigen, P. Segers, and L. Lovstakken, "A fast 4D B-spline framework for model-based reconstruction and regularization in vector flow imaging", *IEEE International Ultrasonics Symposium, IUS*, vol. 1, no. 1, pp. 2–5, 2018.

[197] M. S. Wigen, S. Fadnes, *et al.*, "4D Intracardiac Ultrasound Vector Flow Imaging -Feasibility and Comparison to Phase-Contrast MRI", *IEEE Transactions on Medical Imaging*, no. c, 2018. DOI: 10.1109/TMI.2018.2844552.

[198] D. Bera, F. van den Adel, *et al.*, "Fast Volumetric Imaging Using a Matrix Transesophageal Echocardiography Probe with Partitioned Transmit–Receive Array", *Ultrasound in Medicine and Biology*, vol. 44, no. 9, pp. 2025–2042, 2018. DOI: 10.1016/j.ultrasmedbio.2018.05.017.

[199] J. Ahrens, B. Geveci, and C. Law, "ParaView: An End-User Tool for Large-Data Visualization", in *Visualization Handbook*, January 2005, Elsevier, 2005, pp. 717–731. DOI: 10.1016/B978-012387582-2/50038-1. arXiv: arXiv:1301.7609v1.

[200] S. G. Foster, P. M. Embree, and W. D. O'Brien, "Flow Velocity Profile via Time-Domain Correlation: Error Analysis and Computer Simulation", *IEEE Transactions on Ultrasonics, Ferroelectrics, and Frequency Control*, vol. 37, no. 3, pp. 164–175, 1990. DOI: 10.1109/58.55306.

[201] I. K. Ekroll, M. Wigen, S. Fadnes, and J. Adval, "Quantitative vascular blood flow imaging : A comparison of vector velocity estimation schemes", in *IEEE International Ultrasonics Symposium (IUS)*, 2018, pp. 1–4.

[202] A. M. S. Omar, S. Vallabhajosyula, and P. P. Sengupta, "Left Ventricular Twist and Torsion", *Circulation: Cardiovascular Imaging*, vol. 8, no. 6, pp. 74–82, Jun. 2015. DOI: 10.1161/CIRCIMAGING.115.003029.

[203] C. A. V. Hoyos, M. B. Stuart, K. L. Hansen, M. B. Nielsen, and J. A. Jensen, "Accurate Angle Estimator for High-Frame-Rate 2-D Vector Flow Imaging", *IEEE Transactions on Ultrasonics, Ferroelectrics, and Frequency Control*, vol. 63, no. 6, pp. 842–853, 2016. DOI: 10.1109/TUFFC.2016.2551689.

[204] M. Wigen and L. Lovstakken, "In vivo three-dimensional intra-cardiac vector flow imaging using a 2D matrix array transducer", *IEEE International Ultrasonics Symposium, IUS*, vol. 2016-Novem, pp. 2–5, 2016. DOI: 10.1109/ULTSYM.2016.7728690.

[205] H. Takahashi, H. Hasegawa, and H. Kanai, "Echo motion imaging with adaptive clutter filter for assessment of cardiac blood flow", *Japanese Journal of Applied Physics*, vol. 54, no. 7S1, 07HF09, Jul. 2015. DOI: 10.7567/JJAP.54.07HF09.

[206] M. Toulemonde, Y. Li, *et al.*, "High-Frame-Rate Contrast Echocardiography using diverging waves: initial in-vitro and in-vivo evaluation", *IEEE Transactions on Ultrasonics, Ferroelectrics, and Frequency Control*, pp. 1–1, 2018. DOI: 10.1109/TUFFC.2018.2856756.

[207] R. Rau, W. Scheffer, *et al.*, "3D functional ultrasound imaging of the visual system in the pigeon brain", in *2017 IEEE International Ultrasonics Symposium (IUS)*, IEEE, Sep. 2017, pp. 1–1. DOI: 10.1109/ULTSYM.2017.8092831.

[208] N. Halko, P.-G. Martinsson, and J. A. Tropp, "Finding structure with randomness: Probabilistic algorithms for constructing approximate matrix decompositions", *SIAM review*, vol. 53, no. 2, pp. 217–288, Sep. 2011. arXiv: 0909.4061.

[209] H. Becher and R. Olszewski, "Current Indications for Contrast Echocardiography", *European Cardiology Review*, vol. 3, no. 2, p. 44, 2007. DOI: 10.15420/ecr.2007.0.2.44.

[210] E. Picano and P. a. Pellikka, "Stress echo applications beyond coronary artery disease.", *European heart journal*, vol. 35, no. 16, pp. 1033–40, 2014. DOI: 10.1093/eurheartj/eht350.

[211] T. Roesgen, "Optimal subpixel interpolation in particle image velocimetry", *Experiments in Fluids*, vol. 35, no. 3, pp. 252–256, 2003. DOI: 10.1007/s00348-003-0627-8.

[212] R. Hall, A. Budaj, *et al.*, "Guidelines on the management of valvular heart disease: The Task Force on the Management of Valvular Heart Disease of the European Society of Cardiology", *European Heart Journal*, vol. 28, no. 2, pp. 230–268, 2007. DOI: 10.1093/eurheartj/ehl428. arXiv: NIHMS150003.

[213] R. Z. Azar, O. Goksel, and S. E. Salcudean, "Sub-sample displacement estimation from digitized ultrasound RF signals using multi-dimensional polynomial fitting of the cross-correlation function", *IEEE Transactions on Ultrasonics, Ferroelectrics and Frequency Control*, vol. 57, no. 11, pp. 2403–2420, Nov. 2010. DOI: 10.1109/TUFFC.2010.1708.

[214] A. E. Saris, M. M. Nillesen, S. Fekkes, H. H. Hansen, and C. L. de Korte, "Robust blood velocity estimation using point-spread-function-based beamforming and multi-step speckle tracking", in *2015 IEEE International Ultrasonics Symposium (IUS)*, IEEE, Oct. 2015, pp. 1–4. DOI: 10.1109/ULTSYM.2015.0421.

[215] O. Couture, S. Bannouf, G. Montaldo, J. F. Aubry, M. Fink, and M. Tanter, "Ultrafast Imaging of Ultrasound Contrast Agents", *Ultrasound in Medicine and Biology*, vol. 35, no. 11, pp. 1908–1916, 2009. DOI: 10.1016/j.ultrasmedbio.2009.05.020.

[216] I. K. Ekroll, M. M. Voormolen, O. K. V. Standal, J. M. Rau, and L. Lovstakken, "Coherent compounding in doppler imaging", *IEEE Transactions on Ultrasonics, Ferroelectrics, and Frequency Control*, vol. 62, no. 9, pp. 1634–1643, 2015. DOI: 10.1109/TUFFC.2015.007010.

[217] L. Nie, D. M. J. Cowell, T. M. Carpenter, J. R. McLaughlan, A. A. Cubukcu, and S. Freear, "High Frame-Rate Contrast-Enhanced Echocardiography using Diverging Waves: 2-D Motion Estimation and Compensation", *IEEE Transactions on Ultrasonics, Ferroelectrics, and Frequency Control*, no. December, pp. 1–1, 2018. DOI: 10.1109/TUFFC.2018.2887224.

[218] J. Poree, D. Posada, A. Hodzic, F. Tournoux, G. Cloutier, and D. Garcia, "High-Frame-Rate Echocardiography Using Coherent Compounding with Doppler-Based Motion-Compensation", *IEEE Transactions on Medical Imaging*, vol. 35, no. 7, pp. 1647–1657, 2016. DOI: 10.1109/TMI.2016.2523346.

[219] A. Stanziola, M. Toulemonde, *et al.*, "Benefits of Adaptive Beamforming Methods for Contrast Enhanced High Frame-Rate Ultrasound", in *2018 IEEE International Ultrasonics Symposium (IUS)*, IEEE, Oct. 2018, pp. 1–4. DOI: 10.1109/ULTSYM.2018.8579906.

[220] A. Stanziola, M. Toulemonde, *et al.*, "Motion Artifacts and Correction in Multi-Pulse High Frame Rate Contrast Enhanced Ultrasound", *IEEE Transactions on Ultrasonics, Ferroelectrics, and Frequency Control*, pp. 1–1, 2018. DOI: 10.1109/TUFFC.2018.2887164.

[221] K. Diamantis, T. Anderson, M. B. Butler, C. A. Villagomez-Hoyos, J. A. Jensen, and V. Sboros, "Resolving Ultrasound Contrast Microbubbles Using Minimum Variance Beamforming", *IEEE Transactions on Medical Imaging*, vol. 38, no. 1, pp. 194–204, Jan. 2019. DOI: 10.1109/TMI.2018.2859262.

[222] D. Hyun, L. Abou-Elkacem, V. A. Perez, S. M. Chowdhury, J. K. Willmann, and J. J. Dahl, "Improved Sensitivity in Ultrasound Molecular Imaging With Coherence-Based Beamforming", *IEEE Transactions on Medical Imaging*, vol. 37, no. 1, pp. 241–250, Jan. 2018. DOI: 10.1109/TMI.2017.2774814.

[223] H. Taki, K. Taki, *et al.*, "High range resolution ultrasonographic vascular imaging using frequency domain interferometry with the capon method", *IEEE Transactions on Medical Imaging*, vol. 31, no. 2, pp. 417–429, 2012. DOI: 10.1109/TMI.2011.2170847.

[224] M. A. Hussain, S. K. Alam, S. Y. Lee, and M. K. Hasan, "Robust Strain-Estimation Algorithm Using Combined Radiofrequency and Envelope Cross-Correlation with Diffusion Filtering", *Ultrasonic Imaging*, vol. 34, no. 2, pp. 93–109, Apr. 2012. DOI: 10.1177/016173461203400203.

[225] J. Baranger, B. Arnal, F. Perren, O. Baud, M. Tanter, and C. Demene, "Adaptive spatiotemporal SVD clutter filtering for Ultrafast Doppler Imaging using similarity of spatial singular vectors", *IEEE Transactions on Medical Imaging*, vol. 0062, no. c, 2018. DOI: 10.1109/TMI.2018.2789499.

[226] L. Løvstakken, S. Bjærum, K. Kristoffersen, R. Haaverstad, and H. Torp, "Real-time adaptive clutter rejection filtering in color flow imaging using power method iterations", *IEEE Transactions on Ultrasonics, Ferroelectrics, and Frequency Control*, vol. 53, no. 9, pp. 1597–1608, 2006. DOI: 10.1109/TUFFC.2006.1678188.

[227] T. Segers, P. Kruizinga, M. P. Kok, G. Lajoinie, N. de Jong, and M. Versluis, "Monodisperse Versus Polydisperse Ultrasound Contrast Agents: Non-Linear Response, Sensitivity, and Deep Tissue Imaging Potential", *Ultrasound in Medicine & Biology*, vol. 44, no. 7, pp. 1482–1492, Jul. 2018. DOI: 10.1016/j.ultrasmedbio.2018.03.019. arXiv: arXiv:1806.04379v1.

[228] P. Santos, G. U. Haugen, L. Lovstakken, E. Samset, and J. D'Hooge, "Diverging Wave Volumetric Imaging Using Subaperture Beamforming", *IEEE Transactions on Ultrasonics, Ferroelectrics, and Frequency Control*, vol. 63, no. 12, pp. 2114–2124, 2016. DOI: 10.1109/TUFFC.2016.2616172.

[229] F. Seemann, P. Arvidsson, *et al.*, "Noninvasive Quantification of Pressure-Volume Loops From Brachial Pressure and Cardiovascular Magnetic Resonance", *Circulation: Cardiovascular Imaging*, vol. 12, no. 1, e008493, Dec. 2019. DOI: 10.1161/CIRCIMAGING.118.008493.

[230] I. Z. Apostolakis, P. Nauleau, C. Papadacci, M. D. McGarry, and E. E. Konofagou, "Feasibility and Validation of 4-D Pulse Wave Imaging in Phantoms and In Vivo", *IEEE Transactions on Ultrasonics, Ferroelectrics, and Frequency Control*, vol. 64, no. 9, pp. 1305–1317, 2017. DOI: 10.1109/TUFFC.2017.2735381.

[231] A. Caenen, D. Shcherbakova, *et al.*, "Myocardial stiffness assessment in pediatric cardiology using shear wave imaging", in *2015 IEEE International Ultrasonics Symposium (IUS)*, IEEE, Oct. 2015, pp. 1–4. DOI: 10.1109/ULTSYM.2015.0222.

[232] S. Fiorentini, L. M. Saxhaug, T. G. Bjastad, E. Holte, H. Torp, and J. Avdal, "Maximum Velocity Estimation in Coronary Arteries Using 3-D Tracking Doppler", *IEEE Transactions on Ultrasonics, Ferroelectrics, and Frequency Control*, vol. 65, no. 7, pp. 1102–1110, Jul. 2018. DOI: 10.1109/TUFFC.2018.2827241.

[233] D. Maresca, M. Correia, *et al.*, "Noninvasive Imaging of the Coronary Vasculature Using Ultrafast Ultrasound", *JACC: Cardiovascular Imaging*, vol. 11, no. 6, pp. 1–11, Jun. 2017. DOI: 10.1016/j.jcmg.2017.05.021.

SUMMARY

Diseases of the cardiovascular system are a significant burden on society, being the highest cause of death worldwide. Early diagnosis of many cardiovascular diseases offers the potential for more effective treatment and better outcome. Blood flow patterns are influenced by the morphology and function of the heart and vascular system, potentially offering early stage signals of dysfunction. However, current methods of blood flow quantification are limited in frame rate or dimensionality or the estimated flow components. This thesis aimed to address these problems by using high frame rate (HFR) ultrasound and echo-particle image velocimetry (echoPIV).

In this thesis we have developed and tested HFR echoPIV in 2D from the bench to bedside, in both the left ventricle and abdominal aorta. In 3D we have developed and tested HFR echoPIV using two different matrix transducers in silico and in vitro.

First, in **Chapter 2**, a simple parabolic flow phantom was used to verify that 2D HFR echoPIV could accurately measure the high velocity flows that are expected in the abdominal aorta (during systole) and the LV (during filling and ejection). Additionally we found that the velocity magnitude bias increased with depth, due to elevational plane thickness which caused averaging over the parabolic flow profile. We then showed that using ultrasound contrast agent (UCA) microbubbles improved accuracy over native blood speckle at greater depths.

We then assessed the feasibility and accuracy of 2D HFR echoPIV in the abdominal aorta in healthy volunteers (**Chapter 3 & 4**). In **Chapter 3**, we searched for an optimum microbubble concentration, acoustic pressure and clutter suppression strategy. We found that using singular value decomposition suppressed tissue clutter better than amplitude modulation, and that very low acoustic pressures should be used to prevent microbubble destruction when using HFR imaging sequences. We found that higher microbubble concentrations provided higher signal levels during diastole, when more bubble destruction would occur. Additionally, a higher microbubble concentration accompanied higher cross-correlation values during low flow rates and vice versa. We then compared 2D HFR echoPIV with phase contrast magnetic resonance imaging and found good agreement (**Chapter 4**).

In **Chapter 5 & 6**, we determined if 2D HFR echoPIV could estimate the complex, high velocity flow patterns in the left ventricle. First, in **Chapter 5**, we developed a dynamic left ventricular phantom with a realistic geometry to facilitate comparison between HFR echoPIV and time-resolved optical PIV. We found that HFR echoPIV could measure the high velocity trans-mitral jet and other high energy flow patterns. Then, in **Chapter 6**, we demonstrated that 2D HFR echoPIV could also measure the trans-mitral

jet in a patient, using pulsed wave Doppler as a reference for the velocity magnitudes.

Chapters 7-9 shift focus to 3D flow estimation. We started in silico using a pediatric transesophageal matrix transducer with micro-beamforming architecture to image a simulated arterial flow phantom (**Chapter 7**). We found that during periods with high velocity gradients 4D echoPIV greatly underestimated the velocity magnitudes. We attributed the underestimation to the larger lateral point-spread-function of the imaging system relative to the flow gradients being studied.

Wanting to perform experiments with a prototype adult transesophageal matrix transducer, we then developed a new left ventricle phantom capable of being imaged with a 3D optical velocimetry technique (tomographic PIV). In **Chapter 8** we then tested the effect that different prosthetic valves have on intraventricular flow patterns using the setup. We found that biological prosthetic valves allowed for higher kinetic energies and much higher velocities than the mechanical valves tested. The biological valve facilitated a trans-mitral jet that penetrated further into the left ventricle than the mechanical valves, potentially having consequences for blood stasis and thrombus formation. All of the valves tested, except for the tilting-disc valve, resulted in a cross-flow path, where the outflow path crossed in the inflow path. In **Chapter 9** we compared 4D echoPIV against tomographic PIV using the same left ventricular phantom. A HFR imaging sequence was described, capable of achieving 1000 volumes per second over a 60° x 60° field of view, using only 4 gated heartbeats. Tomographic PIV and 4D echoPIV estimated similar flow patterns in the phantom, but the accuracy of 4D echoPIV deteriorated with depth, which was attributed to the increasing lateral point-spread-function over depth.

Chapter 10 then discusses the challenges and future perspectives for clinical translation of 2D HFR echoPIV and further development of 4D echoPIV.

SAMENVATTING

Hart- en vaatziekten zijn de belangrijkste doodsoorzaak wereldwijd en vormen daarom een grote last voor de maatschappij. Het vroegtijdig detecteren van veel hart- en vaatziekten biedt mogelijkheden tot effectievere behandelingen en dus betere uitkomsten. Bloedstromingspatronen worden beïnvloed door de morfologie en het functioneren van het hart- en vaatstelsel, en zijn daarom mogelijk een vroegtijdige biomarker voor stoornissen.De huidige methodes voor het kwantificeren van bloedstromingen zijn echter alleen toegepast op lage frame rates, in een gelimiteerd aantal dimensies, en/of schatten niet alle stromingscomponenten. In dit proefschrift worden deze tekortkomingen aangepakt door gebruik te maken van ultrageluid met hoge frame rates (HFR) en echoparticle image velocimetry (echoPIV).

Dit proefschrift beschrijft het ontwikkelen en testen van 2D HFR echoPIV voor de linker hartkamer en de abdominale aorta, vanaf het lab tot aan de kliniek. We hebben HFR echoPIV ook ontwikkeld in 3D en getest in silico en in vitro met behulp van twee matrix probes.

Ten eerste laat **Hoofdstuk 2** met behulp van een eenvoudig fantoom met parabolisch stromingsprofiel zien dat 2D HFR echoPIV hoge stroomsnelheden accuraat kan meten. Dergelijke stromingen met hoge snelheid worden verwacht in de abdominale aorta tijdens systole en in de linker hartkamer tijdens het vullen en legen van het hart. Bovendien vonden we een systematische afwijking in de geschatte snelheden die toenam met diepte. Immers, de breedte van de uitgezonden bundel in de elevatie-richting neemt toe met de diepte, wat zorgt voor meer middeling over het parabolische stromingsprofiel. Vervolgens laten we zien dat de precisie op grotere diepte verbetert door gebruik te maken van ultrasound contrast agent (UCA) microbellen.

Vervolgens hebben we de haalbaarheid en precisie van 2D HFR echoPIV in de abdominale aorta getest in gezonde vrijwilligers **(Hoofdstuk 3 & 4)**. In **Hoofdstuk 3** gaan we op zoek naar de optimale microbellen concentratie, de optimale akoestische druk en de beste strategie om clutter te onderdrukken. We vonden dat clutter beter onderdrukt wordt door singuliere-waardenontbinding (SVD) dan door amplitude modulatie, en dat lage akoestische drukken nodig zijn om de vernietiging van microbellen door HFR beeldvormingssequenties te voorkomen. We zagen dat hogere concentraties van microbellen een hoger signaalniveau opleveren tijdens diastole, wanneer meer microbellen worden vernietigd. Bovendien zorgde een hogere microbellen-concentratie voor een hogere kruiscorrelatiewaarde bij lage stroomsnelheden, en andersom. **Hoofdstuk 4** vergelijkt 2D HFR echoPIV en phase contrast MRI. We vonden een sterke overeenkomst in resultaten.

In **Hoofdstuk 5 & 6** onderzoeken we of 2D HFR echoPIV gebruikt kan worden voor het kwantificeren van de complexe hoge-snelheidsstromingspatronen in de linker hartkamer. Ten eerste beschrijft **Hoofdstuk 5** een dynamisch linker-ventrikelfantoom met een realistische geometrie. Dit fantoom hebben we gebruikt om HFR echoPIV te vergelijken met tijdsgeresolveerde optische PIV. We zagen dat HFR echoPIV de snelle stroming door de mitraalklep en andere hoog-energetische stromingspatronen kon meten. Ten tweede wordt in **Hoofdstuk 6** 2D HFR echoPIV gebruikt om de trans-mitrale stroming in een patiënt te meten. Pulsed wave Doppler is hierbij gebruikt als standaard.

Hoofdstuk 7-9 gaan over het schatten van stromingspatronen in 3D. We beginnen in silico in **Hoofdstuk 7**. We hebben het scannen van een arterieel flowfantoom gesimuleerd op basis van een pediatrische transoesofagale matrix probe met een microbeamforming architectuur. We vonden dat 4D echoPIV de snelheden sterk onderschat tijdens periodes met hoge snelheidsgradiënten. We denken dat deze onderschatting komt door de grote punt-spreidings-functie in verhouding met de schaal van de snelheidsgradiënten.

Vervolgens wilden we de experimenten uitvoeren met een prototype voor een transoesofagale matrix probe voor volwassenen. Daartoe hebben we een nieuw linker-ventrikelfantoom ontwikkeld dat gebruikt kan worden voor 3D optische velocimetry technieken (tomographic PIV). Met behulp van dit fantoom hebben we het effect van verschillende kunstkleppen op de intraventriculaire flowpatronen getest (**Hoofdstuk 8**). We zagen hogere kinetische energieën en veel hogere snelheden voor de biologische kunstkleppen dan voor de geteste mechanische kleppen. De biologische kleppen zorgden voor een transmitrale stroming die dieper in de linker ventrikel doordrong dan wanneer mechanische kleppen werden gebruikt. Dit heeft mogelijk als consequentie dat de bloedstroming stagneert, met thrombusvorming als vervolg. Alle geteste kleppen, behalve de tilting-disc klep, zorgden voor een kruisend stromingspad, waarbij het uitstroompad snijdt met het instroompad. In **Hoofdstuk 9** gebruiken we hetzelfde fantoom om 4D echoPIV met tomografische PIV te vergelijken. We hebben een HFR beeldvormingssequentie ontwikkeld die in staat is om 1000 volumes per seconde op te nemen over een 60° x 60° beeldveld, door slechts gebruik te maken van 4 hartcycli. We vonden vergelijkbare flowpatronen in het fantoom met tomografische PIV en 4D echoPIV. De precisie van 4D echoPIV nam echter af met de diepte, vanwege de eveneens met de diepte toenemende laterale punt-spreidings-functie.

Hoofdstuk 10 tenslotte bediscussieert de uitdagingen en perspectieven voor de toekomst gerelateerd aan de klinische translatie van 2D HFR echoPIV en aan het verder ontwikkelen van 4D echoPIV.

LIST OF PUBLICATIONS

PEER-REVIEWED PAPERS

T. van Rooij, I. Skachkov, I. Beekers, K. R. Lattwein, **J.D. Voorneveld**, T. J. Kokhuis, D. Bera, Y. Luan, A. F. van der Steen, N. de Jong, and K. Kooiman, "Viability of endothelial cells after ultrasound-mediated sonoporation: Influence of targeting, oscillation, and displacement of microbubbles", *Journal of Controlled Release*, vol. 238, pp. 197–211, 2016. DOI: 10.1016/j.jconrel.2016.07.037.

J. Voorneveld, A. Muralidharan, T. Hope, H. J. Vos, P. Kruizinga, A. F. W. van der Steen, F. J. H. Gijsen, S. Kenjeres, N. de Jong, and J. G. Bosch, "High Frame Rate Ultrasound Particle Image Velocimetry for Estimating High Velocity Flow Patterns in the Left Ventricle", *IEEE Transactions on Ultrasonics, Ferroelectrics, and Frequency Control*, vol. 65, no. 12, pp. 2222–2232, 2017. DOI: 10.1109/TUFFC.2017.2786340.

S. S. Khalafvand, **J.D. Voorneveld**, A. Muralidharan, F. J. Gijsen, J. G. Bosch, T. van Walsum, A. Haak, N. de Jong, and S. Kenjeres, "Assessment of human left ventricle flow using statistical shape modelling and computational fluid dynamics", *Journal of Biomechanics*, vol. 74, pp. 116–125, 2018. DOI: 10.1016/j.jbiomech.2018.04.030.

S. A. Engelhard, **J. Voorneveld**, H. J. Vos, J. J. M. Westenberg, F. J. H. Gijsen, P. Taimr, M. Versluis, N. de Jong, J. G. Bosch, M. M. P. J. Reijnen, and E. Groot Jebbink, "High-Frame-Rate, Contrast-enhanced Ultrasound Particle Image Velocimetry in the Abdominal Aorta: first human results", *Radiology*, vol. 289, no. 1, pp. 119–125, Jul. 2018. DOI: 10.1148/radiol.2018172979.

J. Voorneveld, S. Engelhard, H. J. Vos, M. M. J. Reijnen, F. Gijsen, M. Versluis, E. G. Jebbink, N. de Jong, and J. G. Bosch, "High Frame Rate Contrast-Enhanced Ultrasound for Velocimetry in the Human Abdominal Aorta", *IEEE Transactions on Ultrasonics, Ferroelectrics, and Frequency Control*, vol. 65, no. 12, pp. 2245–2254, 2018. DOI: 10.1109/TUFFC.2018.2846416.

J. Voorneveld, L. B. Keijzer, M. Strachinaru, D. J. Bowen, J. S. Goei, F. Ten Cate, A. F. van der Steen, N. de Jong, H. J. Vos, A. E. van den Bosch, and J. G. Bosch, "High-Frame-Rate Echo-Particle Image Velocimetry Can Measure the High-Velocity Diastolic Flow Patterns", *Circulation: Cardiovascular Imaging*, vol. 12, no. 4, Apr. 2019. DOI: 10.1161/CIRCIMAGING.119.008856.

H. Saaid, **J. Voorneveld**, C. Schinkel, J. Westenberg, F. Gijsen, P. Segers, P. Verdonck, N. de Jong, J. G. Bosch, S. Kenjeres, and T. Claessens, "Tomographic PIV in a model of the left ventricle: 3D flow past biological and mechanical heart valves", *Journal of Biomechanics*, vol. 90, pp. 40–49, Jun. 2019. DOI: 10.1016/j.jbiomech.2019.04.024.

SUBMITTED PAPERS

J. Voorneveld, H. Saaid, C. Schinkel, N. Radeljic-Jakic, B. Lippe, F. J. Gijsen, A. F. van der Steen, N. de Jong, T. Claessens, H. J. Vos, S. Kenjeres, and J. G. Bosch, "4D Echo-Particle Image Velocimetry in a Left Ventricular Phantom",

CONFERENCE PROCEEDINGS

J. Voorneveld, P. Kruizinga, H. J. Vos, F. J. Gijsen, E. G. Jebbink, A. F. van der Steen, N. de Jong, and J. G. Bosch, "Native blood speckle vs ultrasound contrast agent for particle image velocimetry with ultrafast ultrasound - in vitro experiments", in *2016 IEEE International Ultrasonics Symposium (IUS)*, IEEE, Sep. 2016, pp. 1–4. DOI: 10.1109/ULTSYM.2016.7728614.

E. Bodnariuc, S. Petra, C. Schnörr, and **J. Voorneveld**, "A Local Spatio-Temporal Approach to Plane Wave Ultrasound Particle Image Velocimetry", in *Lecture Notes in Computer Science (including subseries Lecture Notes in Artificial Intelligence and Lecture Notes in Bioinformatics)*, vol. 10496 LNCS, 2017, pp. 138–149. DOI: 10.1007/978-3-319-66709-6_12.

J.D. Voorneveld, D. Bera, A. F. van der Steen, N. de Jong, and J. G. Bosch, "Particle image velocimetry on simulated 3D ultrafast ultrasound from pediatric matrix TEE transducers", in *Proc. SPIE, Medical Imaging 2017*, vol. 10139, 2017, pp. 1–9. DOI: 10.1117/12.2254436.

A. M. Hoving, **J. Voorneveld**, E. E. de Vries, E. Groot Jebbink, J. Mikhal, M. Versluis, J. G. Bosch, N. de Jong, G. J. de Borst, and C. H. Slump, "In vitro high-frame-rate contrast-enhanced ultrasound particle image velocimetry in a carotid artery stent", in *Medical Imaging 2018: Ultrasonic Imaging and Tomography*, N. Duric and B. C. Byram, Eds., SPIE, Mar. 2018, p. 5. DOI: 10.1117/12.2293669.

F. Khellaf, S. Leclerc, **J.D. Voorneveld**, R. S. Bandaru, J. G. Bosch, and O. Bernard, "Left ventricle segmentation in 3D ultrasound by combining structured random forests with active shape models", in *Medical Imaging 2018: Image Processing*, E. D. Angelini and B. A. Landman, Eds., SPIE, Mar. 2018, p. 18. DOI: 10.1117/12.2293544.

CURRICULUM VITÆ

Jason Dirk Voorneveld was born on the 19th of January 1987 in Johannesburg, South Africa. Upon completing secondary school in Johannesburg he relocated to Cape Town where he completed his BSc in Electro-Mechanical Engineering in 2009 at the University of Cape Town, finishing top of his class in 2008 and 2009. He then spent time in industry working as a maintenance/project engineer at Indigo Brands in Cape Town until 2013. In 2013 he returned to the University of Cape Town where he obtained his MSc in Biomedical Engineering developing small diameter vascular grafts. During his Masters study he was also accepted for a 2-month internship at DKFZ (German Cancer Research Center) in Heidelberg, Germany where he developd automated drosophila melanogaster counting software for Alzheimer's disease research. He completed his MSc with distinction in 2015 and, shortly after, joined the Department of Biomedical Engineering at Erasmus MC Medical Center Rotterdam, where he completed the work that led to this thesis.

He is currently working as a post-doctoral researcher at Erasmus MC, continuing his research in 4D ultrasound based velocimetry techniques for cardiovascular flow quantification.

PHD PORTFOLIO

PhD Training	Year	ECTS
International Conferences		
Conference on Functional Imaging and Modelling of the Heart, Maastricht, Netherlands	2015	0.9
IEEE International Ultrasonics Symposium (Poster), Tours, France	2016	1.4
22nd European Symposium on Ultrasound Contrast Imaging (Poster), Rotterdam, Netherlands	2017	1.1
SPIE Medical Imaging (Oral), Florida, USA	2017	2.2
Artimino (Oral), Artimino, Italy	2017	2.2
IEEE International Ultrasonics Symposium (Oral), Washington D.C., USA	2017	1.9
23rd European Symposium on Ultrasound Contrast Imaging (Oral), Rotterdam, Netherlands	2018	1.6
IEEE International Ultrasonics Symposium (Oral), Kobe, Japan	2018	1.9
24th European Symposium on Ultrasound Contrast Imaging (Oral+Poster), Rotterdam, Netherlands	2019	2.1
7th Dutch Bio-medical Engineering Conference (Poster), Egmond aan Zee, Netherlands	2019	1.1
Courses		
COEUR: Heart Failure Research	2016	1.5
Medical Imaging Summer School	2016	1.4
Ultrafast ultrasound imaging: Basic Principles and Applications (IEEE IUS)	2016	0.15
Ultrasound Vector Velocity Imaging (IEEE IUS)	2016	0.15
High-Performance Computing for Medical Imaging on Programmable Graphics Hardware (SPIE)	2017	0.15
COEUR: Cardiovascular Imaging and Diagnostics	2017	0.5
Basic Training Ultrasound	2017	0.9
English Biomedical Writing and Communication	2017	3
Research Integrity	2018	0.3

PhD Training	Year	ECTS
Research Symposia and Seminars		
Dutch Society for Medical Ultrasound Autumn Meeting, Leuven, Belgium	2015	0.15
Dutch Society for Medical Ultrasound Spring Meeting (Oral), Rotterdam, Netherlands	2016	1.15
Dutch Society for Medical Ultrasound Autumn Meeting, Nijmegen, Netherlands	2016	0.15
Dutch Society for Medical Ultrasound Spring Meeting (Oral), Delft, Netherlands	2017	1.15
Dutch Society for Medical Ultrasound Autumn Meeting, Enschede, Netherlands	2017	0.15
Dutch Society for Medical Ultrasound Spring Meeting, Eindhoven, Netherlands	2017	0.15
2nd Cardiovascular Translational Research Meeting (Poster), Utrecht	2018	1.1
Supervision		
Timothy Hope, May - Sep	2016	0.57
Feriel Khellaf, Mar - Aug	2017	0.86
Onno Gieling, Feb - May	2019	0.57
Total		**30.4**